RATIONAL DESIGN OF METAL-ORGANIC ELECTRONIC DEVICES: A COMPUTATIONAL PERSPECTIVE

Bhaskar Chilukuri, B.Pharm.

Dissertation Prepared for the Degree of

DOCTOR OF PHILOSOPHY

UNIVERSITY OF NORTH TEXAS

December 2012

APPROVED:

Thomas R. Cundari, Major Professor
Mohammad A. Omary, Committee Member
Jincheng Du, Committee Member
W. Justin Youngblood, Committee Member
Bruce E. Gnade, Committee Member
William E. Acree, Jr., Chair of the Department of Chemistry
Mark Wardell, Dean of the Toulouse Graduate School

Chilukuri, Bhaskar. Rational Design of Metal-Organic Electronic Devices: A Computational Perspective. Doctor of Philosophy (Chemistry), December 2012, 151 pp., 15 tables, 61 illustrations, chapter references.

Organic and organometallic electronic materials continue to attract considerable attention among researchers due to their cost effectiveness, high flexibility, low temperature processing conditions and the continuous emergence of new semiconducting materials with tailored electronic properties. In addition, organic semiconductors can be used in a variety of important technological devices such as solar cells, field-effect transistors (FETs), flash memory, radio frequency identification (RFID) tags, light emitting diodes (LEDs), etc. However, organic materials have thus far not achieved the reliability and carrier mobility obtainable with inorganic silicon-based devices. Hence, there is a need for finding alternative electronic materials other than organic semiconductors to overcome the problems of inferior stability and performance.

In this dissertation, I research the development of new transition metal based electronic materials which due to the presence of metal-metal, metal-π, and π-π interactions may give rise to superior electronic and chemical properties versus their organic counterparts. Specifically, I performed computational modeling studies on platinum based charge transfer complexes and d^{10} cyclo-$[M(\mu\text{-}L)]_3$ trimers (M = Ag, Au and L = monoanionic bidentate bridging (C/N~C/N) ligand). The research done is aimed to guide experimental chemists to make rational choices of metals, ligands, substituents in synthesizing novel organometallic electronic materials. Furthermore, the calculations presented here propose novel ways to tune the geometric, electronic, spectroscopic, and conduction properties in semiconducting materials.

In addition to novel material development, electronic device performance can be improved by making a judicious choice of device components. I have studied the interfaces of a

p-type metal-organic semiconductor viz cyclo-$[Au(\mu\text{-}Pz)]_3$ trimer with metal electrodes at atomic and surface levels. This work was aimed to guide the device engineers to choose the appropriate metal electrodes considering the chemical interactions at the interface. Additionally, the calculations performed on the interfaces provided valuable insight into binding energies, charge redistribution, change in the energy levels, dipole formation, etc., which are important parameters to consider while fabricating an electronic device.

The research described in this dissertation highlights the application of unique computational modeling methods at different levels of theory to guide the experimental chemists and device engineers toward a rational design of transition metal based electronic devices with low cost and high performance.

ACKNOWLEDGEMENTS

I would like express my sincere gratitude to several people who played an important role in making my time in the graduate school at the University of North Texas (UNT). First and foremost I thank my adviser Prof. Thomas Cundari who introduced me to the world of computational chemistry. His enthusiasm toward science, ability to explain things clearly and simply, personal encouragement and sound advice were invaluable in not only aiding my doctoral research but also my professional career. He is a good friend, guide and truly means a lot more than just an adviser to me.

I enunciate a special thanks to Prof. Mohammad Omary, my research collaborator at UNT for his mentorship and guidance in multiple research projects. I am grateful to Prof. Jincheng Du at UNT, Prof. Jean-Luc Brédas at the Georgia Institute of Technology, Prof. Mike Whangbo at North Carolina State University and their research groups for training me in multiple codes and numerous fruitful conversations. I am obligated to Dr. Scott Yockel and Dr. Dave Hrovat for all their help in maintaining the computational resources and attending all my research requests at UNT. I would certainly be indebted to all the graduate students and postdocs in $^{\text{Team}}$Cundari for their endless support and friendship.

Last but certainly not least, I express my sincere thanks and love to my parents for their unlimited support in my continued pursuit of education from high school to a doctoral degree. I certainly wouldn't have made this journey toward success without their constant motivation and encouragement. Finally, I would like to thank the rest of my family, friends and relatives for their continuous concern and support.

TABLE OF CONTENTS

LIST OF TABLES

LIST OF ILLUSTRATIONS

CHAPTER 1

INTRODUCTION

1.1 Organic Electronic Devices: Applications, Advantages and Disadvantages

Development of electronic and optoelectronic devices based on organic semiconductors have become important research targets for the past two decades[1]. This increased attention is mainly due their technological applications such as organic light emitting diodes (OLEDs)[2], organic field effect transistors (OFETs)[3] or organic thin film transistors (OTFTs), radio frequency identification (RFID) tags[4], conductive polymer printed electronics[5] and organic photovoltaics (OPVs)[6] or organic solar cells. In addition to the previously mentioned applications, the greatest advantage of using organic semiconductors in electronic devices is that they are extremely cost effective, easy to make, low temperature processed materials, increased device functionality, low energy consumption and capability to make lighter flexible devices than the traditional inorganic or silicon based semiconductors[1-6].

More and more organic electronic devices are making their way into the consumer market every year. Figure 1.1 shows some organic semiconductor based consumer electronics that are currently available or proposed to be released in the near future by major electronics companies. A great deal of progress has been achieved only with some devices such as RFIDs for product tracking and OLEDs leading to portable display screens in cell phones, digital photo frames, laptops and even televisions recently. However, other organic electronic devices such as OFETs and OPVs have not achieved the type of performance and stability similar to those with inorganic electronic devices, which is mainly due to the low electron and hole mobilities (μ) in organic semiconductors[7].

Figure 1.1. Commercial organic electronic devices that are currently in the market or proposed to be released in the future. *Top row (left to right)*: Sony XEL-1 OLED TV, building integrated solar cells by Konarka Technologies, Samsung mobile phones with active matrix OLED display screen. *Bottom row (left to right)*: Flexible OLED-OTFT display by Sony, Nokia flexible ("bendy") concept phone, RFID-tags made with organic materials.

It is important to note that organic semiconducting materials have certain limitations with respect to the charge carrier mobility because of their intrinsic properties such as the bonding nature and crystal packing as a solid. The bonding in organic molecular crystals is mainly due to a variety of intra- and intermolecular interactions, such as van der Waals interactions, weak hydrogen bonds and π-π stacking. However, the degree of overlap of molecular orbitals in organic materials that give rise to a band structure of valence and conduction bands is not wide enough as in conventional inorganic semiconductors that are solely covalently bonded solids. This puts a fundamental limit on the mobility of charge carriers in organic semiconductors versus inorganic materials.

1.2 Organic Electronic Device Architecture

Most organic electronic devices are fabricated with similar device components. If we consider well-studied devices such as OFET[3], OLED[2] and OPV[6], the common device components are the organic semiconductor, metal electrodes and substrate materials. In addition to these device components, OFETs have a gate electrode and dielectric materials. OLEDs and OPVs have hole/electron transport layers, emissive layers, hole blocking layers, photoconductive layers, etc.; all of them are shown as conducting materials in Figure 1.2 (a), (b).

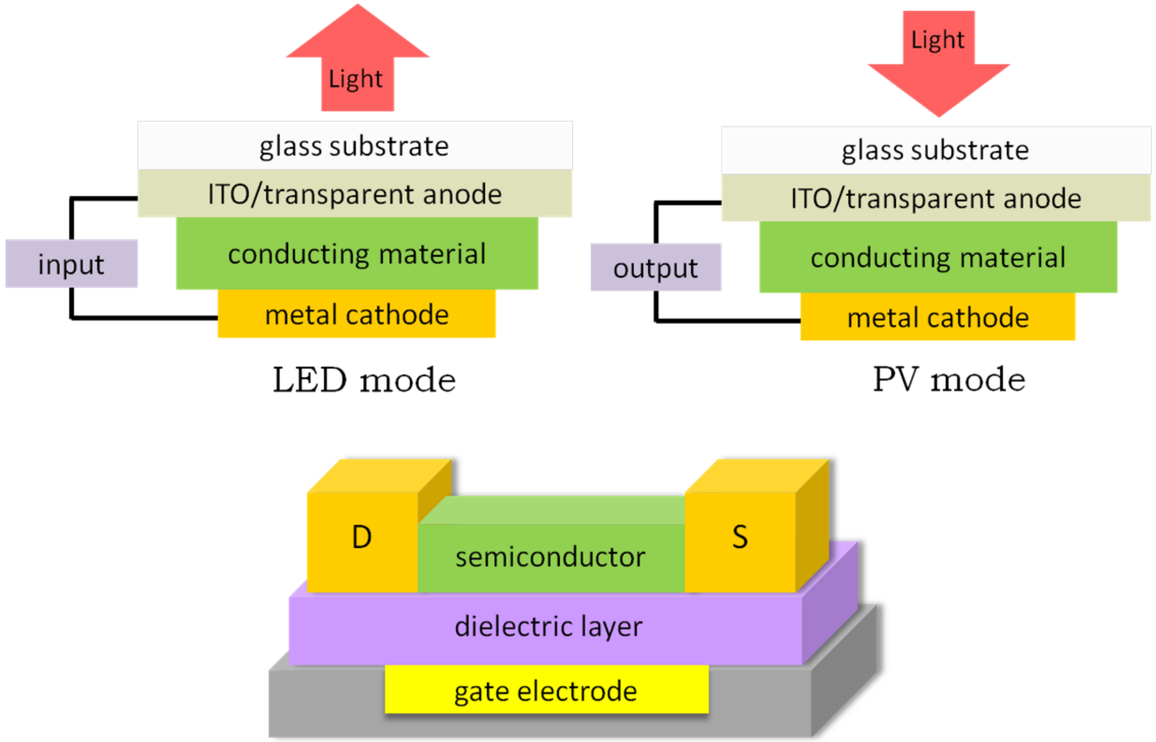

Figure 1.2. Typical layouts of organic electronic devices. OLED (top left), OPV (top right) and OFET (bottom). Note that the OLED and OPV have similar layouts but the difference is with the direction of current and light.

The following subsections very briefly reviews the different types of device components that are conventionally used in organic electronic and optoelectronic devices.

1.2.1 Organic Semiconductors

Organic semiconductors can be broadly classified into two categories based on (a) the type of charge transport such as hole or electron transporting materials, and (b) the nature of molecular architecture like small molecules and macromolecules.

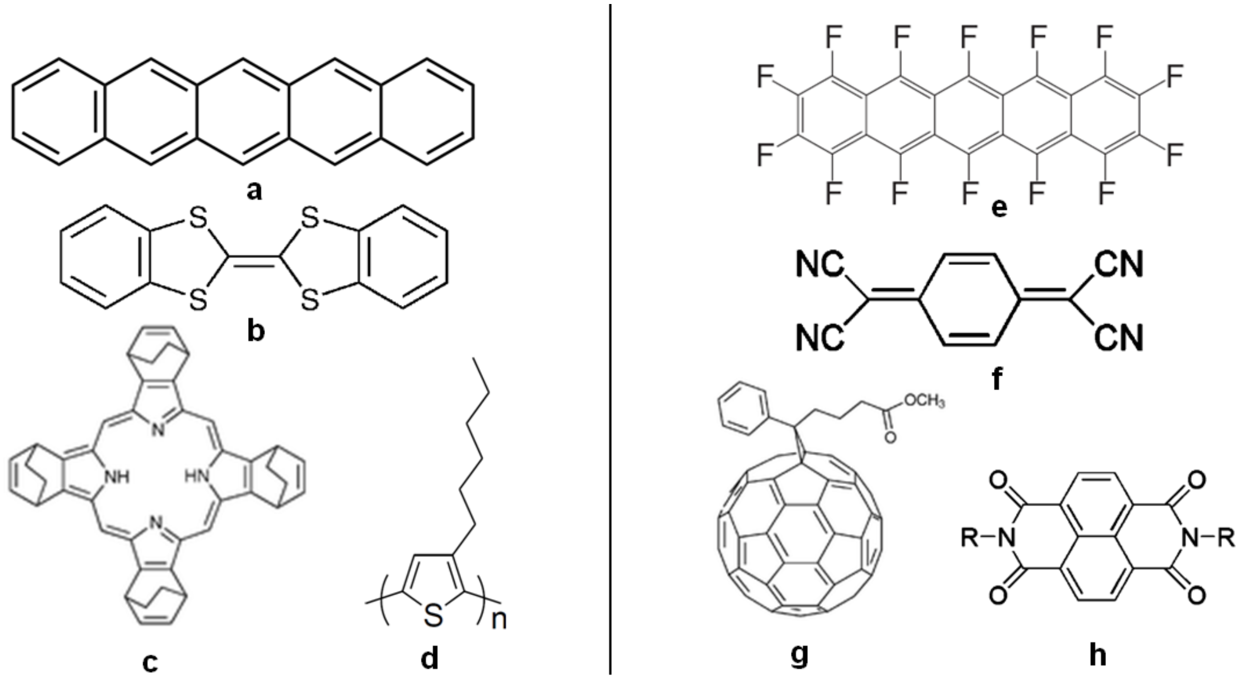

Figure 1.3. Examples of organic semiconductors[8] classified based on charge transport. *p-type materials*: (a) pentacene, (b) dibenzotetrathiafulvalene (DB-TTF), (c) tetrabenzoporphyrin precursor (1,4:8,11:15,18:22,25-tetraethano-29H,31H-tetrabenzo [b,g,l,q] porphine), (d) poly(3-hexylthiophene) (P3HT). *N-type materials*: (e) perfluoro-pentacene, (f) Tetracyanoquinodimethane (TCNQ), (g) [6,6]-phenyl C_{61}-butyric acid methyl ester (PCBM) (h) Naphthalene tetracarboxylic diimide (NDI).

1.2.1.1 Classification of organic semiconductors based on charge transport

Figure 1.3 shows the structures of organic semiconductors which are divided by their type of charge transport. Hole transporting materials donate electrons or accept holes, whereas the electron transporting materials donate holes and accept electrons[8]. Hole transporters conventionally have low ionization potential (IP) and low electron affinity (EA) while electron transporters have high IP and EA values. Determination of the nature of charge transport in a particular material is dependent upon the ease of charge injection from a particular electrode (anode/cathode) in an electronic device. An organic semiconductor is referred to as a hole transporting material if its IP matches closely to the Fermi level of the anode and it is referred to as a an electron transporting materials when its EA matches closely to the Fermi level of the cathode. Hole and electron transporting materials are often called p-type and n-type materials respectively in order to be consistent with the inorganic semiconductor terminology. Also, there are materials that can transport both electrons and holes, which are referred to as ambipolar materials.

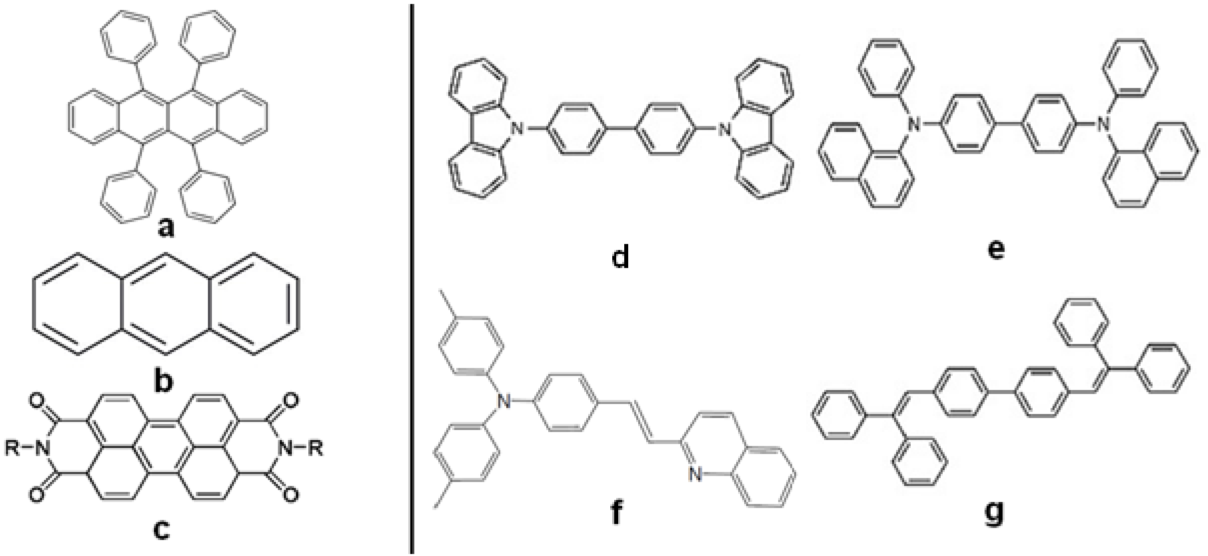

Figure 1.4. Examples of organic semiconductors[8] classified based on their molecular architecture. *Crystalline materials*: (a) rubrene, (b) anthracene, (c) parylene diimide. *Amorphous materials*: (d) CBP (4,4'-*N,N'*-dicarbazole-biphenyl), (e) α-NPB(N, N`-bis(Inaphthyl)-N,N`-diphenyl-1,1`-biphenyl-4,4`-diamine), (f) styryl benzene based semiconductor, (g) DPVBi (4,4'-bis(2,2'-diphenylvinil)-1,1'-biphenyl).

1.2.1.2 Classification of organic semiconductors based on molecular architecture

Classifying organic semiconducting materials based on their molecular architecture basically yields two classes of materials, viz small molecules and macromolecules. Small molecule semiconductors have low molecular weight and include both crystalline and amorphous materials. Crystalline materials are often synthesized with high purity and well defined molecular structure. Organic semiconductors that are crystalline in nature are found to give very high mobilities in contrast to amorphous semiconductors[8]. Figure 1.4 shows the molecular structures of some crystalline and amorphous organic semiconductors. Though crystalline materials have exhibited very high mobilities, growth of crystalline molecules is often difficult on substrate materials due to geometrical mismatch, grain size and boundaries. Amorphous materials on the other hand may easily form thin films on the substrates due to their homogeneous properties, giving them have an advantage over crystalline materials. Though small molecule amorphous semiconductors form uniform thin films on substrates like polymeric semiconductors, it is important to note that the former have well defined molecular weight and structure in contrast to the later.

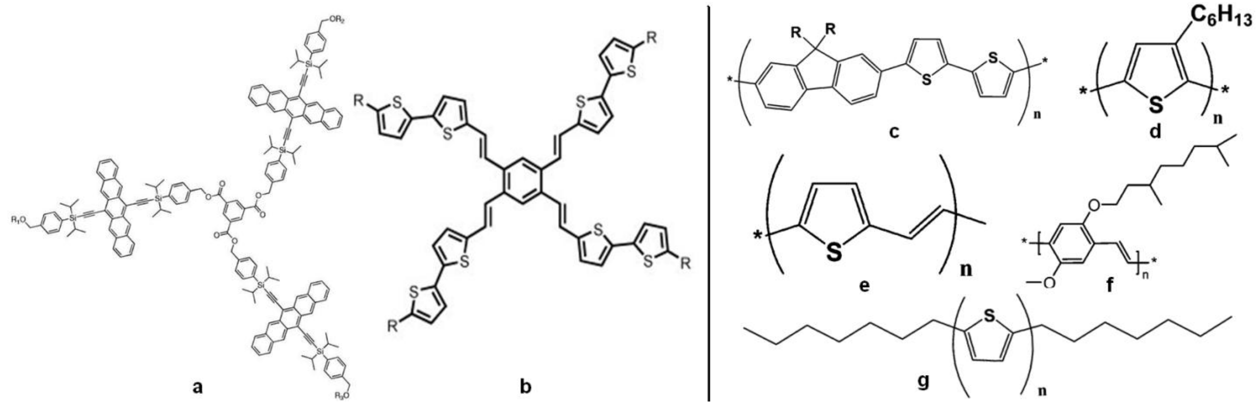

Figure 1.5. Examples of macromolecular organic semiconductors[8-9]. *Dendrimeric materials*: (a) Pentacene based dendrimers, (b) HPBT or DPBT dendrimers (where R= hexyl or dodecyl respectively). *Polymeric materials*: (c) dioctylfluorene-bithiophene (F8T2), (d) poly(3-hexylthiophene) (P3HT), (e) polyvinylthiophene (PVT), (f) Poly(2-methoxy-5-(3'-7'-dimethyloctyloxy)-1,4-phenylene vinylene) (MDMO-PPV), (g) poly-Dihexylthiophene derivatives (n=5: DH-5T, n=6: DH-6T respectively).

Macromolecular organic semiconductors are classified further into dendrimers and polymers[8-9]. A major difference between these two macromolecules is precision in terms of their molecular weights. Dendrimers have precise molecular weight and are synthesized in a controlled fashion with defined structure, points of branching, size and functionalities. This synthetic process can be reproduced countless times and one can still achieve similar dendrimers. On the other hand polymers differ in their shape, size and molecular weights every time they are synthesized. Being inconsistent from batch to batch makes electronic devices fabricated from the same polymers differ in their performance. Figure 1.5 shows the molecular structures of some dendrimeric and polymeric organic semiconductors.

1.2.2 Metal Electrodes

Metal electrodes play a critical role of charge carrier injection into organic electronic devices. The metals that are used as electrodes are usually high and low work function metals[8c] like Al, Au, Ag, Cu, La, Ni, Pd, Pt, Ru, etc. These electrodes act as anodes or cathodes depending upon the type of injected charge carrier (hole/electron). In an OFET, metal electrodes are referred to as source, drain and gate electrodes. Any barrier between the contacts of metal electrodes and organic semiconducting channel will impede the flow of charge through the device. This requires low energetic barriers at the metal-organic interfaces for both contacts to inject equally high amounts of electrons and holes, which is required for a balanced charge carrier flow. Thus, the interface electronic structure plays a very significant role in overall device performance. Choice of an electrode metal in an electronic device depends upon the type of conducting material, surrounding environment, surface chemistry with interacting materials and most importantly the work function. Comparing the work function of the injecting metal with the HOMO/LUMO (HOMO = Highest occupied molecular orbital, LUMO = Lowest unoccupied molecular orbital) levels of a semiconductor can help to determine whether charge injection is likely and whether high or low contact resistance is to be expected.

1.2.3 Gate Dielectrics

Gate dielectric materials are insulating materials present in the OFETs[10] which separate the active semiconducting material from the gate electrode. Figure 1.2 depicts a dielectric layer in a typical thin-film transistor device is sandwiched between the gate electrode and the organic semiconductor. This typical OFET architecture creates two interfaces of dielectric material (one with the semiconducting material and the other with the gate electrode), which must be considered when selecting a suitable dielectric material. Both these interfaces play a very important role in the overall device performance. For example, when considering the dielectric–gate interface, one must address the issue of preventing charge (static and dynamic) injection into the dielectric and leakage currents through pinhole defects from the dielectric material. Also, when considering the interface with organic semiconductor where the conducting channel is formed, the quality of this channel is determined by interface roughness, surface energy, and charges at this interface[11]. The standard dielectric materials used in OFETs are classified into two major types[12]:

1.2.3.1 Inorganic Dielectrics

The most prevalent inorganic dielectric material in OFET devices is SiO_2 which is typically grown as an amorphous thermal oxide on top of silicon. SiO_2 has been widely used due to its ready and cheap availability, large band gap (8.9 eV) and thermodynamic stability[13]. However, its major disadvantage is that SiO_2 surfaces are likely to contain Si-OH defects and water, depending on its processing history and that alkali ions in the oxide layer influence further the quality of device characteristics, particularly hysteresis and threshold voltages. Numerous alternative dielectrics have been considered due to the materials limitations of SiO_2 [14], such as TiO_2 HfO_2, Al_2O_3, Ta_2O_5 etc[12]. Choice of a dielectric is dependent upon not only its dielectric constant but also its interactions with the semiconducting layer and the electrodes. To improve the dielectric properties of inorganic amorphous oxides, researchers have used multiple strategies like anodization of thin-metal films, or surface treatment of inorganic dielectric materials with self-assembled monolayers/multilayers (SAMs)[12]. There are studies using nitrides like Si_3N_4 as the dielectrics as well[8c].

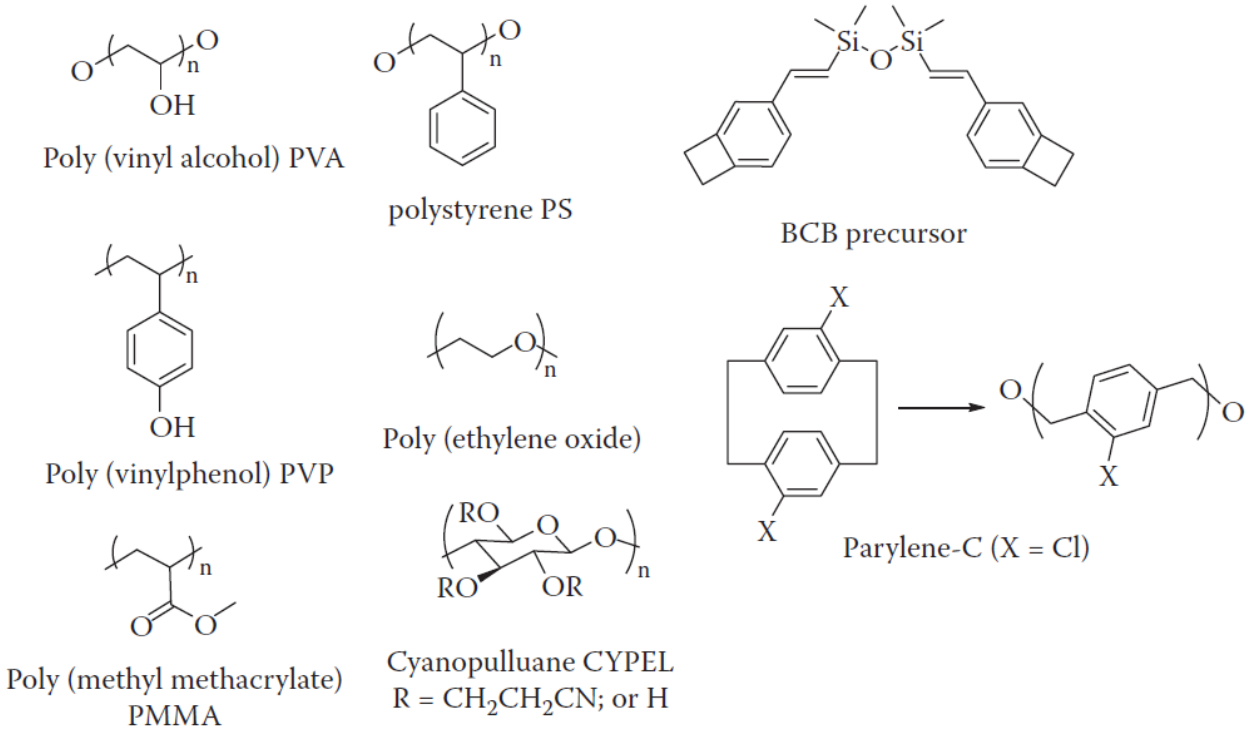

Figure 1.6. Polymeric dielectric materials used in organic field effect transistors[12].

1.2.3.2 Polymer Dielectrics

Polymeric materials are the second major class of dielectric materials used in OFETs, especially in the bottom gate architecture of thin film transistors[12]. Surface treatment of inorganic dielectrics will be practically impossible in bottom gate devices and hence they are replaced with polymeric dielectrics. Also, polymers offer multiple advantages over inorganic dielectrics including solution processability, dip-coating and spin-coating methods. Polymers are flexible and present no special challenge in generating flexible devices. Moreover, polymers form smooth and reproducible films on the semiconducting materials with excellent interfaces. Though polymers have many advantages in terms of flexibility, processability and interaction, they lack the high dielectric constants like inorganic dielectrics that are ultimately necessary to make a device. Examples of polymeric dielectrics include poly vinyl alcohol (PVA), polystyrene (PS), poly vinyl phenol (PVP), Parylene-C, etc. Figure 1.6 shows the structures of some polymeric dielectric materials.

The materials requirements for a suitable gate dielectric for flexible OFETs are challenging and are not easily met by a single material. Thus, there have been recent efforts to explore the use of blended ceramic and polymeric materials on the nanoscale to generate a nanostructured dielectric with an intelligent blending of the desirable properties of its constituents[12]. Some of the composite materials that have been produced on this context are nanoparticle dielectrics such as bismuth titanate-polyacrylate, $BaTiO_3$-PVA, $BaTiO_3$ Luxprint/smoothing layer, TiO_2-PVA, TiO2-PS, etc[12].

1.3 Motivation of Research

Over the last few decades, organic electronics research has led to many successful and ground breaking innovations, especially cheap and flexible devices. However, organic semiconducting materials have certain limitations with respect to the charge carrier mobility because of their intrinsic properties such as the bonding nature and crystal packing in the solid state. Some of the major disadvantages in organic electronic devices made so far are low stability, low carrier mobility (especially in n-type materials), short device life time and inferior performance. So, there is a great scope for finding new organic semiconducting materials to overcome the above mentioned disadvantages. Also, another important aspect in order to improve the electronic device performance is the choice of materials used to build a device. A rational choice of device components (semiconducting materials, electrodes, dielectrics, substrate materials, etc.) considering the material properties and interface interactions will greatly improve device performance.

With this background, I have framed my doctoral research to look into the following two important areas in an effort to guide experimental efforts to design better, cheap and flexible electronic devices. For both of the topics mentioned below, I have used computational modeling tools to guide the experimental synthesis, characterization and device fabrication.

1.3.1 Finding novel organometallic materials

Electronic materials made with transition metals in conjunction with organic ligands can give rise to interesting chemistry due to the presence of a variety of chemical interactions including metal-metal, metal-π, and π-π, ionic, covalent, electrostatic, metallophilic and van der Waals interactions. Thus, organometallic compounds can exhibit useful electronic, geometric, spectroscopic and conduction properties. Figure 1.7 shows some examples of organometallic semiconductors found in the literature[15].

Synthesis of new classes of metal-organic materials by incorporation of transition metals into organic species improves the performance of conventional organic materials in terms of their conductivity, stability, processability, and chromaticity in devices such as OFETs, organic light emitting diodes (OLEDs), and superconductors. Several research groups have produced many novel organometallic electronic materials with interesting properties for applications such as phosphorescent and magnetic devices[16]. Previous research from the Omary and Cundari groups[17] has shown that organometallic materials based on coinage metals produce interesting photophysical properties and that their properties can be tuned by rational manipulation of metal, ligand and ligand substituents. Primary research indicated that these coinage metal trimers have excellent π-acidic and π-basic properties that can surpass the organic p- and n-type materials[16d]. This initial work invoked a strong motivation to develop and tune novel organometallic materials for microelectronics applications like metal-organic light emitting diodes (MOLED) and metal-organic field effect transistors (MOFET).

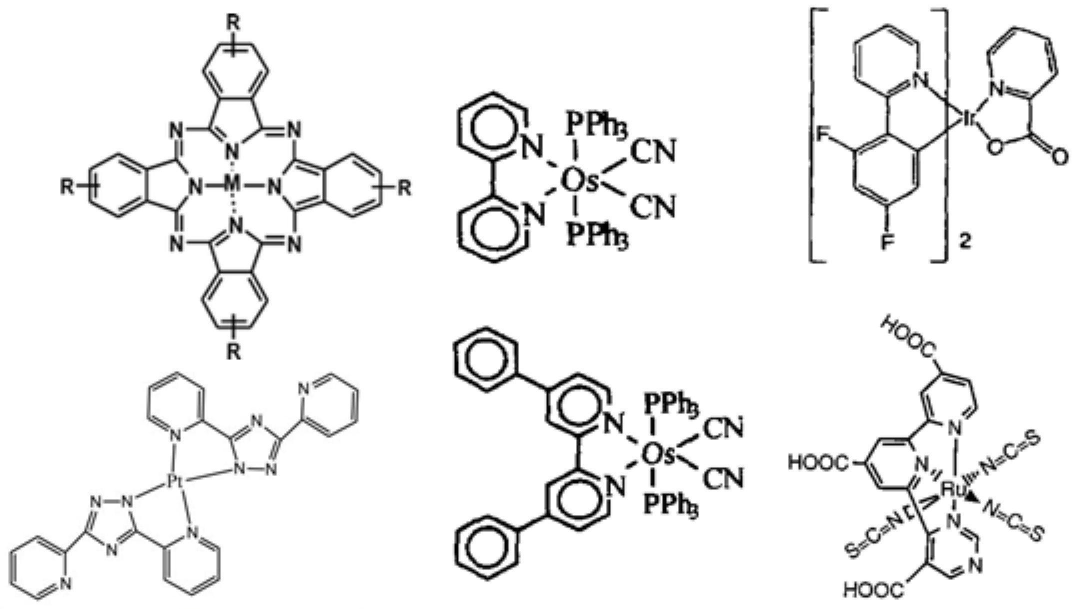

Figure 1.7. Examples of some organometallic electronic materials found in the literature[15].

1.3.2 Understanding interface chemistry in electronic devices

As mentioned earlier, the performance of an electronic device not only depends on the characteristic properties of the semiconducting material but also on the other materials used in the device and their respective interfaces. Although, numerous devices have been made experimentally with organic semiconductors, relatively few have been made with organometallic semiconductors. So, it is important to understand the interface chemistry of organometallic semiconductors with metal electrodes and dielectrics.

Computational modeling of the interface chemistry can be a valuable tool in aiding device fabrication engineers to pick a right choice of device materials (e.g., choice of electrodes, hole and electron transport materials in MOLEDs and choice of dielectrics in MOFETs) in conjunction with the respective semiconductor. I was interested to looking at the interface chemistry between the metal electrodes and the novel organometallic semiconductors developed by our research team in order to suggest rational device combinations for device construction.

1.4 Outline of Thesis

As mentioned in section 1.3, the current research deals with computational modeling of novel organometallic electronic materials and device interfaces for better metal-organic electronic devices. Hence, this thesis is organized in accordance with the aforementioned themes. In Chapter 2, a brief overview of the computational methodology used in the present research is described. Chapters 3 to 5 include the modeling of organometallic materials for electronics applications and Chapters 6 and 7 deal with modeling device interfaces between an organometallic semiconductor and metal electrodes.

In Chapter 3, computational modeling data on the impact of solid state stacking on conduction and charge transfer properties of a platinum donor (D) complex, (dbbpy)Pt(tdt) (dbbpy = 4,4'di-tert-butyl-2,2'-bipyridine; tdt = 3,4-toluenedithiolate) and organic acceptor (A) complex, TENF (TENF = 2,4,5,7-tetranitro-9-flourenone), are presented. The consequences of D/A versus DD/A stacking on electronic material properties of platinum-based charge transfer complexes are elucidated.

In Chapter 4, experimental and computational studies were performed on $[Ag(\mu\text{-}L)]_3 \bullet [Au(\mu\text{-}L)]_3$ cyclo-trimer charge transfer complexes (where L= Triazolate(Tz)/Pyrazolate(Pz) ligand). Electronic spectroscopy and x-ray crystal structure determination of novel Ag•Au charge transfer complexes are presented. The nature and degree of charge transfer (CT) interactions, their chemical origin, change in the interaction by changing the chemical components (ligands, substituents) of the trimers, effect of metallophilic bonds on CT, etc., were studied with combined periodic and molecular modeling methodology.

In Chapter 5, a combined experimental and computational study of how polymorphic forms of gold (I) carbeniate, $[Au_3(RN{=}COR')_3]$ complexes effect their structural, photophysical and conduction properties is reported. Experimental studies on four novel gold (I) carbeniate complexes along with computational modeling data on all solid state stacking possibilities of gold (I) carbeniate complexes available in the literature are presented.

Chapter 6 reports the interactions of different electrode metal atoms (M') with a p-type organometallic semiconductor; a gold (I) pyrazolate (Pz) trimer, cyclo-$[Au(\mu\text{-}Pz)]_3$ is modeled. Electrode metals chosen to assess metal-trimer interactions are M'= Al, Au, Cu, La, Ni, Pd, Pt, Ru and Ni. Modeling the interactions of metal atoms with semiconductors is an important first step in modeling full electrode metal surfaces because in a device there is the possibility of diffusion of metal atoms from the slab into the semiconductor layer causing instability and inferior device performance.

In Chapter 7, a periodic modeling study of interface interactions and electronic properties of cyclo-$[Au(\mu\text{-}Pz)]_3$ trimer (T) with Au(111) and Al(111) metal surfaces is demonstrated. A comparison of the interfacial interactions of the trimer molecule with high work function Au(111) and low work function Al(111) metals is presented. Changes in trimer (T) reorganization both in terms of the energies and geometries, binding energies, orbital hybridization and Fermi levels in different metal surfaces are discussed. This work is an extension of research described in Chapter 6, as the modeling scale moves from molecular to periodic in metal atoms to surfaces respectively.

Finally in Chapter 8, the overall research is summarized and possible future directions are presented.

1.5 Chapter References

(1) (a) Roncali, J. *Chem Rev.* **1992**, *92 (4)*, 711-738. (b) Bryce, M. R. *Chem. Soc. Rev.* **1991**, *20*, 355-390. (c) Dulov, A. A. *Russ. Chem. Rev.* **1966**, *35*, 773. (d) Menard, E.; Meitl, M. A.; Sun, Y. G.; Park, J.-U.; Shir, D. J.-L.; Nam, Y.-S.; Jeon, S.; Rogers, J. A. *Chem. Rev.* 2007, *107*, 1117– 1160. (d) Samuel, I. D. W.; Turnbull, G. A. *Chem. Rev.* **2007,** *107*, 1272-1295. (e) Coropceanu, V.; Cornil, J.; da Silva Filho, D. A.; Olivier, Y.; Silbey, R.; Bredas, J .L. *Chem. Rev.* 2007, *107*, 926– 952

(2) (a) Akhtaruzzaman, M.; Kamata, N.; Nishida, J.; Ando, S.; Tada, H.; Tomura, M.; Yamashita, Y. *Chem. Commun.* **2005**, *41*, 3183-3185. (b) Anthony, J. E. *Chem.Rev.* **2006**, *106*, 5028-5048. (c) Babel, A.; Jenekhe, S. A. *J. Am. Chem. Soc.* **2003**, *125*, 13656-13657.

(3) (a) Barron, J. A.; Bernhard, S.; Houston, P. L.; Abruna, H. D.; Ruglovsky, J. L.; Malliaras, G. G. *J. Phys. Chem. A* **2003**, *107*, 8130-8133. (b) Kido, J.; Okamoto, Y. *Chem. Rev.*, **2002**, *102*, 2357–2368. (c) Kulkarni, A. P.; Tonzola, C. J.; Babel, A.; Jenekhe, S. A. *Chem. Mater.* 2004, *16*, 4556. (d) Li, F.; Tang, H.; Anderegg, J.; Shinar, J. *Appl. Phys. Lett.* **1997**, *70*, 1233.

(4) (a) Potyrailo, R. A.; Surman, C.; Morris, W. G. *J. Comb. Chem.* **2009**, *11*, 598– 603. (b) Dodabalapur, A. *Materials Today* **2006**, *9*, 24–30.

(5) (a) Clemens, W.; Fix, W.; Ficker, J.; Knobloch, A.; Ullmann, A. *J. Mater. Res.* **2004**, *19*, 1963-1973. (b) Berggren, M.; Nilsson, D.; Robinson, N. D. *Nat. Mater.* **2007**, *6*, 3-5. (c) Yan, H.; Chen, Z.; Zheng, Y.; Newman, C.; Quinn, J. R.; Dötz, F.; Kastler, M.; Facchetti, A. *Nature* **2009**, *457*, 679-686.

(6) (a) Bach, U.; Lupo, D.; Comte, P.; Moser, J. E.; Weissortel, F.; Salbeck, J.; Spreitzer, H.; Gratzel, M. *Nature* **1998**, *395*, 583-585. (b) Brabec, C. J. *Sol. Energy Mater. Sol. Cells* **2004**, *83*, 273-292. (c) Brabec, C. J.; Sariciftci, N. S. *Adv. Funct. Mater.* **2001**, *11*, 15-26. (d) Gunes, S.; Neugebauer, H.; Sariciftci, N. S. *Chem. Rev.* **2007**, *107*, 1324.

(7) (a) Sirringhaus, H.; Brown, P. J.; Friend, R. H.; Nielsen, M. M.; Bechgaard, K.; Langeveol-Voss, B. M. W.; Spiering, A. J. H.; Janssen, R. A. J.; Meijer, E. W.; Herwig, P.; Leeuw, D. M. *Nature* **1999**, *401*, 685. (b) Gundlach, D. J.; Lin, Y. –Y.; Jackson, T. N.; Nelson, S. F.; Schlom, D. G. *IEEE Electr. Device L.*, **1997**, *18*, 87. (c) Cho, S.; Lee, K.; Yuen, J.; Wang, G.; Moses, D.; Heeger, A. J.; Surin, M.; Lazzaroni, R. *J. Appl. Phys.*, **2006**, *100*, 114503.

(8) (a) Mas-Torrent, M.; Rovira, C. *Chem. Soc. Rev.* **2008**, *37*, 827–838. (b) Di, C.; Yu, G.; Liu, Y.; Zhu, D. *J. Phys. Chem. B* **2007,** *111,* 14083-14096. (c) Zaumseil, J.; Sirringhaus, H. *Chem. Rev.* **2007,** *107*, 1296-1323.

(9) (a) Li, J.; Liu, D. *J. Mater. Chem.* **2009**, *19*, 7584-7591. (b) Kim, K. H.; Chi, Z.; Cho, M. J.; Choi, D. H.; Kang, H. S.; Cho, M. Y.; Joo, J. *Appl. Phys. Lett.* **2006**, *89*, 202109. (c) Kawasaki, N.; Nagano, T.; Kubozono, Y.; Sako, Y.; Morimoto, Y.; Takaguchi, Y.; Fujiwara, A.; Chu, C.; Imae, T. *Appl. Phys. Lett.* **2007**, *91*, 243515. (d) Lo, S.; Burn, P. L. *Chem. Rev.* **2007**, *107*, 1097-1116.

(10) (a) Facchetti, A.; Yoon, M. H.; and Marks, T. J. *Adv. Mater.* **2005**, *17*, 1705–1725. (b) Dimitrakopoulos, C.; Malenfant, P. *Adv. Mater.* **2002**, *14*, 99–117. (c) Sirringhaus, H. *Adv. Mater.* **2005**, *17*, 2411–2425.

(11) (a) Veres, J.; Ogier, S.; Lloyd, G.; de Leeuw, D. *Chem. Mater.* **2004**, *16*, 4543–4555. (b) Ruiz, R.; Papadimitratos, A.; Mayer, A. C.; Malliaras, G. G. *Adv. Mater.* **2005**, *17*, 1795–1798.

(12) Bao, Z.; Locklin, J. *Organic Field Effect Transistors* pp. 229-251; CRC Press, Taylor & Francis Group: Boca Raton, FL, **2007**.

(13) (a) Wilk, G.; Wallace, R.; Anthony, J. *J. Appl. Phys.* **2001**, *89*, 5243–5275. (b) Wallace, R.; Wilk, G. *MRS Bull.* March **2002**, 192–197. (c) Kingon, A.; Maria, J.; Streiffer, S. *Nature* **2000**, *406*, 1032–1038. (d) Plummer, J.; Griffin, P. *Proc. IEEE* **2001**, *89*, 240–258.

(14) Robertson, J. *Eur. Phys. J. Appl. Phys.* **2004**, *28*, 265–291.

(15) (a) Smucker, B. W.; Hudson, J. M.; Omary, M. A.; Dunbar, K. R. *Inorg. Chem.* **2003**, *42*, 4714. b) Hudson, J. M. *Ph.D. Dissertation*, UNT, Denton, **2007**. c) Olmstead, M. M.; Jiang, F.; Attar, S.; Balch, A. L. *J. Am. Chem. Soc.* **2001**, *123*, 3260. d) Ishibashi, S.; Hasimoto, T.; Kohyama, T.; Terakura, K. *Phys. Rev. B* **2004**, *69*, 155111. (e) Ma, Y.; Zhang, H.; Shen, J.; Che, C. *Syn. Metals* **1998**, *94*, 245-248. (f) Kalyanasundaram, K.; Grätzel, M. *Coord. Chem. Rev.* **1998**, *77*, 347–414. (g) Ye, R.; Baba, M.; Mori, K. *Jap. J. of App. Phys.* **2005**, *44*, L581-L583.

(16) (a) Caseri, W. R.; Chanzy, H. D.; Feldman, K.; Fontana, M.; Smith, P.; Tervoort, T. A.; Goossens, J. G. P.;Meijer, E. W.; Schenning, A. P. H. J.; Dolbnya, I. P.; Debije, M. G.; de Haas, M. P.; Warman, J. M.; van de Craats,M.; Friend, R. H.; Sirringhaus, H.; Stutzmann, N. *Adv. Mater.* **2003**, *15*, 125. (b) Faulmann, C.; Cassoux, P. *Progr. Inorg. Chem.* **2004**, *52*, 399. (c) D'Andrade, B. W.; Forrest, S. R. *Adv. Mater.* **2004**, *16*, 1585.

(17) (a) Omary, M. A.; Rawashdeh-Omary, M.; Gonser, M. W. A.; Elbjeirami, O.; Grimes, T.; Cundari, T. R.; Diyabalanage, H. V. K.; Gamage, C. S. P.; Dias, H. V. R. *Inorg. Chem.* **2005***,* *44*, 8200-8210. (b) Dias, H. V. R.; Diyabalanage, H. V. K.; Rawashdeh-Omary, M.; Franzman, M. A.; Omary, M. A. *J. Am. Chem. Soc.* **2003***,* *125*, 12072-12073. (c) Dias, H. V. R.; Diyabalanage, H. V. K.; Eldabaja, M. G.; Elbjeirami, O.; Rawashdeh-Omary, M.;

Omary, M. A. *J. Am. Chem. Soc.* **2005***, 127*, 7489-7501. (d) Tekarli, S. M.; Cundari, T. R.; Omary, M. A. *J. Am. Chem. Soc.* **2008***, 130*, 1669-1675. (e) Grimes, T.; Omary, M. A.; Dias, H. V. R.; Cundari, T. R. *The J. Phys. Chem. A* **2006***, 110*, 5823-5830.

CHAPTER 2

COMPUTATIONAL METHODOLOGY

The process of solving chemically relevant problems using computational modeling methods, which are developed from mathematical equations based on fundamental laws of physics and chemistry, has achieved great progress, especially over the last three decades[1-2]. Theoretical chemistry can be broadly divided into two basic branches based on the methodology used to describe or solve a chemical phenomenon. These two branches are classical mechanics and quantum mechanics. A detailed explanation of classical and quantum mechanics is out of the scope of this thesis. Instead, I will try to narrow the description of computational methodology relevant to the research described in the thesis with reduced mathematical emphasis.

2.1 Schrödinger Equation

In this work, the computational methodology used for all calculations is quantum mechanics. The goal here is to model chemical systems by computing their electronic properties using the non-relativistic, time-independent Schrödinger equation[1-2].

$$H\Psi = E\Psi \tag{2.1}$$

H is the Hamiltonian operator, Ψ is the wavefunction and E is the energy eigenvalue. The non-relativistic Hamiltonian operator H can be written as a combination of kinetic and potential energy terms of the nuclei and electrons,

$$H = T_n + T_e + V_{ne} + V_{ee} + V_{nn} \tag{2.2}$$

where T_n, and T_e represent the kinetic energy operators of each nucleus and electron in the system, respectively. V_{ne}, V_{ee}, and V_{nn} represent the potential energy operators for Coulombic interactions between nucleus-electron, electron-electron and nucleus-nucleus in the system. Exactly solving the Schrödinger equation is generally infeasible for a number of reasons. Thus, an approximation based on mass of the electron and nuclei in a system was introduced to solve the Schrödinger equation, which is called the Born-Oppenheimer approximation[3]. This approximation assumes that the coupling between the nuclei and electronic motion is zero because of the negligible mass of an electron versus the mass of nuclei. This approximation allows the electronic wavefunction to be solved depending on the nuclear positions but not upon their velocities, i.e., nuclear motion is assumed to be much slower than electron motion so that the former can be considered to be fixed. Even with a variety of approximations, the quantum mechanical equations have never been solved exactly for any chemical system with more than a single electron[1].

2.2 Quantum Chemistry Methodology

Computational methodologies based on quantum mechanics can be broadly divided into ab initio and semi-empirical methods[1b]. The basic difference between ab initio and semi-empirical methods is the use of empirical parameters in the latter to model a chemical system. In this research, I used two theoretical methods for modeling metal-organic electronic materials and their interfaces in electronic devices. They are density functional theory and extended Hückel tight binding theory. These two methods are described briefly focusing on the relevant theory in the following sections.

2.2.1 Density Functional Theory

Density Functional Theory (DFT) is a quantum mechanical electronic structure method in which the Schrödinger equation is approximately solved as a function of electron density[2] of a system under investigation. Unlike popular ab initio methods such as Hartree-Fock (HF)[4], Møller–Plesset perturbation (MPn)[5], configuration interaction (CI)[6], coupled cluster (CC)[7], etc., which are based on the wavefunction, DFT methodology is computationally efficient in terms of the cost and result it produces. The DFT formalism is based on first principle calculations of electron density and hence it is classified by most chemists as an ab initio method. However, certain functionals do use some empirical data to describe the electronic exchange-correlation energy (see below). The theoretical framework for utilizing the electron density as the primary variable to determine the properties of a molecular system is based on three concepts: Thomas-Fermi model[8], Hohenberg-Kohn theorem[9] and Kohn-Sham equations[10].

Thomas-Fermi (TF) Model[8]: Based on the uniform electron gas concept, the Thomas-Fermi model postulates that the electrons are distributed uniformly in phase space and the energy of the atom can be calculated using the kinetic energy functional of electron density combined with a classical expression for the nuclear-nuclear and electron-electron potentials. Thus, the energy is given completely in terms of the electron density and the correct density is determined using the variational principle.

Hohenberg-Kohn (HK) Theorems[9]: Two theorems are proposed by Hohenberg and Kohn. The first theorem states that there is a one-to-one mapping between the electron density and the exact ground state wavefunction. The second theorem states that the functional that delivers the ground state energy of the system, delivers the lowest energy if and only if the input density is the true ground state density. The second theorem is otherwise noted as the variational principle and hence limited only to the ground state and cannot be applied to the excited states.

Kohn-Sham density functional theory (KS-DFT)[10]: DFT theory developed on the above two concepts is based on a pure, or orbital-free, approach. In other words, the energy of interacting electrons in a system is computed as a functional of the density. Though this approach is principally correct, it is not very accurate in practice due to the lack of accurate approximations for the kinetic energy functionals. To overcome these shortcomings, Kohn and

Sham developed modern day DFT, which is also called Kohn-Sham DFT. The basic idea behind KS-DFT is the construction of a fictitious non-interacting system in such a way, that its density is the same as that of the interacting electrons. In other words, the many-body interactions in a static external potential present in any model system is now replaced by non-interacting electrons in an effective potential also called the Kohn-Sham potential.

From the Schrödinger equation and DFT theory based on the TF model and HK theorems, the total energy of a system expressed as a functional ($E[\rho]$) of the charge density (ρ) contains three terms – the kinetic energy, the interaction with the external potential ($V_{ext}[\rho]$) and the electron-electron interaction ($V_{ee}[\rho]$) and so one may write the total energy functional ($E[\rho]$) as

$$\boldsymbol{E[\rho] = T[\rho] + V_{ext}[\rho] + V_{ee}[\rho]} \tag{2.3}$$

The interaction with the external potential, ($V_{ext}[\rho]$) for an N particle system can be expressed in spherical coordinates (r) as

$$V_{ext}[\rho] = \int \hat{V}_{ext}\,\rho(\mathbf{r})d\mathbf{r} \tag{2.4}$$

From the KS-DFT approach, the kinetic and electron-electron functionals can be approximated by a fictitious system of N non-interacting electrons described by a single determinant wavefunction in N "orbitals" ϕ_i, also known as the Kohn-Sham orbitals[10].

$$T_s[\rho] = -\frac{1}{2}\sum_i^N \left\langle \phi_i \middle| \nabla^2 \middle| \phi_i \right\rangle \tag{2.5}$$

$$\rho(\mathbf{r}) = \sum_i^N \left|\phi_i\right|^2 \tag{2.6}$$

Since the significant component of the electron-electron interaction ($V_{ee}[\rho]$) will be the classical Coulomb interaction, the $V_{ee}[\rho]$ term can be replaced by the Hartree energy (V_H) given in terms of charge density (ρ). The total DFT energy functional can now be written as

$$\boldsymbol{E[\rho] = T_s[\rho] + V_{ext}[\rho] + V_H[\rho] + E_{xc}[\rho]} \qquad \textbf{(2.7)}$$

where $E_{\mathrm{xc}}[\rho]$ is the exchange-correlation functional. $E_{\mathrm{xc}}[\rho]$ is defined as the sum of the error made in using a non-interacting kinetic energy and the error made in treating the electron-electron interaction classically. This can be represented as

$$\boldsymbol{E_{xc}[\rho] = (T[\rho] - T_s[\rho]) + (V_{ee}[\rho] - V_H[\rho])} \qquad \textbf{(2.7)}$$

Deriving a suitable formalism for the exchange-correlation functional ($E_{\mathrm{xc}}[\rho]$) is a major problem with DFT. If we write the total energy functional ($E[\rho]$ in equation 2.7) explicitly in terms of the density (ρ) built from non-interacting orbitals (ϕ_i, equation 2.6) and apply the variational principle, we find that the orbitals, which minimize the energy, satisfy the following set of equations, the Kohn-Sham equations[2,10].

$$\left[-\frac{1}{2}\nabla^2 + v_{ext}(\mathbf{r}) + \int \frac{\rho(\mathbf{r}')}{|\mathbf{r}-\mathbf{r}'|} d\mathbf{r}' + v_{xc}(\mathbf{r})\right]\phi_i(\mathbf{r}) = \varepsilon_i \phi_i(\mathbf{r}) \qquad \textbf{(2.8)}$$

$$v_{xc}(\mathbf{r}) = \frac{\delta E_{xc}[\rho]}{\delta \rho} \qquad \textbf{(2.9)}$$

The Kohn-Sham equations have the same structure as the Hartree-Fock equations, with the non-local exchange potential replaced by the local exchange-correlation potential ($\boldsymbol{v_{xc}}$).

A variety of density functionals have appeared over the last few decades[11-12] based on KS-DFT. These density functionals primarily differ in their approximations to account for the exact exchange and correlation energy functional ($E_{\mathrm{xc}}[\rho]$). Some of the initial approximations used to describe the $E_{\mathrm{xc}}[\rho]$ functionals include the local density approximation (LDA), local spin-density approximations (LSDA) and generalized gradient approximations (GGA)[2]. These approximations are further developed by tweaking the formalism using the gradient or Laplacian of electron density to better describe the exchange and correlation functionals. These approximations acted as starting points to develop the modern “hybrid functionals” that better describe the exchange part of the $E_{xc}[\rho]$ functionals by inclusion of a portion of the exact exchange energy from Hartree-Fock theory. In other words, the exact exchange energy in hybrid functionals is expressed in terms of Kohn-Sham orbitals instead of electron density.

KS-DFT can be used for both molecular and periodic calculations. In the present research, hybrid DFT functionals, B3LYP[13] and M06[14] are used for single-point, structure optimization and property descriptions in molecular calculations. For the solid state calculations, plane-wave basis sets[15] are used to describe the delocalized electrons of an infinite crystal for each point in k-space, called the Brillouin zone[16]. Further details of the DFT methodology are described in the respective chapters.

2.2.2 Extended Hückel Tight Binding Method

The extended Hückel method is a semi-empirical quantum chemistry method developed by Roald Hoffmann[17] based on the Hückel method. The basic difference between the original Hückel and extended Hückel theory is the consideration of both σ and π orbitals in the later method while only π orbitals were considered for the Hückel method. Like Hückel theory, the extended Hückel method focuses only on valence electrons and orbitals. Calculations of electronic interactions in Extended Hückel Theory (EHT) avoid the inclusion of the electron-electron repulsion term (V_{ee} in equation 2.2). EHT uses the Koopmans' theorem[18] and assigns the diagonal elements in the Fock matrix to be atomic ionization potentials. The off-diagonal elements are parameterized as averages of the diagonal elements, weighted by an overlap integral according to Wolfsberg-Helmholz approximation[19].

$$H_{ij} = KS_{ij}\,(H_{ii} + H_{jj})/2 \tag{2.7}$$

Here K is the Wolfsberg-Helmholz constant, which is typically 1.75. H_{ij} represents the Hamiltonian matrix and S_{ij} is the simple σ and π diatomic overlaps (a group overlap G(i, j) can be written in terms of S_{ij}). H_{ii} and H_{jj} denote the energy of an electron in the i^th and j^th orbital, respectively, in the field of the nuclear skeleton and the remaining valence electrons.

The extended Hückel method is used in conjugation with the tight binding model developed for periodic systems, using an approximate set of wavefunctions based upon superposition of wavefunctions for isolated atoms located at each atomic site for the calculation of the electronic band structure. The combination of extended Hückel method and the tight binding model is thus named the Extended Hückel Tight Binding (EHTB) method[20]. The extended Hückel method can be used for determining the molecular/crystal orbitals, relative energies of different geometric configurations of molecules and crystals, approximate determination of certain molecular/solid-state properties, structure-property relationships, etc. The major drawbacks of EHT are that it is incapable of performing geometry optimizations and thus determining accurate bond lengths and energies.

2.3 Basis Sets

In simple terms, a basis set[1-2,21] can be defined as a mathematical description of the motion and position of electron is in the molecular orbitals (MO) of a system,. A basis set is built using a combination of basis functions used to describe the size, shape and energy of the orbitals in an atom. In other words, basis functions approximately describe the shape and symmetry of atomic orbitals, while a basis set is a linear combination (equation 2.8) of N such basis functions to describe molecular orbitals in a system.

$$\Psi_i = \sum_{\mu=1}^{N} C_{\mu i}\, \varphi_\mu \qquad \textbf{(2.8)}$$

Here, μ is the size/number of basis functions in the basis set, φ is the basis function and Ψ_i is the basis set. A wide variety of basis sets have been defined to describe different systems depending upon the desired accuracy in calculated properties, molecular composition of the system, computational scaling, etc. The choice of a right combination of basis sets together with ab initio or DFT methodologies is critically important to obtain the desired results from electronic structure calculations. In the following few sections, a brief description of the different types of basis sets used in this research is presented.

2.3.1 Pople Basis Sets

Bonding in molecules occurs mostly due to interaction of valence electrons. Based on this fact Pople[23] and coworkers defined a group of basis sets where valence atomic orbitals are represented by more than one basis function. Multiple basis functions corresponding to each valence atomic orbital are called valence double, triple, quadruple-zeta, and so on, basis sets. Such basis sets are called split-valence basis sets. They are represented typically in the form of $A\text{-}B_1B_2G$, $A\text{-}B_1B_2B_3G$, $A\text{-}B_1B_2B_3B_4G$, *etc.* In $A\text{-}B_1B_2G$, '*A*' represents the number of primitive Gaussian functions (*G*) comprising each core atomic orbital basis function. B_1 and B_2 represent that the valence orbitals are composed of two basis functions each, the first one composed of a linear combination of B_1 primitive Gaussian functions, the other composed of a linear combination of B_2 primitive Gaussian functions. Since there are 2 characters after the hyphen and before '*g*' in $A\text{-}B_1B_2g$ basis set, it is called a double zeta (ζ, historically represented the exponent of a Slater-type orbital basis function) split valence basis set. Similarly, $A\text{-}B_1B_2B_3g$, $A\text{-}B_1B_2B_3B_4g$, …. represent the triple-zeta, quadruple-zeta, …. basis sets. In the present research, most of calculations are performed using the 6-31G and 6-311G basis sets. More details about the use of Pople basis sets and adding the respective polarization and diffuse functions to them are described in the computational methodology section of individual chapters.

2.3.2 ECP Basis Sets

In transition metal containing systems, inclusion of all-electron correlation energy is computationally not feasible, so pseudopotentials have been introduced to account for the cost[24]. Effective core potentials (ECPs) are a useful means of replacing the core electrons in a calculation with an effective potential (also called a pseudopotential)[25], thereby eliminating the need for the core basis functions, which usually require a large set of Gaussians (g) to describe them. Effective core potentials (ECPs) essentially replace the Coulombic potential term (V_{ne} in equation 2.2) of the Schrödinger equation. In addition to replacing the core, they may be used to model relativistic effects, which are largely confined to the core. In this context, both the scalar (spin-free) relativistic effects and spin-orbit (spin-dependent) relativistic effects may be included in effective potentials. In the present research, all calculations on molecules containing transition metal species are performed using CEP-31G(d)[26] or LANL2DZ[27] pseudopotential basis sets. More details are given in the computational methodology section of the respective chapters.

2.3.3 Plane Wave Basis Sets

In solid state or periodic systems, it is impossible to model the near infinite number of interacting electrons in a system[28]. In a perfect periodic crystal, the ions are arranged periodically and hence the external potential felt by the electrons will also be periodic. In crystalline simulations the period is defined by the unit cell. Bloch's theorem[29] uses the periodicity of a crystal to reduce the infinite number of one-electron wavefunctions to be calculated to the number of electrons in the unit cell of the crystal. Using this theorem, basis sets using a pseudopotential plane wave approach have been proposed for calculating ground state properties of extended systems within the framework of DFT methodology[2].

Plane waves are defined as constant frequency waves whose wave fronts are infinite parallel planes of constant peak-to-peak amplitude normal to the phase velocity vector. In a unit cell of a crystal under periodic boundary conditions (PBCs), plane waves are periodic, orthonormal and complete. Within the PBC, the real space is Fast Fourier Transformed (FFT) into reciprocal space and a finite number of plane waves within the cut off energy makes up a finite basis set to calculate the electron density. In practice, plane-wave basis sets are often used in combination with ECPs, so that the plane waves are only used to describe the valence charge density.

2.4 Chapter References

(1) (a) Cramer, C. J. *Essentials of Computational Chemistry*, *2nd* ed.; John Wiley & Sons: Chichester, **2004**. (b) Jensen, F. *Introduction to Computational Chemistry, 2nd* ed; John Wiley & Sons: Chichester, **2007**. (c) Levine, I. N. *Quantum Chemistry, 6th* ed.; Pearson Education, Inc.: Upper Saddle River, NJ, **2009**. (d) Lewars, E. *Computational Chemistry: Introduction to the Theory and Applications of Molecular and Quantum Mechanics*; Kluwer Academic Publishers: Norwell, MA, **2003**.

(2) (a) Koch, W.; Holthausen, M. C. *A Chemist's Guide to Density Functional Theory*, *2nd* ed.; Wiley-VCH: Weinheim, **2001**. (b) Sholl, D. S.; Steckel, J. A. *Density Functional Theory: A Practical Introduction,* John Wiley & Sons, Inc.: Hoboken, NJ, **2009**.

(3) Born, M.; Oppenheimer, J. R. *Ann. Physik.* **1927**, *84*, 457-484.

(4) (a) Hartree, D. R. *Proc. Camb. Phil. Soc.* **1928**, 24, *89*. (b) Fock, V. *Zeits. f. Physik* **1930**, *61*, 126. (c) Slater, J. C. *Phys. Rev.* **1930**, *35*, 210.

(5) Møller, C.; Plesset, M. S. *Phys. Rev.* **1934**, *46*, 618-633.

(6) (a) Cramer, C. J. *Essentials of Computational Chemistry*, *2nd* ed., pp. 205-211; John Wiley & Sons: Chichester, **2004**. (b) Sherrill, D. C.; Schaefer III, H. F. *In Löwdin, Per-Olov. Advances in Quantum Chemistry*. 34, pp. 143–269; Academic Press: San Diego, **1999**.

(7) Cramer, C. J. *Essentials of Computational Chemistry*, *2nd* ed., pp. 224-227; John Wiley & Sons: Chichester, **2004**.

(8) Fermi, E. *Z. Phys.* **1928**, *48*, 73. (b) Thomas, *Proc. Camb. Phil. Soc.* **1927**, *23*, 542.

(9) Hohenberg, P.; Kohn, W. *Phys. Rev.* **1964**, *136*, B864.

(10) Kohn, W.; Sham, L. J. *Phys. Rev.* **1965**, *140*, A1133.

(11) (a) Sousa, S. F.; Fernandes, P. A.; Ramos, M. J. *J. Phys. Chem. A* **2007**, *111*, 10439-10452. (b) Zhao, Y.; Truhlar, D. G. *Acc. Chem. Res.* **2008**, *41*, 157. (c) Quintal, M. M.; Karton, A.; Iron, M. A.; Boese, A. D.; Martin J. M. L. *J. Phys. Chem. A* **2006,** *110,* 709 and references therein.

(12) (a) Buhl, M.; Kabrede, H. *J. Chem. Theory Comput.* **2006**, *2*, 1282–1290. (b) Waller, M. P.; Braun, H.; Hojdis, N.; Buhl, M. *J. Chem. Theory Comput.* **2007***, 3*, 2234-2242. (c) Buhl, M.; Reimann, C.; Pantazis, D. A.; Bredow, T.; Neese, F. *J. Chem. Theory Comput.* **2008***, 4*, 1449-1459.

(13) (a) Stephens, P. J.; Devlin, F. J.; Chabalowski, C. F.; Frisch, M. J. *J. Phys. Chem.* **1994***, 98*, 11623-11627. (b) Becke, A. D. *Phys. Rev. A* **1988***, 38*, 3098. (c) Lee, C.; Yang, W.; Parr, R. G. *Phys. Rev. B* **1988***, 37*, 785.

(14) (a) Lynch, B. J.; Fast, P. L.; Harris, M.; Truhlar, D. G. *J. Phys. Chem. A* **2000**, *104*, 4811. (b) Zhao, Y.; Lynch, B. J.; Truhlar, D. G. *J. Phys. Chem. A* **2004**, *108*, 2715. (c) Zhao, Y.; Truhlar, D. *Theor. Chem. Acc.* **2008***, 120*, 215-241.

(15) (a) Kresse, G.; Joubert, D. *Phys. Rev. B* **1999***,* *59*, 1758. (b) Perdew, J. P.; Burke, K.; Ernzerhof, M. *Phys. Rev. Lett.* **1996***,* *77*, 3865.

(16) Monkhorst, H. J.; Pack, J. D. *Phys. Rev. B* **1976***,* *13*, 5188.

(17) (a) Hoffmann, R.; Lipscomb, W.N. *J. Chem. Phys.* **1962,** *36,* 2179. (b) Hoffmann, R.; Lipscomb, W.N. *J. Chem. Phys.* **1962,** *36*, 3489. (c) Hoffmann, R.; Lipscomb, W.N. *J. Chem. Phys.* **1963,** *37,* 590. (d) Hoffmann, R. *J. Chem. Phys.* **1963**, *39,* 1397. (e) Hoffmann, R. *Solids and Surfaces: A Chemist's View of Bonding in Extended Structures*; Wiley-VCH: New York, **1988**.

(18) Koopmans, T. *Physica* (Elsevier), **1934**, *1 (1–6)*, 104–113.

(19) Wolfsberg, M.; Helmholz, L. J. *J. Chem. Phys.* **1952**, *20 (5)*, 837.

(20) (a) Whangbo, M-H.; Hoffmann, R. *J. Am. Chem. Soc.* **1978**, *100*, 6093. (b) Whangbo, M-H.; Hoffmann, R.; Woodward, B. *Proc. Royal Soc. A* **1979**, *366*, 23.

(21) Davidson, E.; Feller, D. *Chem. Rev.* **1986**, *86 (4)*: 681–696.

(22) Lennard-Jones, J. E. *Trans. Faraday Soc.* **1929**, *25*, 668

(23) (a) Binkley, J. S.; Pople, J. A.; Hehre, W. J. *J. Am. Chem. Soc.* **1980**, *102*, 939-47. (b) Collins, J. B.; Schleyer, P. v. R.; Binkley, J. S.; Pople, J. A. *J. Chem. Phys.* **1976**, *64*, 5142-51. (c) Gordon, M. S.; Binkley, J. S.; Pople, J. A.; Pietro, W. J; Hehre, W. J. *J. Am. Chem. Soc.* **1982** *104 (10)*, 2797-2803. (d) Francl, M. M.; Pietro, W. J; Hehre, W. J; Binkley, J. S.; Gordon, M. S.; DeFrees, D. J.; Pople, J. A. *Chem. Phys.* **1982**, *77*, 3654.

(24) Cundari, T. R.; Benson, M. T.; Lutz, M. L.; Sommerer, S.O. *Rev. Comp. Chem.* **1996**, *8*, 145-202.

(25) (a) Szasz, L. *Pseudopotential Theory of Atoms and Molecules*; John Wiley & Sons: New York, **1985**. (b) Krauss, M.; Stevens, W. J. *Ann. Rev. Phys. Chem.* **1984**, *35*, 357-385.

(26) (a) Stevens, W. J.; Krauss, M.; Basch, H.; Jasien, P. G. *Can. J. Chem.* **1992**, *70*, 612. (b) Stevens, W. J.; Basch, H.; Krauss, M. *J. Chem. Phys.* **1984**, *81*, 6026-6033. (c) Cundari, T. R.; Stevens, W. J. *J. Chem. Phys.* **1993**, *98*, 5555-5565.

(27) Hay, P.; Wadt, W. *J. Chem. Phys.* **1985**, *82*, 270.

(28) Hergert, W.; Ernst, A. *Computational Materials Science: From Basic Principles to Material Properties*; Springer: Verlag Berlin Heidelberg New York, **2004**.

(29) Blochl, P. E. *Phys. Rev. B.,* **1994**, *50*, 17953-17979.

CHAPTER 3

EFFECT OF CRYSTAL STACKING ON DONOR-ACCEPTOR INTERACTIONS IN PLATINUM BASED CHARGE TRANSFER COMPLEXES*

3.1 Introduction

Study of charge transfer complexes has been an active area of research for over three decades. Several pure organic[1-4] and hybrid-inorganic[5-9] complexes showing interesting electronic and charge transfer properties have been studied over the years. Dunbar, Omary and coworkers have studied novel supramolecular stacks containing inorganic donors of the formula (dbbpy)M(dmid) (M = Pt, Pd; dbbpy = 4,4'di-tert-butyl-2,2'-bipyridine; dmid = 2-oxo-1,3-dithiole-4,5-dithiolate) with different nitrile acceptors such as TCNQ (TCNQ = 7,7,8,8-tetracyanoquinodimethane) [10-13]. These materials display interesting optoelectronic properties in solution and in the solid state, e.g., as photosensitizing dyes for solar cells based on wide band gap semiconductors[10-18]. Omary and coworkers[11-12] have synthesized new supramolecular systems containing (dbbpy)Pt(tdt) (dbbpy = 4,4'di-tert-butyl-2,2'-bipyridine; tdt = 3,4-toluenedithiolate) and the organic acceptor TENF (TENF = 2,4,5,7-tetranitro-9-flourenone), Figure 3.1, built from (dbbpy)Pt(tdt) donors (D) with TENF acceptors (A).

The stacking pattern of donors (D) and acceptors (A) as well as their relative orientation in the solid state impact the conductivity of such materials, yielding metallic, insulating, or semiconducting properties[10-23]. Interestingly, by changing the crystal growth conditions, the stacking in the above mentioned materials varies in the ratio of donor to acceptor molecules. For

---

* This entire chapter is reproduced from [Cundari, T. R.; Chilukuri, B.; Hudson, J. M.; Minot, C.; Omary, M. A.; Rabaâ, H. "Periodic and Molecular Modeling Study of Donor−Acceptor Interactions in (dbbpy)Pt(tdt)·TENF and [Pt(dbbpy)(tdt)]$_2$·TENF" *Organometallics* **2010**, vol. *29*, pp 795-800], with permission for electronic and print publication in thesis and dissertation from the American Chemical Society (ACS) to Bhaskar Chilukuri # 3000501953.

(dbbpy)Pt(tdt) and TENF, crystallography reveals both a 1:1 (D/A) stacking pattern (Figure 3.2(a))of the donor and acceptor molecules, as well as a 2:1 (DD/A) pattern[12]. (Figure 3.2 (b)) Both patterns crystallize in the $P2_1/n$ space group. The crystal structure of (dbbpy)Pt(tdt)•(TENF) has a linear chain structure with D/A stacking and close D:A contacts of 3.49 Å. The DD/A material has D:A and D:D distances of 3.34 and 3.45 Å, respectively. In the latter, the TENF molecule is sandwiched between two donor molecules, Figure 3.2(b).

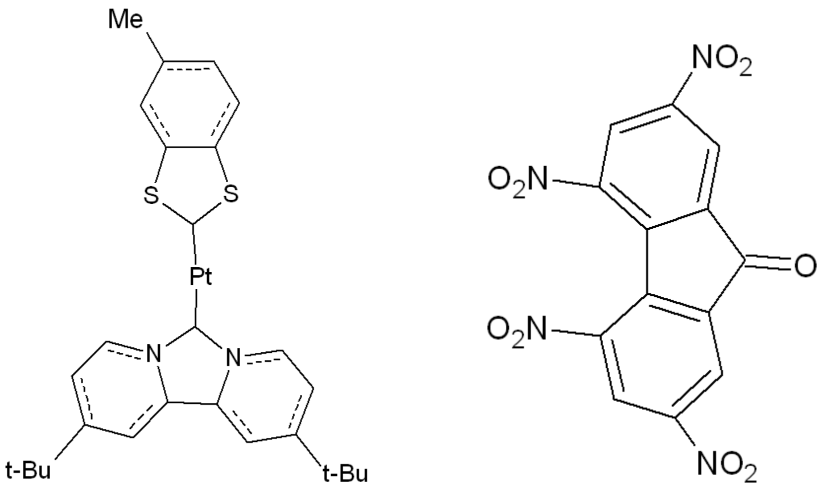

Figure 3.1. Molecular structures of (dbbpy)Pt(tdt) donor (D) (left) and TENF acceptor(A) (right).

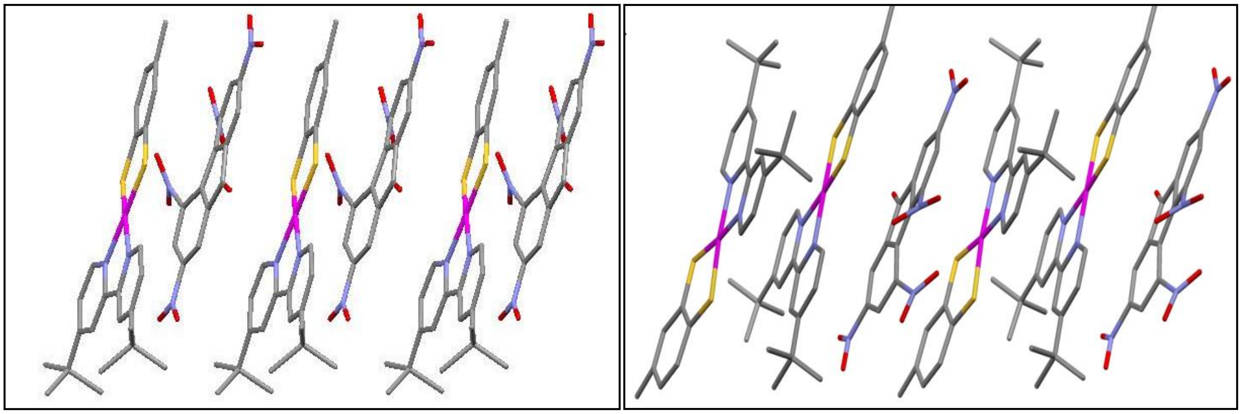

Figure 3.2. Crystallographic structures[11-12] for (a) D/A stacks of (dbbpy)Pt(tdt)•(TENF) (left) and (b) DD/A stacking of $[Pt(dbbpy)(tdt)]_2$•(TENF) (right).

Table 3.1. Experimental[11-12] lattice parameters of $[(dbbpy)Pt(tdt)]_{1,2}$•(TENF) used for periodic DFT simulations.

Parameter	Pt(dbbpy)(tdt)•(TENF)	$[Pt(dbbpy)(tdt)]_2$•(TENF)
a (Å)	23.128(2)	11.257(2)
b (Å)	7.1640(6)	26.004(5)
c (Å)	25.474(2)	24.165(5)
α (°)	90	90
β (°)	109.19(10)	92.19(3)
γ (°)	90	90

In this chapter, DFT based solid state calculations on Pt based donor-acceptor materials are reported. The electronic structure and charge transfer properties of D/A and DD/A stacks are analyzed, viz (dbbpy)Pt(tdt)•(TENF) and $[Pt(dbbpy)(tdt)]_2$•(TENF), respectively. We focused our research on the structural and electronic parameters of these stacks, the fractional charge on TENF, and the implications of these for D to A charge transfer.

3.2 Computational Methods

Solid-state calculations were carried out using the VASP (Vienna Ab initio Simulation Program) code[24]. Density functional theory within the PAW (Projector-Augmented Wave) method[25]; the generalized gradient approximation (GGA) functional of Perdew, Burke and Ernzerhof (PBE)[26] was employed. The electronic wave functions were sampled on a 1×3×1 k-mesh in the irreducible Brillouin zone (BZ) using the Monkhorst and Pack method[27]. The cut-off energy of the wave functions was 400 eV. Convergence of the total energy with the k-mesh in the Brillouin zones and the plane wave cut-off energy was checked.

3.3 Results and Discussion

For plane-wave DFT simulations the ^{t}Bu groups of dbbpy were replaced with hydrogen atoms to save computational effort and the lattice constants kept fixed at experimental values,[11-

[12] Table 3.1. Heavy atoms were fixed at experimentally determined positions while C-H bond lengths were standardized to 1.083 Å. VASP calculations were also carried out on the isolated D and A components using crystallographic coordinates for the D/A stack material. Given the expense of these systems and the large number of atoms (408 in the largest simulations) in the unit cell, neither lattice nor ionic relaxation was investigated.

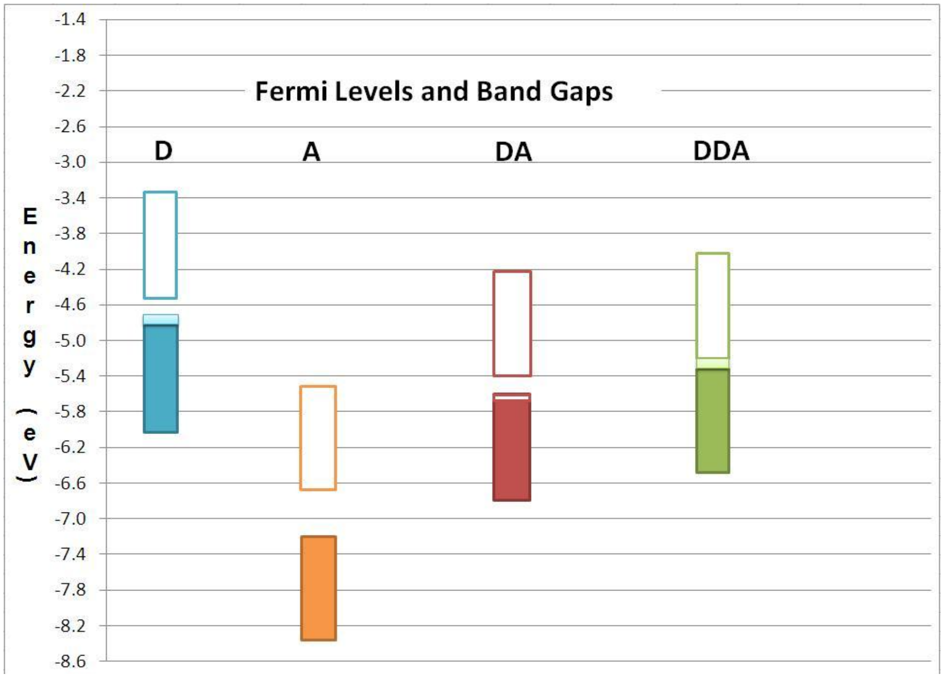

Figure 3.3. Schematic depiction of Fermi levels for D, A, D/A and DD/A materials obtained via periodic plane-wave DFT simulations. The colored filled portions denote the valence band and the empty portions denote the conduction band. Fermi energies for the materials investigated are as follows: D (-4.8 eV), A (-7.2 eV), D/A (-5.6 eV) and DD/A (-5.3 eV).

The results obtained from the plane-wave DFT (PW-DFT) simulations of crystalline D, A, D/A and DD/A are depicted in Figure 3.3. Three points are of interest with respect to the VASP simulations. First, the PW-DFT calculations support the EHTB (Extended Huckel Tight Binding method) supposition[28] as to the increase (shifting) in the Fermi energy upon going from the D/A to the DD/A material. In the case of the PW-DFT calculations the increase is 0.3 eV (-5.6 eV → -5.3 eV) versus 0.4 eV from the EHTB calculations (-9.55 eV → -9.95 eV). Second, note the disposition of the Fermi level (-4.8 eV) for the isolated D molecules while the A molecules show a considerably lower Fermi energy (-7.2 eV). This result is consistent with the flow of electrons from D → A as suggested by the charge transfer model obtained from analysis of the EHTB simulations.[28] One can deduce from Figure 3.3 that A and D present a much different electronic structure in isolation versus the ~ 3.5 Å separation of the stacks. The interaction between D and A is noticeably enhanced in D/A and DD/A stacks, which we propose from the calculations is primarily via charge transfer. Third, the PW-DFT calculations suggest the DD/A material will be a better conductor given that the Fermi level is located in a region of high DOS in terms of the filled bands.

Overall, the PW-DFT and EHTB calculations[28] show qualitatively similar features unless some difference has happened in D/A with some opening of band gap less than 0.1 eV, which is normal when we compare two different levels of theory.

3.4 Summary and Conclusions

Theoretical VASP results give evidence of semi-metallic behavior for the D/A material (gap < 0.1 eV) and metallic behavior for DD/A. We note that dispersion and the conduction band differences are more emphasized in DD/A than in D/A in terms of charge transfer and interaction between metallic and organic fragment, indicating a substantial contribution from TENF and tdt in this transfer (vide supra). In addition the EHTB results[28] agree with the PW-DFT calculations, which suggest the DD/A material will be a better conductor than D/A with filled bands and the Fermi level is located in a region of high DOS.

3.5 Chapter References

(1) Ferraris, J.; Cowan, D. O.; Walatka, V. V., Jr.; Perlstein, J. H. *J.Am. Chem. Soc.* **1973**, *95*, 948.

(2) Coleman, L. B.; Cohen, M. J.;Sandman, D. J.; Yamagashi, F. G.; Garito, A. F.; Heeger, A. J. *J. Solid State Commun.* **1973**, *12*, 1125.

(3) Wudl, F. *Acc. Chem. Res.* **1984**, *17*, 227.

(4) Williams, J. M.; Ferraro, J. R.; Thorn, R. J.; Carlson, K. D.; Geiser, U.; Wang, H. H.; Kini, A. M.; Whangbo, M.-H. *Organic Superconductors (including Fullerenes)*; Prentice Hall: Englewood Cliffs, NJ, **1992**.

(5) Bousseau, M.; Valade, L.; Legros, J.-P.; Cassoux, P.; Garbauskas, M.; Interrante, L. V. *J. Am. Chem. Soc.* **1986**, *108*, 1908.

(6) Brossard, L.; Bousseau, M.; Ribault, M.; Valade, L.; Cassoux, P. *C. R. Acad.Sci.2,* **1986**, *302*, 205.

(7) Brossard, L.; Ribault, M.; Valade, L.; Cassoux, P. *Phys.Re*V. *B* **1990**, *42*, 3935.

(8) Cassoux, P.; Valade, L.; Kobayashi, H.; Kobayashi, A.; Clark, R. A.; Underhill, A. E. *Coord. Chem. Re*V. **1991**, *110*, 115.

(9) Cassoux, P. *Coord. Chem. Re*V. **1999**, *185-186*, 213.

(10) Smucker, B. W.; Hudson, J. M.; Omary, M. A.; Dunbar, K. R. *Inorg. Chem.* **2003**, *42*, 4714.

(11) Hudson, J. M. *Ph.D. Dissertation*, UNT, Denton, **2007**.

(12) Olmstead, M. M.; Jiang, F.; Attar, S.; Balch, A. L. *J. Am. Chem. Soc.* **2001**, *123*, 3260.

(13) Ishibashi, S.; Hasimoto, T.; Kohyama, T.; Terakura, K. *Phys. Rev. B* **2004**, *69, 155111*.

(14) Rand, B. P.; Xue, J.; Uchida, S.; Forrest, S. R. *J. Appl. Phys.* **2005**, *98*, 124902.

(15) Xue, J.; Rand, B. P.; Uchida, S.; Forrest, S. R. *J. Appl. Phys.* **2005**, *98*, 124903.

(16) Shirota, Y.; Kageyama, H. *Chem. Rev.* **2007**, *107*, 953.

(17) Coropceanu, V.; Cornil, J.; Da Silva Filho, D. A.; Olivier, R.; Brédas, S. J. *Chem. Rev.* **2007**, *107*, 926.

(18) Walzer, K.; Maennig, B.; Pfeiffer, M.; Leo, K. *Chem. Rev.* **2007**, *107*, 1233.

(19) Shaik, S. S. *J. Am. Chem. Soc.* **1982**, *104*, 5328.

(20) McConnell, H. M.; Hoffman, B. M.; Metzger, R. M. *Proc. Natl. Acad. Sci. U.S.A.* **1965**, *53*, 46.

(21) Miller, J. S.; Epstein, A. J. *J. Am. Chem. Soc.* **1987**, *109*, 3850.

(22) Islam, A.; Sugihara, H.; Hara, K.; Singh, L. P.; Katoh, R.; Yanagida, M.; Takahashi, Y.; Murata, S.; Arakawa, H. *New J. Chem.* **2000**, *24*, 343.

(23) Rabaa, H.; Cundari, T. R.; Omary, M. A. *Canad. J. Chem*. **2009**, *87*, 775.

(24) Kresse, G.; Furthmüller, J. *Computational Materials Science* **1996**, *6*, 15-50.

(25) Kresse, G.; Joubert, D. *Phys. Rev. B* **1999**, *59*, 1758.

(26) Perdew, J. P.; Burke, K.; Ernzerhof, M. *Phys. Rev. Lett.* **1996**, *77*, 3865.

(27) Monkhorst, H. J.; Pack, J. D. *Phys. Rev. B* **1976**, *13*, 5188.

(28) Cundari, T. R.; Chilukuri, B.; Hudson, J. M.; Minot, C.; Omary, M. A.; Rabaa, H. *Organometallics* **2010**, *29*, 795-800.

CHAPTER 4

HYBRID COINAGE METAL-ORGANIC MACROCYCLIC COMPLEXES AS NEW CLASSES OF ACTIVE MATERIALS FOR NOVEL MOLECULAR ELECTRONIC DEVICES: THE IMPORTACE OF CHARGE TRANSFER INTERACTIONS*

4.1 Introduction

Organic semiconductors are increasingly important research targets for development of optical and electronic devices[1-3]. A major challenge for development of organic semiconductors remains viable n-type materials. For example, the most efficient organic field-effect transistors (OFETs) are typically p-type, most notably pentacene-based, even with appropriate low-work-function electrodes[1-3]. Multiple kinds of modern organic electronic devices, however, require both p- and n-type semiconductors. Among such devices are complementary metal–oxide semiconductors (CMOS) circuits, which are the preferred style for digital logic and high performance analog circuitry. Most n-type organic semiconductors and devices developed to date suffer inferior stability, unreliable processing, poor synthetic yield with multiple reaction steps, and/or inefficient device performance except under vacuum[2]. To overcome these problems, hybrid inorganic–organic systems have been studied, e.g., using hydrogenated amorphous silicon (a-Si:H) or ZnO as n-type in conjunction with p-type organic semiconductors[3-5]. All-organic CMOS circuits have been reported[6-7] but the need to develop alternative classes of molecular materials remains keenly needed in part to address the aforementioned problems with n-type organic materials and devices.

---

* Work reported in this chapter was performed in collaboration with Dr. Chi Yang, Dr. Ravi Arvapally, Prof. Mohammad A. Omary at University of North Texas (UNT). Some experimental data contributed by these collaborators are included in this chapter in order to establish an appropriate context for the computational data.

We have recently reported that some Pt(II) metal-organic complexes act as electron donors (p-type) that form charge transfer complexes with quinone- or fluorenone-based organic acceptors (n-type)[8-13]. Synthesis of new classes of metal-organic materials by incorporation of transition metals into organic species improves the performance of conventional organic materials in terms of their conductivity, stability, processability, and chromaticity in devices such as OFETs[14], organic light emitting diodes (OLEDs)[15], and superconductors[16]. Several groups, including our own[7-11], have studied hybrid metal-organic molecular materials in the past for diverse applications such as phosphorescent[17-19], and magnetic[20] devices. Our group has studied cyclic trinuclear complexes of d-10 coinage metal ions - cyclo-$M_3(\mu\text{-}L)_3$ (M = coinage metal, L = anionic ligand) – bearing 9-membered rings {Figure 4.1 depicts two examples}. These d-10 complexes possess a variety of properties that can be both fine- and coarse-tuned via rational manipulation of metal, ligand and ligand substituents, e.g., π vs. Brønsted vs. Lewis acid-base chemistry, host/guest chemistry, supramolecular assemblies, M-M excimers, metalloaromaticity and metallophilic interactions[21-22]. These cyclo-$M_3(\mu\text{-}L)_3$ complexes exhibit photoluminescent, thermochromic, acid-base, and donor-acceptor properties[23]. The phenomenal properties of these coinage metal trimers arise from the interplay of d-d, d-π, π-π interactions among the metal-metal, ligand-ligand and metal-ligand moieties in the solid-state[12-14].

Our research seeks to develop structure (molecular and solid-state)-property (optoelectronic) relationships for cyclo-$M_3(\mu\text{-}L)_3$ trimers by comparing/replacing different coinage metals, ligands and substituents by closely synergizing molecular and solid-state simulations with spectroscopic and device fabrication experiments. Molecular Electrostatic Potential (MEP) and Positive Charge Attraction (PCA) calculations[24] indicate that cyclo-$M_3(\mu\text{-}L)_3$ trimers with Ag, triazolate (Tz) ligands and electron withdrawing $-CF_3$ substituents {viz

$[Ag(\mu\text{-}Tz\text{-}(CF_3)_2]_3\}$ give the most π-acidic or n-type character to the trimer molecule. In contrast, Au, imidazolate (Im) ligand and electron donating $-CH_3$ substituents, {viz $[Au(\mu\text{-}Im\text{-}2CH_3)]_3$}, yield the most π-basic trimer. Previous research indicates that the above mentioned trimers surpass organic semiconductor counterparts, perfluoropentacene and pentacene, with regard to π-acidity and π-basicity, respectively[22].

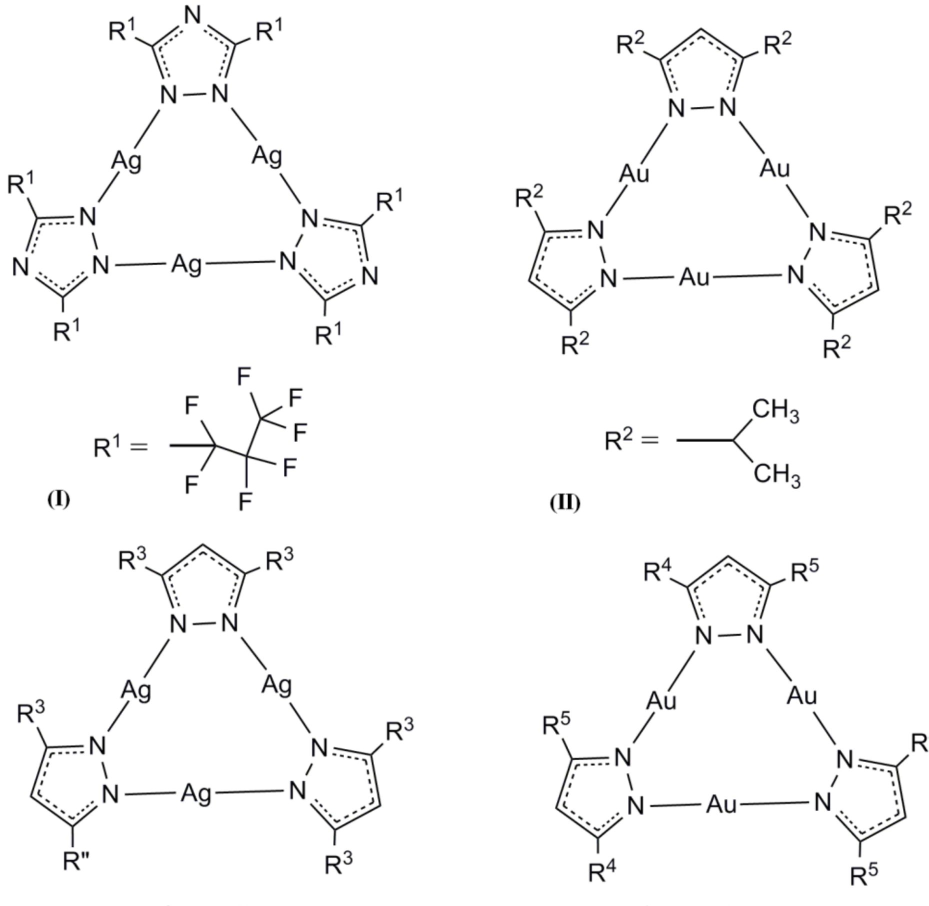

Figure 4.1. Molecular structures of cyclic trimers. (**I**) $[Ag(\mu\text{-}Tz\text{-}(n\text{-}C_3F_7)_2)]_3$. (**II**) $[Au(\mu\text{-}Pz\text{-}(i\text{-}C_3H_7)_2)]_3$. (**III**) $[Ag(\mu\text{-}Pz\text{-}(n\text{-}CF_3)_2)]_3$. (**IV**) $[Au(\mu\text{-}Pz\text{-}(3\text{-}[CH_3],5\text{-}[COOCH_2CH_3])]_3$. Structures (**I**)•(**II**) and (**III**)•(**IV**) are the two stacking charge transfer complexes studied in this chapter respectively. The structures on the left (**I**, **III**) containing silver (Ag) are *π-acid, n-type, acceptor* cyclotrimers. The structures on the right (**II**, **III**) containing gold (Au) are *π-base, p-type, donor* cyclotrimers.

In this chapter, a combined experimental and modeling study of the π-acid/π-base, n-type/p-type, donor/acceptor, Ag_3/Au_3 cyclotrimer materials is reported (Figure 4.1). Experimental luminescence studies were performed on $[Ag(\mu\text{-}Tz\text{-}(n\text{-}C_3F_7)_2)]_3$ • $[Au(\mu\text{-}Pz\text{-}(3\text{-}[CH_3],5\text{-}[COOCH_2CH_3]))]_3$ charge transfer cyclotrimer complexes. But, x-ray crystal structural characterization (only geometric information presented in the chapter) and computational modeling (molecular and solid-state) was performed on $[Ag(\mu\text{-}Tz\text{-}(R)_2]_3$ • $[Au(\mu\text{-}Pz\text{-}(R')_2)]_3$ trimers. Here (R), (R') = $(n\text{-}C_3F_7)$, $(i\text{-}C_3H_7)$ for x-ray structure determination and periodic modeling, while, (R), (R') = (CF_3/H), (CH_3/H) for molecular modeling. Smaller, non-bulky substituents (CF_3, CH_3, H) were used for molecular modeling to study the substituent effects and to save computational cost. Note that the luminescence studies were performed on complex [(**III**)•(**IV**)] while the structural determination and computational modeling was done on [(**I**)•(**II**)] complex. The reason for choosing different complexes for luminescence [(**III**)•(**IV**)] and structural [(**I**)•(**II**)] studies is the difficulty in obtaining the x-ray crystal structure for [(**III**)•(**IV**)] complex. Additionally the luminescence of [(**I**)•(**II**)] complex is very weak and cannot be used to make a realistic device (hence not presented in this chapter).

Molecular designs in which both p- and n-type metal-organic complexes of the type investigated here are wide-band-gap semiconductors are particularly attractive for novel light-emitting device concepts, such as phosphorescent p-n junction or bulk heterojunction OLEDs and ambipolar/light-emitting OFETs (i.e., organic light-emitting transistors or OLETs)[25].

4.2 Experimental Section

The work reported in this section was done by our experimental collaborators. Synthesis (not presented in this chapter), X-ray crystallography (only geometric information presented in the chapter) and electronic spectroscopy studies were done by Dr. Chi Yang and Dr. Ravi

Arvapally from the Omary group at UNT. As mentioned earlier, X-ray structure was determined for $[Ag(\mu\text{-Tz-}(n\text{-}C_3F_7)_2)]_3\bullet[Au(\mu\text{-Pz-}(i\text{-}C_3H_7)_2)]_3$ complex and the electronic spectroscopy studies were done on the $[Ag(\mu\text{-Pz-}(n\text{-}CF_3)_2)]_3\bullet[Au(\mu\text{-Pz-}(3\text{-}[CH_3],5\text{-}[COOCH_2CH_3]))]_3$ complex.

4.2.1 X-ray Crystal Structure of $[Ag(\mu\text{-Tz-}(n\text{-}C_3F_7)_2)]_3\bullet[Au(\mu\text{-Pz-}(i\text{-}C_3H_7)_2)]_3$ complex

A stacked material $[Ag(\mu\text{-Tz-}(n\text{-}C_3F_7)_2)]_3\bullet[Au(\mu\text{-Pz-}(i\text{-}C_3H_7)_2)]_3$ (Tz = triazolate; Pz = pyrazolate) {see Figure 4.1 for structure of the molecular components} was synthesized and structurally characterized by X-ray crystallography, Figures 4.2 and 4.3. The donor (gold) and acceptor (silver) trimers form vertical stacks one along the c axis of the unit cell. The closest Au-Ag distance in the synthesized stacked material is 3.044 Å. Experimental bond distances for Au-Ag bonds range from 2.7 to 3.6 Å[26]. Other selected bond distances and angles were listed in Figure 4.3.

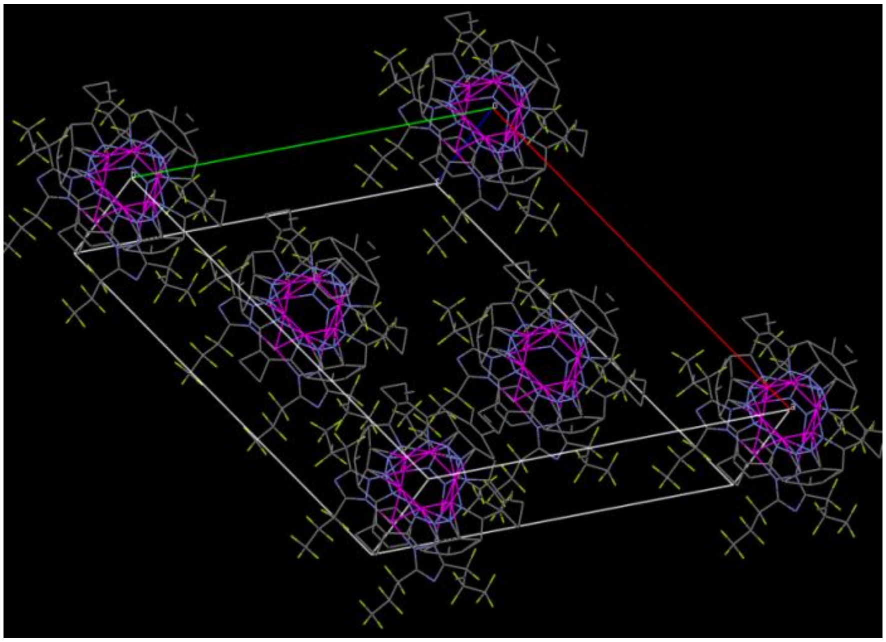

Figure 4.2. Unit cell structure of $[Ag(\mu\text{-Tz-}(n\text{-}C_3F_7)_2)]_3\bullet[Au(\mu\text{-Pz-}(i\text{-}C_3H_7)_2)]_3$. The Au trimer is over the Ag trimer in this figure. Hydrogens are omitted for clarity. The a,b,c axes of the unit cell are colored red, green, and blue, respectively. This structure was acquired by Dr. Chi Yang.

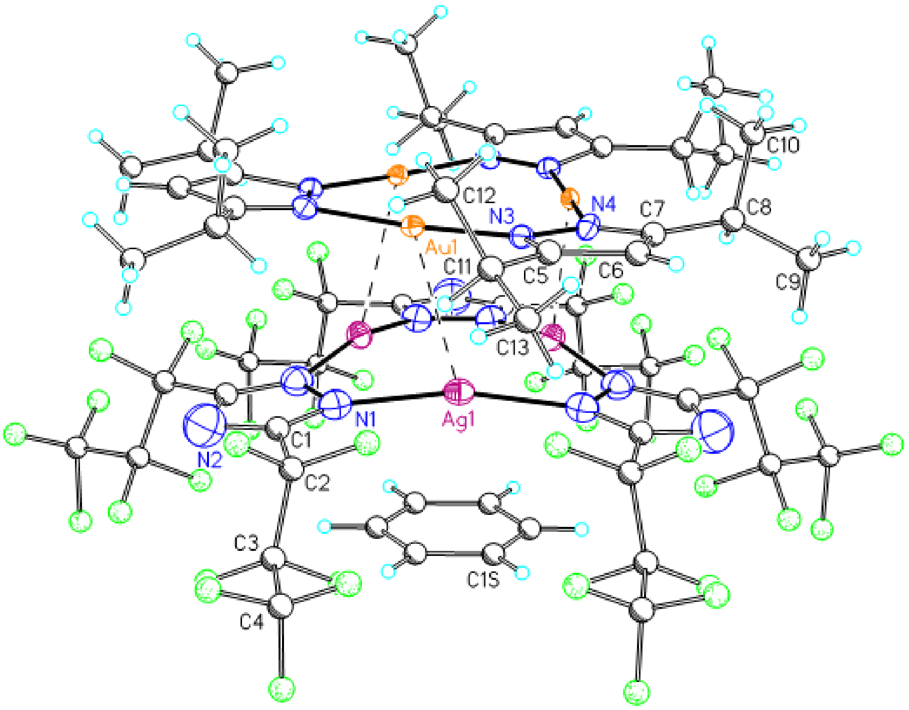

Figure 4.3. Molecular structure of [Ag(μ-Tz-(n-C_3F_7)$_2$)]$_3$•[Au(μ-Pz-(i-C_3H_7)$_2$)]$_3$. Major bond distances (Å) and angles (°): Ag(1)-N(1) 2.133(13), Au(1)-N(3) 1.95(2), Au(1)-N(4)#2, 2.03(2), Ag(1)-Au(1) 3.0446(14), Au(1)-Au(1)#2 3.3538(14), Au(1)#1-Au(1)-Ag(1) 74.003(15), Ag(1)-Au(1)-Au(1)#2 96.38(3). Solvent benzene can also be seen in the molecular structure. The hydrogen and fluorine atoms (not labeled in the figure) are colored blue and green, respectively. This structure was acquired by Dr. Chi Yang.

4.2.2 Electronic Spectroscopy of [Ag(μ-Pz-(n-CF_3)$_2$)]$_3$•[Au(μ-Pz-(3-[CH_3],5-[$COOCH_2CH_3$])]$_3$

Figure 4.4 shows the photoluminescence (PL) spectra for the solid Ag/Au binary adduct as well as equimolar admixtures of the Ag and Au trimers in solution. Neither p- or n-type trimer alone exhibits PL in dilute solution so the phosphorescent emissions observed are due to a charge transfer exciplex. The PL excitation, λ_{exc} (Figure 4.4) and absorption spectra (Figure 4.5) show maxima that are significantly red-shifted from the absorptions of dilute solutions of each trimer alone (Figure 4.5). This result suggests that the charge transfer interaction occurs even in the electronic ground state, which is qualitatively different from the behavior of metal-free organic fluorophores that are known to form exciplexes (or excimers), for which the electronic ground-state has long been presumed to be unbound[27].

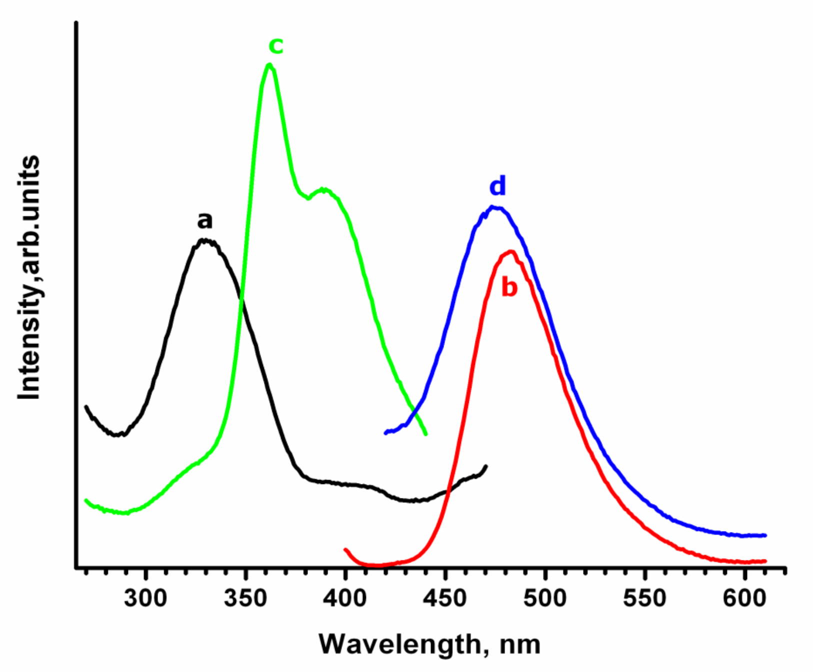

Figure 4.4. Photoluminescence spectra for Ag/Au binary adduct and their solution mixture. (a) solid, λ_{emi}= 480 nm (b) solid, λ_{exc}= 330 nm (c) solution λ_{emi}= 480 nm (d) solution, λ_{exc}= 400 nm. These data were acquired by Dr. Ravi Arvapally.

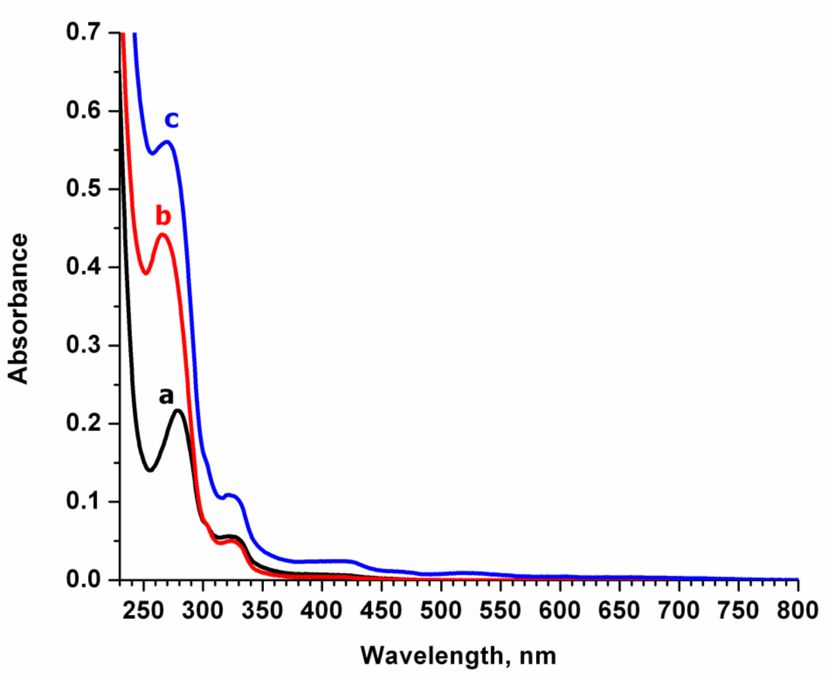

Figure 4.5. UV-Vis absorbance spectra of (a) 10^{-5} M [Ag(μ-Pz-(n-CF_3)$_2$)]$_3$ (b) 10-5 M [Au(μ-Pz-(3-[CH_3],5-[$COOCH_2CH_3$])]$_3$ [Ag(3,5-CF_3-Pz)]$_3$ (C) 1:1 Ag:Au solution mixture. These data were acquired by Dr. Ravi Arvapally.

4.3 Computational Modeling Section

Given the results form experimental electronic spectroscopy and x-ray crystal structure determination, we seek to better understand and explain the charge transfer interactions between Ag and Au trimers. The nature and degree of charge transfer (CT) interactions, their chemical origin, change in the interaction by changing the chemical components (ligands, substituents) of the trimers, effect of metallophilic bonds on CT, etc., were studied with combined periodic and molecular modeling methodology. Additionally, molecular calculations of spectroscopic properties (excitation and emission) were performed to compare with the experimental results. Some of the molecular modeling work presented in this section was performed by Dr. Sammer Tekarli of the Cundari group at UNT.

4.3.1 Periodic Modeling Methodology

Solid-state calculations are performed with density functional theory (DFT) using the Vienna Ab-initio Simulation Package (VASP)[28] which uses plane wave basis sets and Projector Augmented Wave (PAW) [29] methods for treating the interaction among the ions and valence electrons. The Kohn-Sham single electron wave functions are expanded by a series of plane waves with respective cutoff energies. The generalized gradient approximation (GGA) functional of Perdew, Burke and Ernzerhof (PBE) [30] was used for all the calculations. Although pure-DFT functions have well known limitations in describing localized states in wide band gap semiconductors and underestimates band gaps, the trend of calculated properties remains consistent with hybrid-DFT methods[31]. Considering the size of the unit cell lattice parameters and the number of atoms in each unit cell, the electronic wave functions are sampled in the first Brillouin zone on a k-point mesh size of 1x1x3 using the Monkhorst-Pack method[32]. The cut off energies used for the Ag/Au, Au, Ag trimers were 400, 750, 750 eV, respectively, as determined from corresponding energy convergence plots. Charge densities are viewed using Molekel[33].

4.3.2 Molecular Modeling Methodology

Geometry optimizations and single point calculations were performed using the Gaussian09 program[34]. Molecular DFT calculations utilized the B3LYP hybrid functional in conjunction with the CEP-31G(d) pseudopotential basis set[35-40], where (d) signifies addition of a d-polarization function to main group elements. Vibrational frequencies are calculated at all DFT optimized stationary points to confirm them as minima. Modeling of triplet species and computations of Frank-Condon vertical transitions were done using unrestricted Kohn-Sham methods.

4.3.3 Periodic Modeling of Charge Transfer Interactions

For solid-state calculations, we modified the experimental crystal unit cell (Figure 4.2) due to the disorder present in the x-ray structure (Figure 4.2, 4.3) and also due to memory constraints for the calculations. The lattice parameters are not changed, but the molecules in the unit cell are reduced to a single (non-disordered) molecular stack inside the unit cell (Figure 4.6). This assumption is not expected to fundamentally change the present results since the conduction mechanism is intra-stack not inter-stack considering the van der Waals radii of the entire $[Ag(\mu\text{-}Tz\text{-}(n\text{-}C_3F_7)_2)]_3 \bullet [Au(\mu\text{-}Pz\text{-}(i\text{-}C_3H_7)_2)]_3$ complex. All periodic simulations were single point calculations, performed on non-optimized geometries. The molecular stacking geometries of the cyclo-trimers in the built unit cells (Figure 4.6) were obtained from the disorder cleaned experimental crystal structure (Figure 4.3).

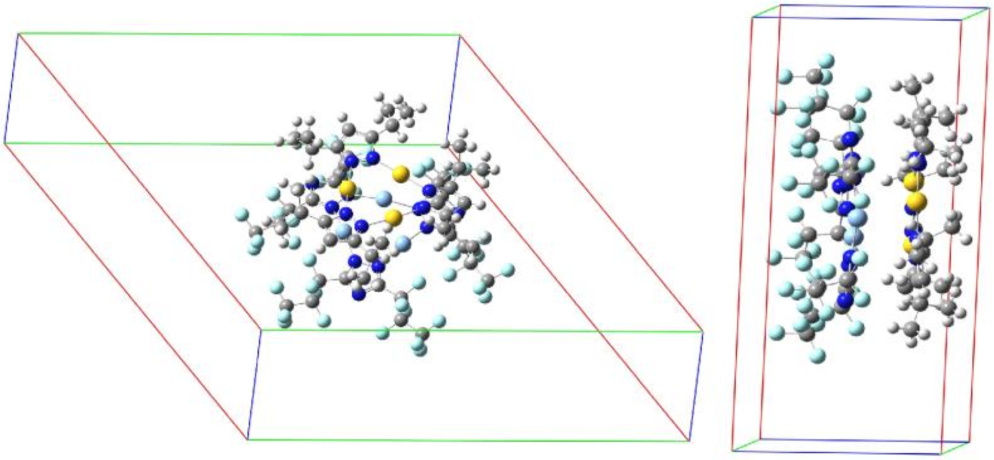

Figure 4.6. Top and side views of modified unit cell structure of [Ag(μ-Tz-(n-C_3F_7)$_2$)]$_3$•[Au(μ-Pz-(i-C_3H_7)$_2$)]$_3$. The Au trimer is over the Ag trimer in the figure to the left. The a,b,c axes of the unit cell are colored red, green, and blue, respectively. Note that the trimers and stacking geometries were taken from the X-ray crystal structure.

For simplistic representation, the π-basic [Au(μ-Pz-(i-C_3H_7)$_2$)]$_3$ trimer is denoted as donor (**D**) and the π-acidic [Ag(μ-Tz-(n-C_3F_7)$_2$)]$_3$ trimer is denoted as acceptor (**A**). With the assumption made above, a total of 3 unit cells were built using the lattice parameters of the experimental unit cell (Figure 4.2).

(i) **D•A** unit cell with [Au(μ-Pz-(i-C_3H_7)$_2$)]$_3$•[Ag(μ-Tz-(n-C_3F_7)$_2$)]$_3$ trimer stacks (Figure 4.6)

(ii) **D** unit cell with only the [Au(μ-Pz-(i-C_3H_7)$_2$)]$_3$ trimer. (this cell is made by deleting the Ag trimer from the **D•A** unit cell)

(iii) **A** unit cell with only the [Ag(μ-Tz-(n-C_3F_7)$_2$)]$_3$ trimer in the cell. (this structure is made by deleting the Au trimer from the **D•A** unit cell)

Single point calculations on the 3 built unit cells were done using plane-wave DFT. The density of states (DOS) obtained from the calculations are depicted in the Figure 4.7, which summarizes three different calculations, one each on the **D**, **A** and **D•A** stacks, respectively.

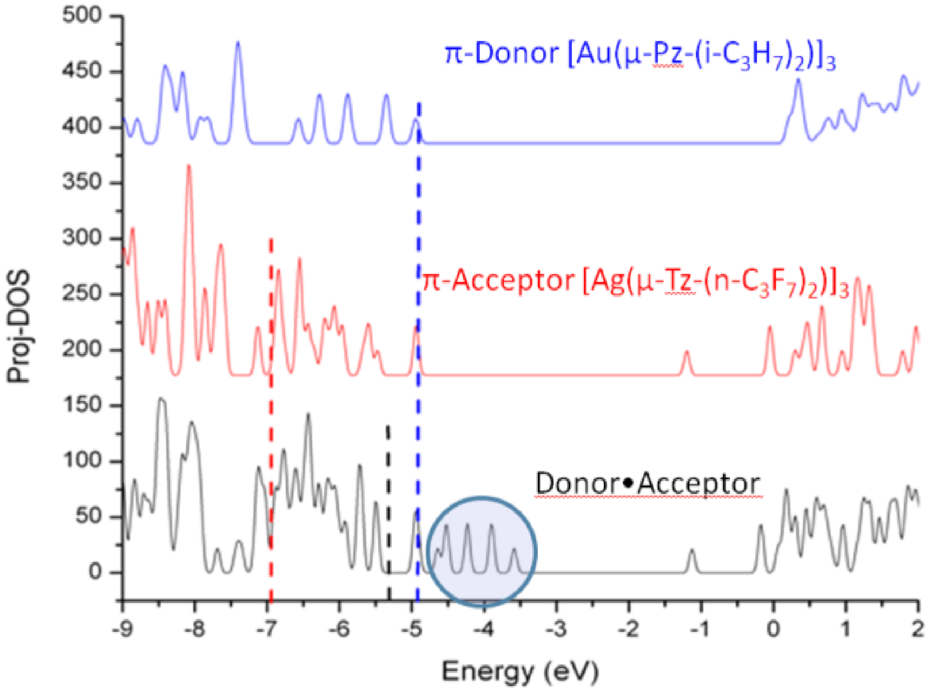

Figure 4.7. Calculated density of states (DOS) for **D** (blue), **A** (red) and **D•A** (black) unitcells. The dotted lines indicate the Fermi levels of the respective materials. The circled region indicates charge transfer states in the **D•A** system.

Comparing the DOS of **D**, **A**, and **D•A**, two main points of interest can be noted. First, the Fermi level (E_f) of **D•A** is shifted with respect to E_f for **D** and **A**. The Fermi energy (-4.9 eV) for isolated **D** is higher than the Fermi energy (-6.9 eV) for isolated **A**. Interestingly, the Fermi energy (-5.3 eV) of **D•A** lies in between the **D** and **A** Fermi energies. These E_f dispositions are consistent with the flow of electrons from **D** → **A** (i.e., Au trimer to Ag trimer within a stack). A second point of interest is the presence of charge transfer (CT) states[41-42] (circled region on DOS of **D•A** system in Figure 4.7). The CT states can be viewed as mid-gap states of the **D•A** system. These states are not seen in either the DOS of isolated **D** or isolated **A** (Figure 4.7), but exclusively in **D•A**. The presence of CT states for **D•A** supports the inference of intra-stack CT of electrons from **D** → **A** that was deduced from the calculated Fermi energies.

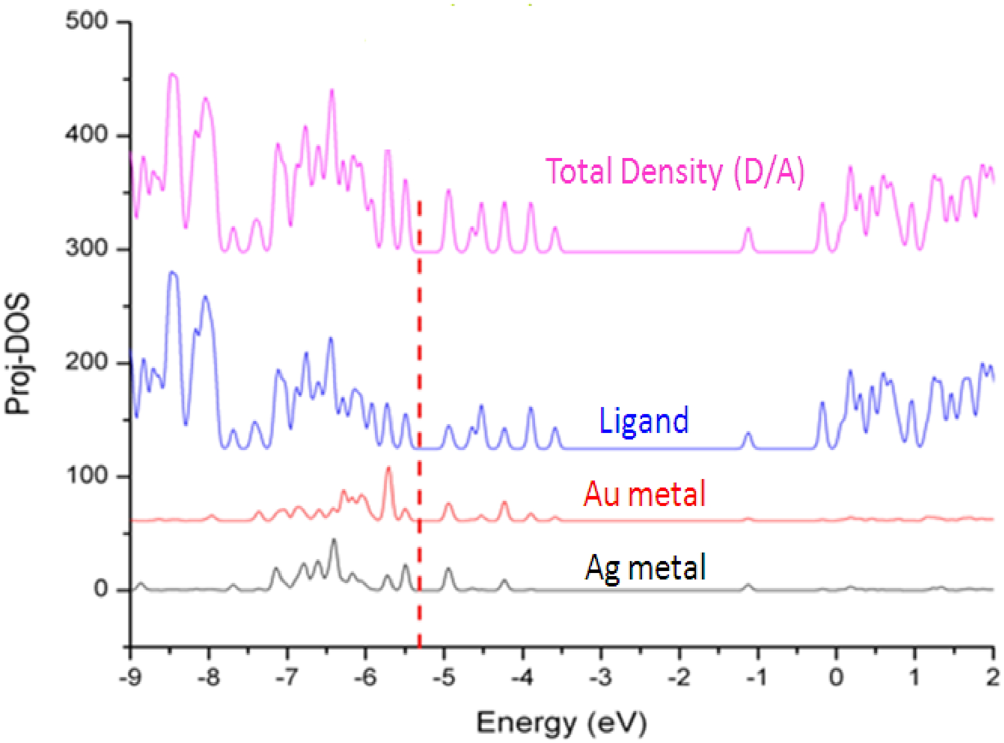

Figure 4.8. DOS contributions in **D•A** stack from ligand (blue), Au (red), Ag (black) which add up to give total density of states (magenta). Dotted line indicates the Fermi energy of **D•A**.

To further understand the nature of charge transfer behavior in the **D•A** stack, the total DOS has been decomposed to respective contributions from the metals Ag, Au and ligands, which is depicted in Figure 4.8. A closer inspection of the population projections of metal (Ag and Au individually) and ligand (via subtraction of Ag and Au projections from the total) contributions to the total DOS indicate that near the Fermi level, and in particular near the CT states, that while there are contributions from both the ligands and the metals there is considerably more contribution from the ligands. These results suggest that the type of CT between these trimers is primarily of the ligand to ligand charge transfer (LLCT) type augmented by some metal to ligand charge transfer (MLCT) character.

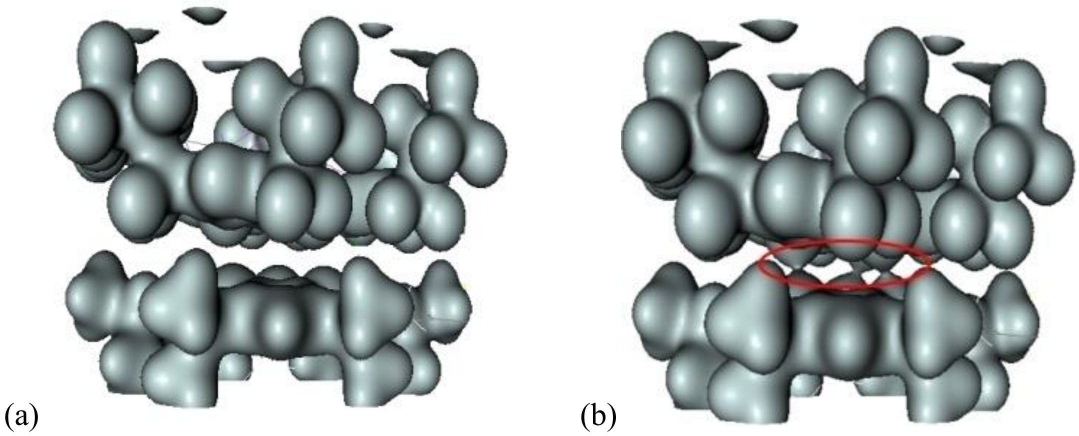

Figure 4.9. Mapped charge density of **D•A** stacks; (a) isosurface value = 0.04 (left) (b) isosurface value = 0.02 (right).

Charge densities obtained from the solid-state calculations are mapped in Figure 4.9. What is interesting is that there is no evidence of direct interaction between the Ag and Au trimers near a typical covalent bond density isovalue (0.04 in Figure 4.9(a)). However, overlap of the electron density envelopes of the individual molecular components within the stack can be seen closer to an isovalue more appropriate for mapping van der Waals radii (0.02 in Figure 4.9(b)). The charge density analysis thus suggests that the interaction between the trimers arises from non-covalent forces. This evidence further supports a proposal that the interaction among the trimers within a stack is primarily due to charge transfer.

The effect of donor-acceptor interaction with respect to distance between the trimers is tested within the solid-state framework, Figure 4.6. This test is important because one expects the strength of interaction between trimer units to change with the intra-stack distance between them. Moreover, the inter-trimer distance may be experimentally tuned via the choice of ligand substituents[24]. The distances between the **D** and **A** stacks are analyzed in the range of 2.7 to 3.6 Å. These distances correspond to the experimental range of Ag-Au bond lengths from the

Cambridge Structural Database[26]. Density of states (DOS) is chosen as the determining parameter to examine the charge transfer behavior.

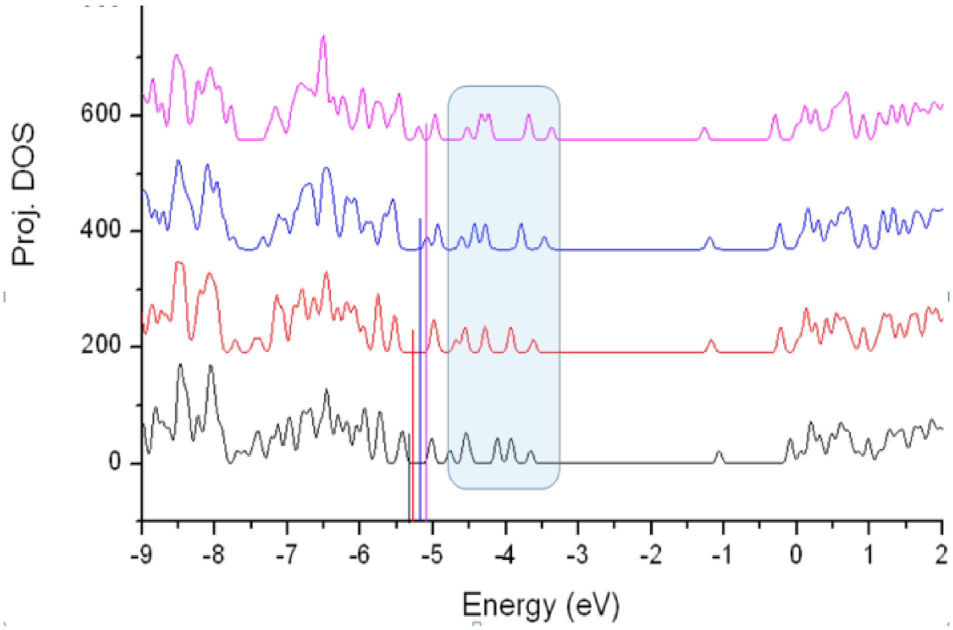

Figure 4.10. Comparison of DOS of **D•A** materials at different plane-to-plane separations between D and A.

Interestingly, no notable differences are observed in the DOS of the **D•A** system as a function of **D**/**A** separation. The CT states (shaded region in Figure 4.10) are present in the DOS of the **D•A** system within the experimentally relevant Ag-Au range. Further, the changes in total energy and Fermi energy at different separations within the computed range have been noted (Table 4.1). The Fermi energy of **D•A** increases with increase in distance between the trimers. The minimum total energy is found at 3.2 Å in contrast to the experimental distance of 3.044 Å. However, the plane-wave DFT simulations indicate a very soft potential surface in the **D•A** systems, which is consistent with the wide range of experimental separations that may be observed in solid-state structures of coinage metal trimer materials. One may envisage that that the degree of charge transfer in the **D•A** system will be less sensitive to changes in **D**/**A** separation than would be the case if the bonding were dominated by ionic/covalent interactions, further supporting the hypothesis as to the CT mechanism of intra-stack conduction for these materials.

Table 4.1. PW-DFT calculated Fermi energies and total energies of the D•A materials at respective distances between the trimers. *Experimental distance

Distance (Å)	E-Fermi (eV)	E-Total (eV)
2.7	-5.34	-908.84
2.8	-5.34	-909.28
2.9	-5.31	-909.73
3.044*	-5.28	-910.03
3.1	-5.26	-910.10
3.2	-5.23	-910.12
3.3	-5.17	-910.06
3.4	-5.16	-910.00
3.6	-5.07	-909.45

To further understand CT interaction between **D** and **A**, we modified the trimers by replacing their substituents with hydrogens. The i-C_3H_7 on the pyrazolate ligands of the Au_3 trimer and the n-C_3F_7 on the triazolate ligands of the Ag_3 trimer were replaced with hydrogen, thus reducing the donor (p-type) ability of the Au_3 trimer and acceptor (n-type) ability of the Ag_3 trimer respectively. All unit cell, stacking geometries and calculation parameters are otherwise retained identical to the previous simulations. Calculations are then performed for the hydrogen-decorated $\mathbf{D_H}$, $\mathbf{A_H}$ and $\mathbf{D_H}$•$\mathbf{A_H}$ systems. The DOS of $\mathbf{D_H}$•$\mathbf{A_H}$ and **D•A** are depicted in Figure 4.11. The most exciting finding from the DOS comparison of these systems is the absence of CT peaks (circled region) for $\mathbf{D_H}$•$\mathbf{A_H}$. Also, the Fermi energy of $\mathbf{D_H}$•$\mathbf{A_H}$ (-5.6 eV) lies below E_f for both $\mathbf{D_H}$ (-5.4 eV) and $A_{\mathbf{H}}$ (-5.2 eV) materials (not shown). This disposition is inconsistent with a flow of electrons (charge transfer) from $\mathbf{D_H} \rightarrow \mathbf{A_H}$. The absence of mid-gap states and the Fermi energies in $\mathbf{D_H}$•$\mathbf{A_H}$ clearly indicates that substituents on the ligands of Ag and Au trimers play a key role in charge transfer and hence conductive properties of these materials.

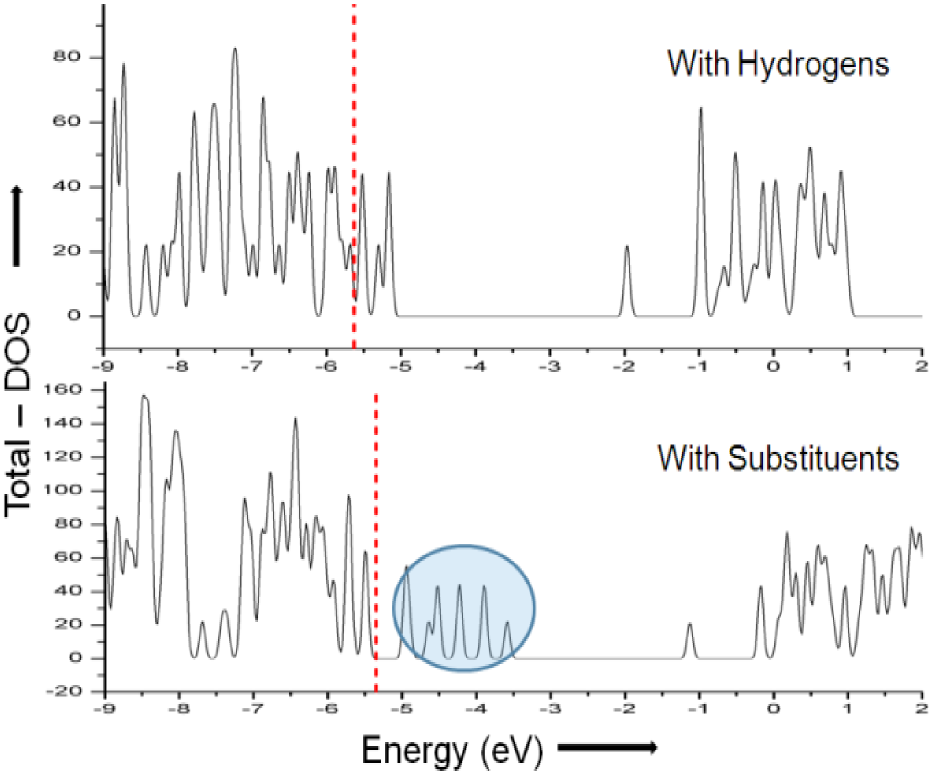

Figure 4.11. DOS of Au_3•Ag_3 trimers. *On the bottom*: DOS of **D•A** unit cell with substituents on the trimer ligands. *On the top*: DOS of $\mathbf{D_H}$•$\mathbf{A_H}$ unit cell where substituents on the trimer ligands were replaced by hydrogens. The dotted lines (red) denote the Fermi energies. The circled region highlights the CT states.

4.3.4 Molecular Modeling of Charge Transfer Interactions

Given the difficulties in analyzing atomic populations within the plane-wave DFT approximation, the solid-state simulations were supplemented by molecular models using Gaussian-based DFT techniques[34-40]. This dual approach has been used with success in previous studies[8] of related CT materials. For the purpose of saving computational resources, we replaced the bulky substituents, n-C_3F_7 and i-C_3H_7, on $[Ag(\mu\text{-Tz})]_3$ and $[Au(\mu\text{-Pz})]_3$ trimers with $-CF_3$ and $-CH_3$, respectively. In addition to the $[Ag(\mu\text{-Tz})]_3$ • $[Au(\mu\text{-Pz})]_3$, molecular calculations were performed on $[Ag(\mu\text{-Tz})]_3$ • $[Au(\mu\text{-Im}]_3$ CT complexes for comparison as the later were found to have better π-acidic and π-basic properties than the former respectively. The calculated atomic charges derived from a natural population analysis, Table 4.2, indicate that there is a ca. six times the charge transfer for the substituted dimer of trimers (DOT) in comparison with non-substituted DOT ($[Ag(\mu\text{-}Tz)]_3$•$[Au(\mu\text{-}Im)]_3$) and fifteen times the amount of CT as the organic (Pentacene• Perfluoropentacene) counterpart.

Table 4.2. Calculated charge transfer for dimer of trimer models and an organic counterpart (last entry). [a]Charge transfer is measured in electron units. Computational data were partly acquired by Dr. Sammer Tekarli.

Dimer Model	Charge Transfer[a]
$[Ag(\mu\text{-}Tz)]_3$ • $[Au(\mu\text{-}Im)]_3$	0.036
$[Ag(\mu\text{-}Tz(CF_3)_2]_3$ • $[Au(\mu\text{-}Im(CH_3)_2]_3$	0.219
$[Ag(\mu\text{-}Tz(CF_3)_2]_3$ • $[Au(\mu\text{-}Pz(CH_3)_2]_3$	0.116
[Pentacene] • [Perfluoropentacene]	0.014

Furthermore, the CT for $[Ag(\mu\text{-}Tz(CF_3)_2]_3$•$[Au(\mu\text{-}Im(CH_3)_2]_3$ is 0.219 e^- while it is 0.036 e^- (six times lower) for $[Ag(\mu\text{-}Tz)]_3$ • $[Au(\mu\text{-}Im)]_3$. Also, the calculated CT of the organic counterpart is 0.014 e^- which is 2.5 times lower than $[Ag(\mu\text{-}Tz)]_3$•$[Au(\mu\text{-}Im)]_3$ with 0.036 e^-. Taken together, the large CT differences further corroborate the plane-wave DOS results, which suggest that the CT between **D** and **A** is significantly modified by the ligands and their substituents.

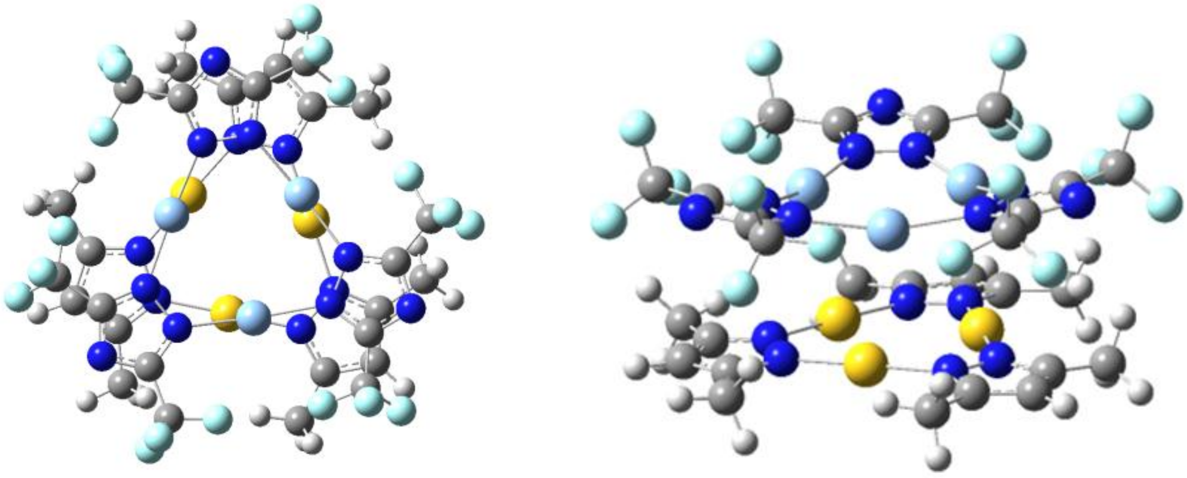

Figure 4.12. The optimized singlet (S = 0) geometry of a molecular dimer of trimer (DOT) model, $[Ag(\mu\text{-}Tz(CF_3)_2]_3$•$[Au(\mu\text{-}Pz(CH_3)_2]_3$. The atoms are colored grey (C), white (H), blue (N), steel blue (Ag) and powder blue (F). Computational data was acquired by Dr. Sammer Tekarli

4.3.5 Molecular Modeling of Electronic Excitations

The results summarized in Table 4.3 show that the excitation energies of the DOT models are significantly lower than the excitation energy for a single trimer. For example, the excitation energy for $[Ag(\mu\text{-}Tz(CF_3)_2]_3$•$[Au(\mu\text{-}Pz(CH_3)_2]_3$ is 3.83 eV while the excitation energy for $[Ag(\mu\text{-}Tz(CF_3)_2]_3$ and $[Au(\mu\text{-}Pz(CH_3)_2]_3$ are 4.63 and 4.56 eV, respectively. The lower excitation energy of the DOT correlates with experimental observations (vide infra) and is consistent with the Fermi level analysis in section 4.3.3.

Table 4.3. Excitation and emission energies of each dimer of trimer model and organic counterparts in eV. Computational data were partly acquired by Dr. Sammer Tekarli.

Model	Excitation $S_0 \rightarrow T_1$	Emission $T_1 \rightarrow S_0$	Stokes Shift
$[Ag(\mu\text{-}Tz)]_3$	5.81	2.72	3.10
$[Au(\mu\text{-}Im)]_3$	4.81	4.10	0.71
$[Ag(\mu\text{-}Tz(CF_3)_2)]_3$	4.63	2.72	1.91
$[Au(\mu\text{-}Im(CH_3)_2)]_3$	4.21	1.87	2.34
$[Au(\mu\text{-}Pz(CH_3)_2]_3$	4.56	2.85	1.71
$[Ag(\mu\text{-}Tz)]_3$ • $[Au(\mu\text{-}Im)]_3$	4.27	3.01	1.27
$[Ag(\mu\text{-}Tz(CF_3)_2]_3$ • $[Au(\mu\text{-}Im(CH_3)_2]_3$	3.66	2.03	1.63
$[Ag(\mu\text{-}Tz(CF_3)_2]_3$ • $[Au(\mu\text{-}Pz(CH_3)_2]_3$	3.83	2.28	1.55
Pentacene	0.89	0.48	0.41
Perfluoropentacene	0.75	0.32	0.43
[Pentacene] • [Perfluoropentacene]	1.18	0.19	0.99

4.4 Summary and Conclusions

Summarizing the work in this chapter, experimental (by Chi Yang and Ravi Arvapally in the Omary group at UNT) and computational studies (some work by Sammer Tekarli in the Cundari group at UNT) were performed on [cyclo-Ag(μ-L-(R)$_2$]$_3$ • [cyclo-Au(μ-L'-(R')$_2$)]$_3$ charge transfer complexes (where L= Triazolate(Tz)/Pyrazolate(Pz); L'= Pyrazolate(Pz); R= (n-C_3F_7)/(CF_3)/(H); R'= (i-C_3H_7)/(3-[CH_3],5-[$COOCH_2CH_3$])/(CH_3), (H)), Figure 4.1.

X-ray structure was determined for the [Ag(μ-Tz-(n-C_3F_7)$_2$)]$_3$•[Au(μ-Pz-(i-C_3H_7)$_2$)]$_3$ complex. In the solid-state, donor (gold) and acceptor (silver) trimers form vertical stacks along the c axis of the unit cell. The closest Au-Ag distance in the synthesized stacked material is 3.044 Å (Figures 4.2, 4.3). Electronic spectroscopy studies were done on the [Ag(μ-Pz-(n-CF_3)$_2$)]$_3$•[Au(μ-Pz-(3-[CH_3],5-[$COOCH_2CH_3$])]$_3$ complex. Results indicate that neither the Ag nor Au trimer exhibits photoluminescence in dilute solutions by themselves. However, phosphorescent emissions are observed in Ag•Au complex indicating that the emissions are due to a charge transfer exciplex.

To better understand and explain the charge transfer (CT) interactions between Ag and Au trimers computational studies at periodic and molecular levels were done on individual and stacked complexes of Ag and Au trimers. Solid-state studies were performed on built crystal (based on X-ray geometries) unit cells of [Ag(μ-Tz-(n-C_3F_7)$_2$)]$_3$•[Au(μ-Pz-(i-C_3H_7)$_2$)]$_3$ complexes. Solid-state simulations support a dominant conduction mechanism from the donor (**D**) Au trimer to the acceptor (**A**) Ag trimer through a charge transfer mechanism. The CT is supported by DOS analysis of **D**, **A** and **D•A** systems which suggest that the type of CT between these trimers is primarily of the ligand to ligand charge transfer (LLCT) type augmented by some metal to ligand charge transfer (MLCT) character. Calculations also suggest that substituents on the ligands are a key ingredient in tuning the amount of CT in these materials through their impact on the acid/base properties of the coinage metal components in the stacks. Finally, molecular calculations on multiple Ag, Au, Ag•Au trimers (vide infra) agrees with the experimental and periodic modeling studies suggesting a charge transfer mechanism.

In conclusion, experimental and computational studies on [cyclo-Ag(μ-L-(R)$_2$]$_3$ • [cyclo-Au(μ-L'-(R')$_2$)]$_3$ stacked materials disclosed in this paper provide a proof of concept that molecular designs in which both p- and n-type metal-organic complexes of the type investigated here are wide-band-gap semiconductors and are particularly attractive for novel light-emitting device concepts, such as phosphorescent p-n junction or bulk heterojunction OLEDs and ambipolar/light-emitting OFETs (i.e., organic light-emitting transistors or OLETs).

4.5 Chapter References

(1) Chua, L.; Zaumseil, J.; Chang, J.; Ou, E. C. -W.; Ho, P. K. -H.; Sirringhaus, H.; Friend, R.H. *Nature* **2005**, *434*, 194.

(2) Newman, C. R.; Frisbie, C. D.; da, S. F.; Bredas, J. -L.; Ewbank, P. C.; Mann, K. R. *Chem. Mater.* **2004**, *16*, 4436.

(3) Wang, L.; Yoon, M.; Lu, G.; Yang, Y.; Facchetti, A.; Marks, T. J. *Nat. Mater.* **2006**, *5*, 893.

(4) Kagan, C. R.; Mitzi, D. B.; Dimitrakopoulos, C. D. *Science* **1999**, *286*, 945.

(5) Mourey, D. A.; Park, S. K.; Zhao, D. A.; Sun, J.; Li, Y. V.; Subramanian, S.; Nelson, S. F.; Levy, D. H.; Anthony, J. E.; Jackson, T. N. *Org. Elec.* **2009**, *10*, 1632.

(6) Zhang, X.; Potscavage Jr.,W. J. P.; Choi, S.; Kippelen, B. *Appl. Phys. Lett.* **2009**, *94*, 043312.

(7) Dzwilewski, A.; Matyba, P.; Edman, L. *J. Phys. Chem. B* **2010**, *114*, 135.

(8) T. R. Cundari, B. Chilukuri, J. M. Hudson, C. Minot, M. A. Omary and H. Rabaa, *Organometallics* **2010**, *29*, 795.

(9) Hudson, J. M. *Ph.D. Dissertation*, University of North Texas, Denton, **2007**, Chapter 4, 62.

(10) Omary, M. A., *U.S. Patent* Application Number: 61/24,878; October 1, **2009**.

(11) Rabaa, H.; Cundari, T. R.; Omary, M. A. *Canad. J. Chem*. **2009**, *87*, 775.

(12) Chen, W.; Reinheimer, E. W.; Dunbar, K. R.; Omary, M. A. *Inorg. Chem.* **2006**, *45*, 2770.

(13) Smucker, B. W.; Hudson, J. M.; Omary, M. A.; Dunbar, K. R. *Inorg. Chem.* **2003**, *42*, 4714.

(14) Caseri, W. R.; Chanzy, H. D.; Feldman, K.; Fontana, M.; Smith, P.; Tervoort, T. A.; Goossens, J. G. P.; Meijer, E. W.; Schenning, A. P. H. J.; Dolbnya, I. P.; Debije, M. G.; de Haas, M. P.; Warman, J. M.; van de Craats, A. M.; Friend, R. H.; Sirringhaus, H.; Stutzmann, N. *Adv. Mater.* **2003**, *15*, 125.

(15) D'Andrade, B. W.; Forrest, S. R. *Adv. Mater.* **2004**, *16*, 1585.

(16) Faulmann, C.; Cassoux, P. *Prog. Inorg. Chem.* **2004**, *52*, 399–489.

(17) Kalyanasundaram, K.; Grätzel, M. *Coord. Chem. Rev.* **1998**, *177*, 347-414.

(18) Ma, Y.; Zhang, H.; Shen, J.; Che, C. *Synth. Met.* **1998**, *94*, 245-248.

(19) Yam, V. W-W.; Lo, K. K-W. *Chem. Soc. Rev.* **1999**, *28*, 323-334.

(20) Matsumoto, Y.; Murakami, M.; Shono, T.; Hasegawa, T.; Fukumura, T.; Kawasaki, M.; Ahmet, P.; Chikyow, T.; Koshihara, S.; Koinuma, H. *Science* **2001**, *291*, 854-856.

(21) Elbjeirami, O.; Gonser, M. W. A.; Stewart, B. N.; Bruce, A. E.; Bruce, M. R. M.; Cundari, T. R.; Omary, M. A. *Dalton Transactions* **2009**, 1522-1533.

(22) Grimes, T.; Omary, M. A.; Dias, H. V. R.; Cundari, T. R. *The Journal of Physical Chemistry A* **2006**, *110*, 5823-5830.

(23) Omary, M. A.; Rawashdeh-Omary, M.; Gonser, M. W. A.; Elbjeirami, O.; Grimes, T.; Cundari, T. R.; Diyabalanage, H. V. K.; Gamage, C. S. P.; Dias, H. V. R. *Inorg. Chem.* **2005**, *44*, 8200-8210.

(24) Tekarli, S. M.; Cundari, T. R.; Omary, M. A. *J. Am. Chem. Soc.* **2008**, *130*, 1669-1675.

(25) Capelli, R.; Dinelli, F.; Loi, M. A.; Murgia, M.; Zamboni, R.; Muccini, M. *J. Phys.: Condens. Matter* **2006**, *18*, S2127–S2138.

(26) Allen, F., *Acta Cryst.* **2002***, 58*, 380-388.

(27) N. J. Turro, *Molecular Photochemistry*, W. A. Benjamin: New York, N. Y., **1965**, pp 194-245.

(28) Kresse, G.; Furthmüller, J. *Computational Materials Science* **1996***, 6*, 15-50.

(29) Kresse, G.; Joubert, D. *Phys. Rev. B* **1999***, 59*, 1758.

(30) Perdew, J. P.; Burke, K.; Ernzerhof, M. *Phys. Rev. Lett.* **1996***, 77*, 3865.

(31) Brothers, E. N.; Izmaylov, A. F.; Normand, J. O.; Barone, V.; Scuseria, G. E. *J. Chem. Phys.* **2008***, 129*, 011102-4.

(32) Monkhorst, H. J.; Pack, J. D. *Phys. Rev. B* **1976***, 13*, 5188.

(33) Portmann, S.; Luthi, Peter, H. *CHIMIA International Journal for Chemistry* **2000***, 54*, 766-770.

(34) Frisch, M. J.; et al. Gaussian 09, Revision A.1, Gaussian, Inc., Wallingford CT **2009**.

(35) Stephens, P. J.; Devlin, F. J.; Chabalowski, C. F.; Frisch, M. J. *J. Phys. Chem.* **1994***, 98*, 11623-11627.

(36) Becke, A. D. *Phys. Rev. A* **1988***, 38*, 3098.

(37) Lee, C.; Yang, W.; Parr, R. G. *Phys. Rev. B* **1988***, 37*, 785.

(38) Stevens, W. J.; Krauss, M.; Basch, H.; Jasien, P. G. *Can. J. Chem.* **1992***, 70*, 612.

(39) Stevens, W. J.; Basch, H.; Krauss, M. *J. Chem. Phys.* **1984***, 81*, 6026-6033.

(40) Cundari, T. R.; Stevens, W. J. *J. Chem. Phys.* **1993***, 98*, 5555-5565.

(41) Giordano, L.; Pacchioni, G. *Physical Chemistry Chemical Physics* **2006***, 8*, 3335-3341.

(42) Di Valentin, C.; Pacchioni, G.; Selloni, A. *Phys. Rev. Lett.* **2006***,* 97, 166803-4.

CHAPTER 5

ELECTRONIC STRUCTURE OF CYCLIC TRINUCLEAR AU(I) CARBENIATE COMPLEXES: INSIGHTS FOR STRUCTURE/LUMINESCENCE/CONDUCTIVITY RELATIONSHIPS*

5.1 Introduction

Incorporation of a transition metal into organic materials can substantially impact their optical, electronic and/or magnetic properties[1,2]. For example, cyclic trinuclear coinage metal complexes display a variety of photophysical properties including solvoluminescence, rigidochromism and vapochromism[3]. The fundamental significance of cyclic trinuclear d-10 complexes spans multiple areas of chemical bonding, such as metallophilic and excimeric bonding, π acid-base interactions and metalloaromacity[4]. The focal point of this study are cyclic trinuclear gold carbeniate complexes or $[Au_3(RN{=}COR')_3]$ (where R and R' are a selection of substituents) or Au_3Cb_3 (Au_3 and Cb_3 represent gold atoms and carbeniate ligands, respectively) complexes, which contain two-coordinate Au^I metal centers, connected by C=N bridging ligands, Figure 5.1[5].

The photophysical and electronic properties of trinuclear Au^I complexes are impacted by solid state intermolecular interactions, which are mediated by aurophilic Au--Au interactions[3-6]. The extent of these intermolecular interactions are also modulated by the bulkiness of the ligand substituents (R, R'), which may retard or enhance inter-trimer interactions, yielding structures of dimers of trimers, extended chains, etc. in the solid state, as shown in Figure 5.2. Several examples of trimeric gold carbeniates have been reported[1,5-8]. Balch et al. elaborated on the

---

* Work reported in this chapter was performed in collaboration with Roy N. McDougald, and Prof. Mohammad A. Omary (UNT) as well as Dr. Huiping Jia and Prof. Bruce E. Gnade (UTD). Some experimental data contributed by these collaborators are included in this chapter to establish an appropriate context for the computational data.

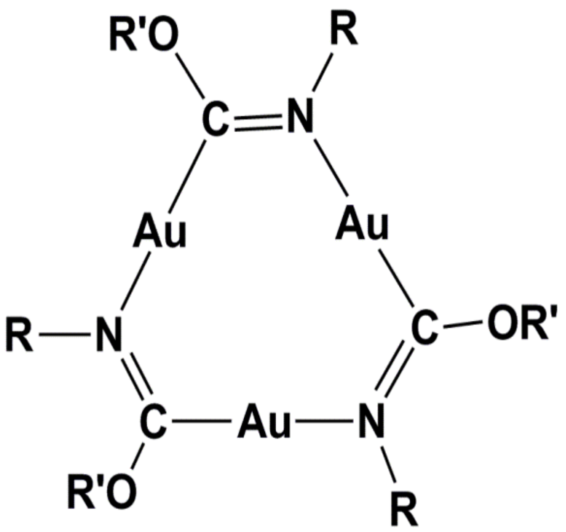

Figure 5.1. Molecular structure of the trinuclear Au(I) carbeniate complexes [Au_3(RN=COR')$_3$]. R and R' represents different substituents on the carbeniate ligands.

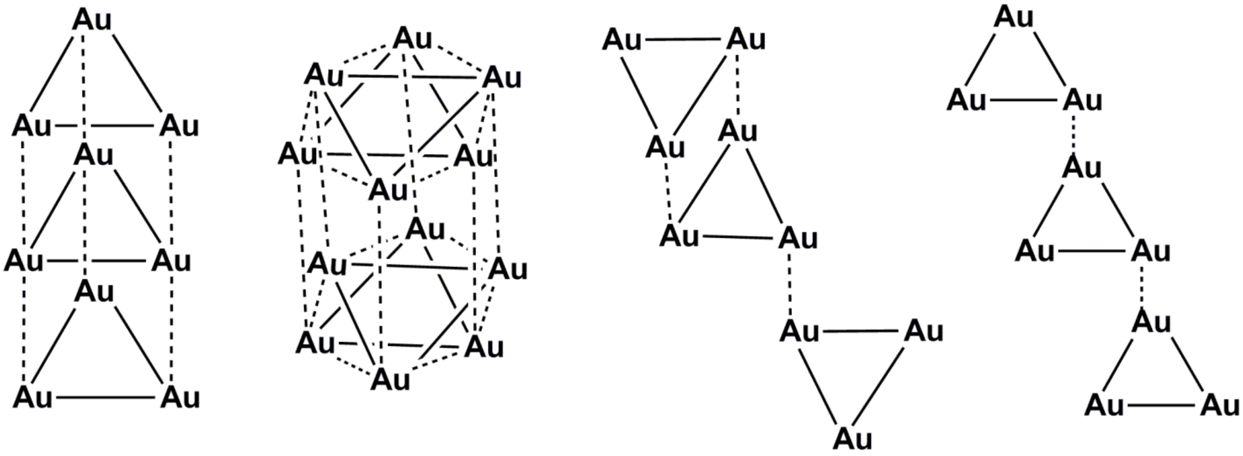

I **II** **III** **IV**

Figure 5.2. Stacking arrangements found in [Au_3(RN=COR')$_3$] complexes. Trinuclear complexes are represented by triangles and inter-trimer aurophilic interactions by dashed lines. Polymorphs are named as eclipsed (I); disordered staggered (II); chair conformation (III); and stair-step conformation (IV).

[Au_3(MeN=COMe')$_3$] series for which steric bulk is minimized by the use of methyl substituents (Me = Methyl).[5a,b] Aurophilic Au--Au interactions are hypothesized to lead to the formation of extended chains of trimers. Moreover, this pioneering research[5-8] demonstrated that the colorless solid of the hexagonal polymorph of [Au_3(MeN=COMe)$_3$][5], displays the rather interesting "solvoluminescence" phenomenon: upon prior irradiation of a crystalline sample with near-UV light, a bright burst of yellow light is observed spontaneously (remaining after irradiation stops) when solvent is introduced. The intensity of the luminescence is greatest for the best solvents for $[Au_3(MeN{=}COMe)_3]$, e.g., chloroform and methylene chloride.[5a] In the solid state, $[Au_3(MeN{=}COMe)_3]$ displays multiple crystalline polymorphs: hexagonal (P6/m) (which has eclipsed **(I)** and staggered (**II**) stacks), triclinic (P-1) (**III**) and monoclinic (C2/c) (Figure 5.2)[5b]. Other polymorphic forms of gold carbeniate complexes, $[Au_3(^{n}PeN{=}COMe)_3]$ (**IV**) and $[Au_3(^{i}PrN{=}COMe)_3]$ with n-pentyl (^{n}Pe) and isopropyl (^{i}Pr) substituents were reported. These polymorphs differ in the way in which the trimer moieties interact with one another (Figure 5.2).

In the hexagonal form of $[Au_3(MeN{=}COMe)_3]$, which has a broad emission and a long wavelength excitation, and is the only form to display solvoluminescence, the trimers form two stack types, **I** and **II,** Figure 5.2[5a]. The hexagonal polymorph **I** shows an eclipsed stacking pattern with close Au--Au interactions forming a columnar extended chain, $d_{Au\text{-}Au}$ = 3.346 Å (intermolecular) between pairs of trimers, and $d_{Au\text{-}Au}$ = 3.308 Å (intramolecular) within the trimer. Polymorph **II** displays a staggered stacking pattern resulting in dimers of trimers, where molecules are disordered with two positions of the trimers offset by 60° with $d_{Au\text{-}Au}$ = 3.384 Å (intermolecular) and $d_{Au\text{-}Au}$ = 3.280 Å (intramolecular). The triclinic polymorph **III** involves formation of dimers of trimers in a "chair" conformation with $d_{Au\text{-}Au}$ = 3.339 Å (intramolecular) and $d_{Au\text{-}Au}$ = 3.528 Å (intermolecular).[7] The monoclinic polymorph (**IV**) contains short prismatic stacks that consist of three trimers with $d_{Au\text{-}Au}$ = 3.323 Å (intramolecular) and a single aurophilic connection between stacks of trimers, $d_{Au\text{-}Au}$ = 3.653 Å (intermolecular)[5b].

The present chapter entails a combined experimental and computational investigation of how solid state stacking in [Au$_3$(RN=COR')$_3$] complexes effect their structural, photophysical and conduction properties.

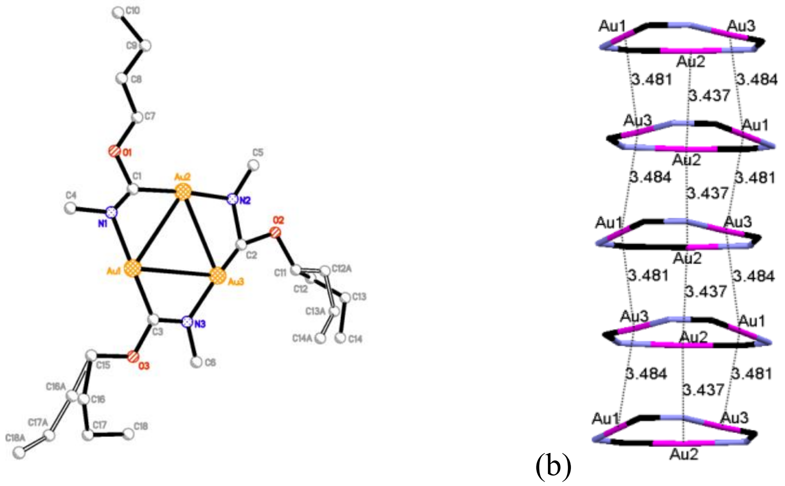

Figure 5.3. a) Crystal structure of [Au$_3$(MeN=CO^{n}Bu)$_3$], b) Molecule stacking orientation. (Pink = Au, blue = N, black = C). Experimental data were acquired by Roy McDougald.

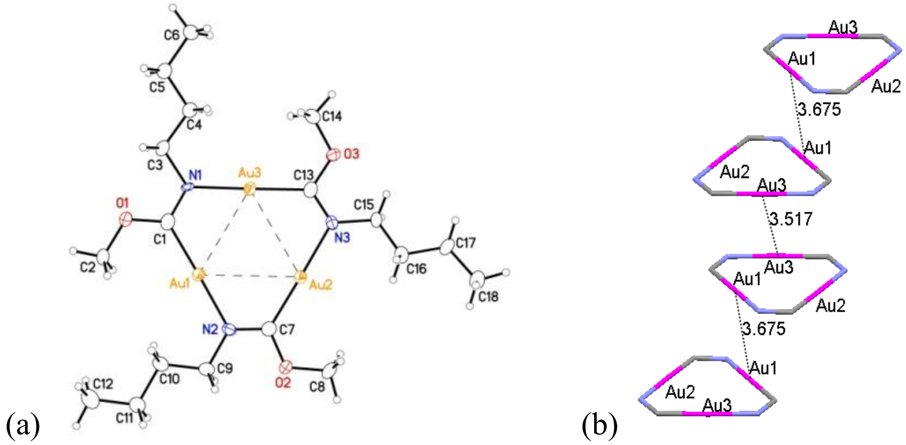

Figure 5.4. a) Crystal structure of [Au$_3$(^{n}BuN=COMe)$_3$], b) Molecule stacking orientation. (Pink = Au, blue = N, black = C). Experimental data were acquired by Roy McDougald.

5.2 Experimental Section

Experimental studies of structural and photophysical properties were performed by Mr. Roy McDougald (UNT) on the following 5 complexes: [Au$_3$(MeN=CO^{n}Bu)$_3$], [Au$_3$(^{n}BuN=COMe)$_3$], [Au$_3$(^{n}BuN=CO^{n}Bu)$_3$], [Au$_3$(^{c}PeN=COMe)$_3$] and the

[Au$_3$(MeN=COMe)$_3$] hexagonal polymorph, ^{n}Bu = normal butyl and ^{c}Pe = cyclopentyl (Figures 5.3 to 5.6). The ^{n}Bu and ^{c}Pe ligands were used in order to increase the solubility of the trinuclear gold(I) carbeniate complexes , which could expand their uses in electronic devices. Additionally, the luminescence properties for each of the complexes vary due to the nature of the aurophilic intermolecular interactions of each compound, which are augmented by the substituents. In this section, the synthetic and X-ray structural data from our experimental collaborators are ignored but the experimental luminescence and conductivity data available for some of the aforementioned complexes are presented to provide a context between experiments and our computational modeling. To explain the relation between molecular/solid-state structure and the luminescence, selected geometric data of gold (I) carbeniate complexes is provided in Table 5.1.

Table 5.1. Selected interatomic distances (Å) and angles (deg) for trinuclear gold (I) complexes. Experimental data were acquired by Roy McDougald.

	Au$_3$(MeN=CO^{n}Bu)$_3$	**Au$_3$(^{n}BuN=COMe)$_3$**	**Au$_3$(^{n}BuN=CO^{n}Bu)$_3$**	**Au$_3$(^{c}PeN=COMe)$_3$**
Au-C	1.97(4) 1.91(3) 1.46(7)	1.991(8) 1.984(8) 1.989(8)	1.925(9) 1.93(2) 1.93(2)	2.001(12) 1.987(12) 1.971(12)
Au-N	2.09(3) 1.99(5) 2.01(3)	2.053(6) 2.059(6) 2.029(6)	2.034(15) 2.014(17) 2.068(16)	2.069(9) 2.062(10) 2.046(9)
C=N	1.15(3) 1.68(12) 1.31(4)	1.312(10) 1.300(10) 1.291(10)	1.337(9) 1.332(9) 1.30(2)	1.280(14) 1.257(15) 1.289(15)
Au-Au (intra)	3.290(2) 3.295(3) 3.281(3)	3.2656(4) 3.3218(5) 3.3328(5)	3.2899(16) 3.3039(15) 3.2920(17)	3.2691(7) 3.3210(7) 3.2904(7)
C-Au-N	179.2(16) 174.9(14) 176(4)	178.5(3) 178.7(3) 177.6(3)	177.2(7) 178.7(7) 176.1(8)	177.0(4) 177.9(5) 175.4(4)

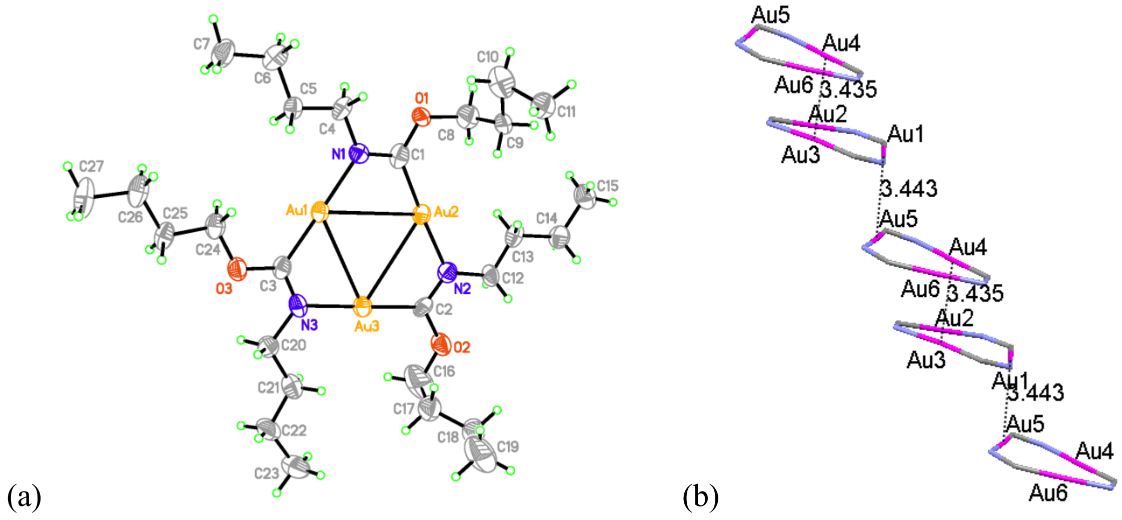

Figure 5.5. a) Crystal structure of [$Au_3(^nBuN{=}CO^nBu)_3$], b) Molecule stacking orientation. (Pink = Au, blue = N, black = C). Experimental data were acquired by Roy McDougald.

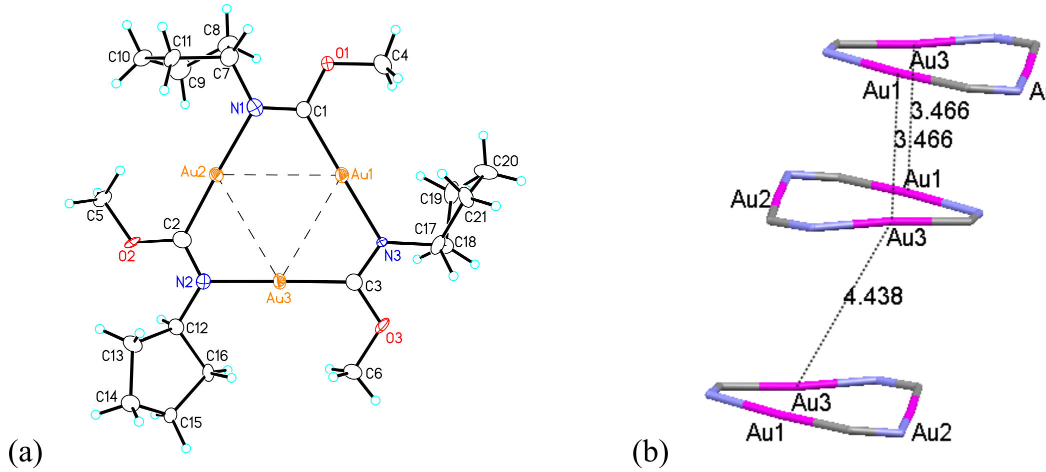

Figure 5.6. a) Crystal structure of [$Au_3(^cPeN{=}COMe)_3$], b) Molecule stacking orientation. (Pink = Au, blue = N, black = C). Experimental data were acquired by Roy McDougald.

5.2.1 Electronic Spectroscopy of Gold Carbeniate Complexes

The complex [$Au(MeN{=}COMe)]_3$ (Figure 5.1, where R=R’=Me), originally prepared by Balch and coworkers[5a], shows a broad emission in the solid state across the visible spectrum ranging from 400 - 700 nm and an excitation band that extends to 425 nm. The data collected in the Omary laboratory and displayed in Figure 5.7 are consistent with those originally reported for this complex[5a]. The broadness of the emission band causes the complex to render white light when irritated with a high energy excitation. This broad emission is proposed to be due to two factors, the first is the small contraction of the intermolecular Au--Au distances upon excitation (vide infra), denoted by the relatively small Stokes' shift between the excitation and emission bands for the blue band. Secondly, the red band with a huge Stokes' shift is attributed to self-trapped excitons[7] that form within disordered stacks and give rise to molecule-like emission (likely from dimer-of-trimer units).

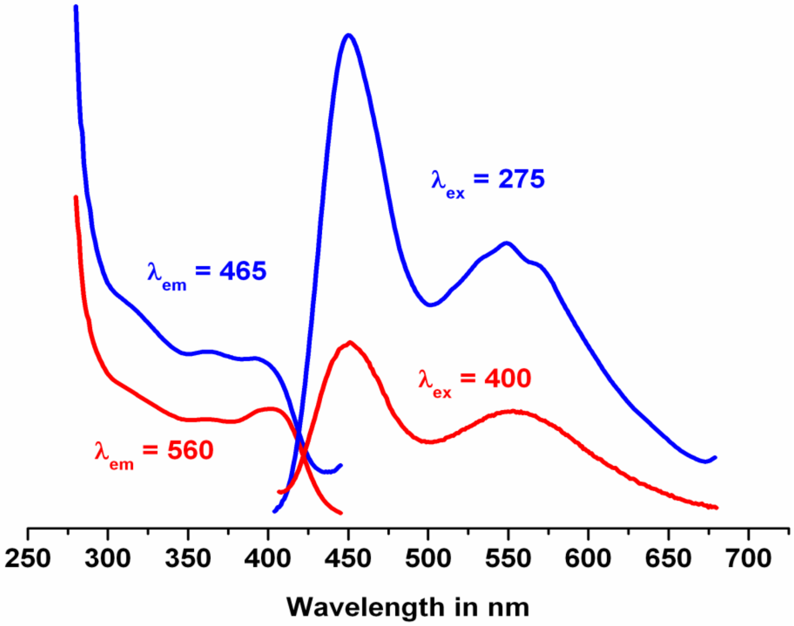

Figure 5.7. Solid state photoluminescence spectra for the hexagonal polymorph of [$Au_3(MeN{=}COMe)_3$] at 298 K. The white emission is due to a combination of a blue band from delocalized excitons (band gap emission), and an orange band due to low-energy self-trapped excitons (discrete molecular orbital emission). Experimental data were acquired by Roy McDougald.

Many Au^I complexes exhibit visible luminescence with high phosphorescence quantum yield at room temperature. The large Stokes' shift for Au^I complexes exhibiting metal-centered emission due to aurophilic association suggests that the Au--Au distances between gold trimer molecules contract greatly upon excitation[3,5]. There is a smaller (3494 cm^{-1}) Stokes' shift in the hexagonal [$Au(MeOC{=}NMe)]_3$ complex, which implies a smaller contraction upon excitation. This is supported by the fact that the intermolecular Au--Au distances are already short (3.346 Å) in the ground state and they occur upon extended chains, making their further compression harder upon photoexcitation or oxidation in luminescence experiments (Figure 5.7).

As previously shown, the structure of the $[Au_3(MeN{=}CO^nBu)_3]$ complex is similar to that of the hexagonal polymorph of the $[Au_3(MeN{=}COMe)_3]$ complex[5a], in fact that the molecules form supramolecular infinite chain structures. Figure 5.8 shows that the $[Au_3(MeN{=}CO^nBu)_3]$ compound has a low energy excitation extending to the visible region (420 nm) and a high energy blue emission with no additional emission band in the red region. The near-visible excitation is due to strong aurophilic interactions found in the packed extended chains. The blue emission of this compound occurs from delocalized excitons (direct band-gap emission) and the Stokes' shift will consequently be small because the trimer chains are already strongly bound in the ground state.

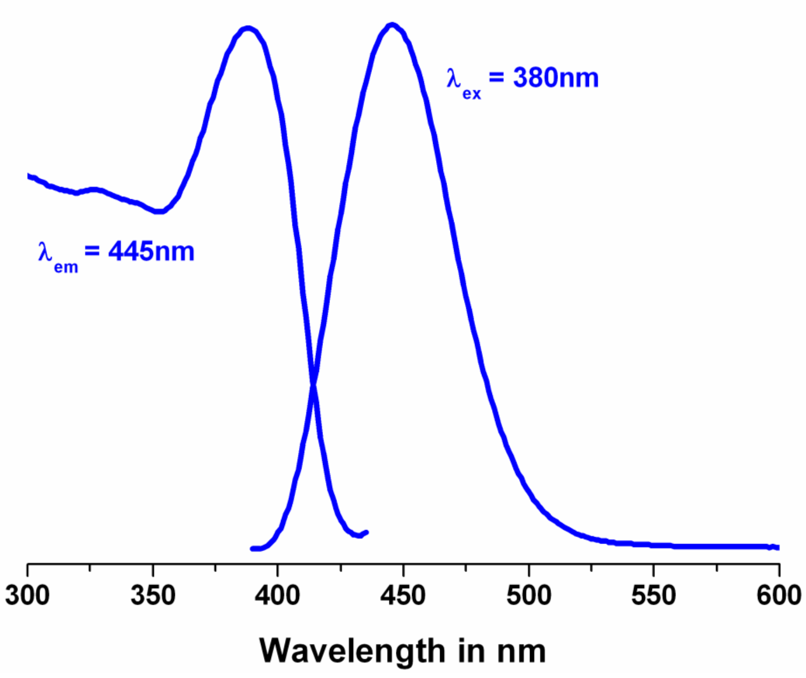

Figure 5.8. Solid state photoluminescence spectra at 298 K of $[Au_3(MeN{=}CO^nBu)_3]$. Experimental data were acquired by Roy McDougald.

The solid state photoluminescence for the [$Au_3(^nBuN{=}COMe)_3$] is given in Figure 5.9 and shows a high energy excitation extending to the visible region (310 nm) and a low energy red emission with no emission in the blue region. The large Stokes' shift (17,681cm^{-1}) given here is due to the contraction of the long intermolecular Au--Au distance in the dimer of trimers for this complex. In moving from the ground state to the excited state, a large aurophilic contraction or excited state distortion occurs in the dimer of trimers and is indicated by the aforementioned humongous Stokes's shift. The low energy red emission is due to the formation of an intermolecular excimer in the dimer of trimer molecular unit and the high energy excitation is due to an electronic transition between discrete molecular orbitals of the dimer of trimer molecules.

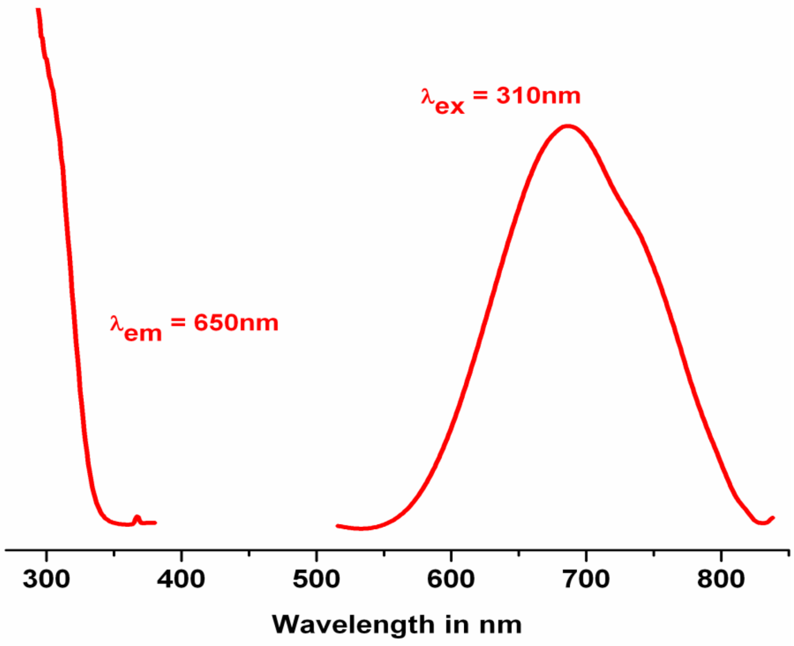

Figure 5.9. Solid state photoluminescence spectra at 298 K of [$Au_3(^nBuN{=}COMe)_3$]. Experimental data were acquired by Roy McDougald.

Figure 5.10 shows that the [$Au_3(^nBuN{=}CO^nBu)_3$] complex has an excitation at 360 nm and a broad emission that crosses the visible spectrum ranging from 400 - 700 nm. This complex was shown to have a loose extended chain structure where the Au--Au distance is shorter than that found in the dimer of trimers and longer than those found in the packed extended chains. Therefore the excitation band is lower in energy than the dimer of trimer structures and higher in energy than that of the strongly-interacting prismatic chains. The emission profile shows two bands, one of which is in the blue region while the other is in the orange region, which is quite similar to the photoluminescence of the hexagonal polymorph of [$Au_3(MeN{=}COMe)_3$]. Given that this situation is intermediate between the molecular and semiconductor band structure, it is reasonable to assign the dual emission that gives rise to a warm white luminescence color in Figure 5.10 as a combination of these two cases. Therefore, the blue band is due to direct band gap emission while the orange band is due to molecula-like self-trapped excitons.

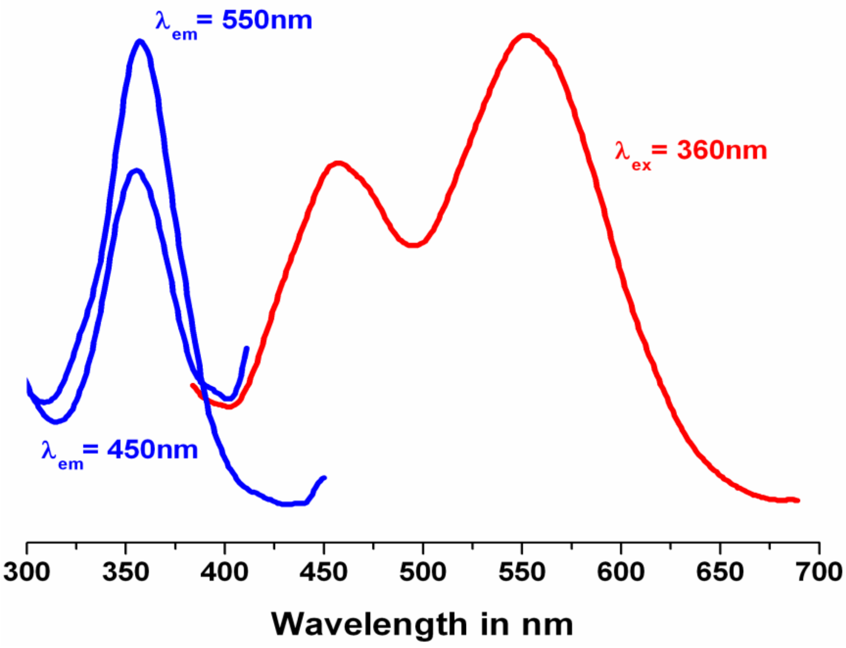

Figure 5.10. Solid state photoluminescence spectra at 298 K of [$Au_3(^nBuN{=}CO^nBu)_3$]. Experimental data were acquired by Roy McDougald.

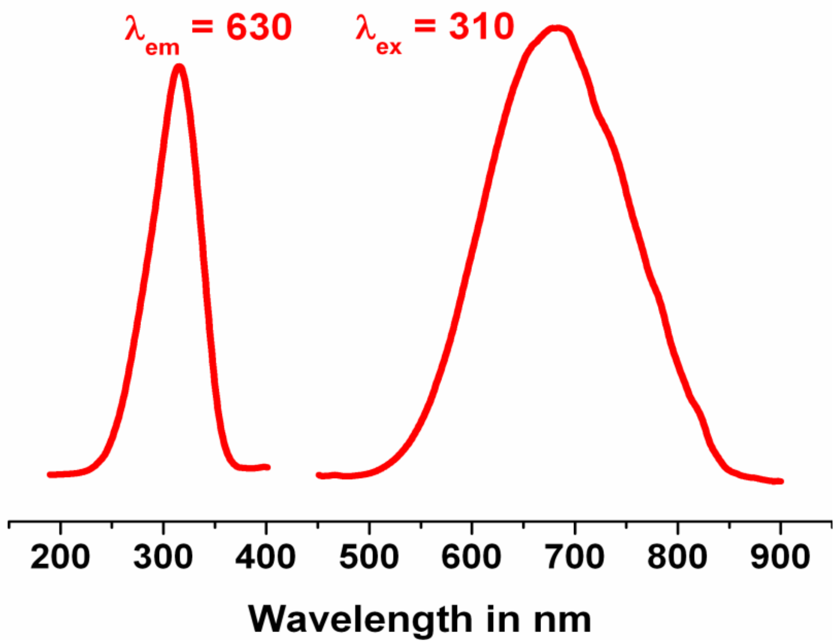

Figure 5.11. Solid state photoluminescence spectra at 298 K of [Au_3(^{c}PeN=COMe)$_3$]. Experimental data were acquired by Roy McDougald.

In Figure 5.11 the luminescence spectra for the [Au_3(^{c}PeN=COMe)$_3$] is given. The complex has a similar crystal structure to that of [Au_3(^{n}BuN=COMe)$_3$] in which molecules conform to a dimer of trimer structure, but with two Au--Au intermolecular interactions between the trimers, as previously shown. A huge Stokes' shift of 16,918 cm^{-1} (Table 5.2) is again seen here for the [Au_3(^{c}PeN=COMe)$_3$]$_3$ solid and is consistent with long intermolecular Au--Au distances in the ground state. Thus, there will be more geometric reorganization in the excited state (calculations suggest a contraction of Au--Au intermolecular distances; vide infra) for these stacked materials, as opposed to the extended chain complexes with smaller Stokes' shifts. As before, the high energy excitation is due to an electronic transition between discrete molecular orbitals of the dimer of trimer molecules and the red low energy emission is due to formation of an intermolecular excimer in the dimer of trimer molecules.

Table 5.2. The excitation and emission maxima (nm), along with the Stokes' shift (cm^{-1}) for the trinuclear gold(I) complexes described here. Experimental data were acquired by Roy McDougald.

Complex	λ Ex. Max	λ Em. Max	Stokes' Shift
$Au_3(MeN{=}COMe)_3$	400	450	2,778
$Au_3(MeN{=}CO^nBu)_3$	388	446	3,352
$Au_3(^nBuN{=}COMe)_3$	310	686	17,681
$Au_3(^nBuN{=}CO^nBu)_3$	357	457	6,130
$Au_3(^cPeN{=}COMe)_3$	316	679	16,918

5.2.2 Structural Disparity in Extended Stacking of Au(I) Carbeniate Complexes

Among a variety of $[Au_3(RN{=}COR')_3]$ polymorphic structures synthesized by Balch's group and at UNT, we found that only two infinitely extended chain structures, $Au_3(MeN{=}COMe)_3$ and $Au_3(MeN{=}CO^nBu)_3$ have smaller Stokes' shifts, and shorter Au--Au bond distances, indicating that these materials may have suitable photophysical and conduction properties for molecular electronic devices. An interesting solid state structural difference between Balch's[5a], **I** (Figure 5.2) and our (Figure 5.3) extended stacks arises from the asymmetric, μ-N,C nature of the bidentate carbeniate ligand. Even for identical substituents (i.e., R = R'), and in an eclipsed conformation, one may alternatively arrange the ligands head-to-head (H-H), i.e., with the ligating N atoms lined up along the columnar, trigonal prismatic stack, or head-to-tail (H-T), i.e., with ligating C and N atoms alternating along the columnar stacks (Figure 5.12).

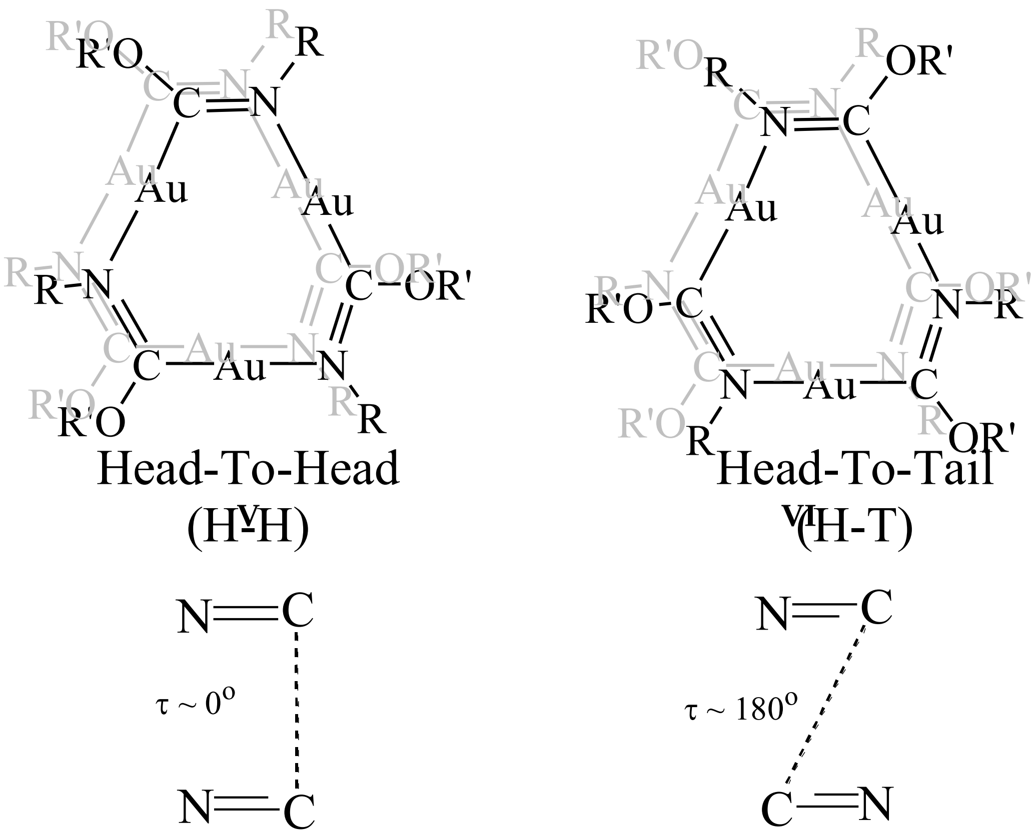

Figure 5.12. Pictorial description of the head-to-head (H-H) **V**, and head-to-tail (H-T) **VI**, arrangement of columnar stacks.

We hypothesized that the differences in electronegativity between carbon and nitrogen might yield an advantage to the H-T arrangement, i.e., enhanced electrostatic and/or dipole-dipole ($C^{\delta+}=N^{\delta-}/N^{\delta+}=C^{\delta+}$) attraction to augment aurophilic Au--Au interactions. To assess the foregoing hypothesis in the solid-state, we investigated in the Cambridge Structural Database (CSD)[9] the structure of C=N···C=N close contacts from 3 – 4 Å (bond centroid to bond centroid distance). To avoid complications due to different sized metals and from ionic systems (e.g., differences in counterion properties), we focused on neutral, organic molecules with C=N moieties in which the C was three-coordinate and the N two-coordinate. To focus attention on the most reliable crystal structures we limited the search to R values < 5% and those without disorder or errors, and excluded polymeric materials. For these two interacting bonds, we tabulated the centroid-to-centroid separation and the N=C···C=N dihedral (τ). For the latter metric, we defined H-H as $\tau \sim 0 \pm 10°$ and H-T as $\tau \sim 160 - 180°$. Two observations from this database analysis support the greater favorability of H-H versus H-T interactions among N=C functionalities. First, for the same 20° range of N=C···C=N dihedrals, there are more than double the number of observations within the 3 – 4 Å range defined as a close contact for the H-H versus the H-T orientation. Second, for those interactions the average (and median) distance is 3.8 Å for H-H (1662 observations) and 3.7 Å for H-T (3754 observations). The results of this solid-state structure analysis thus support the contention that electrostatic/dipole interactions in carbeniate and related asymmetric N,C-ligating ligands may provide an additional feature to be exploited to crystal engineer such materials. We will return to this point again below as we investigate the extent to which shorter trimer-trimer separations impact calculated HOMO-LUMO/VB-CB gaps (and thus electronic and optical properties) for Au_3Cb_3 materials (HOMO = highest occupied Kohn-Sham molecular orbital; LUMO = lowest unoccupied molecular orbital; VB = valence band; CB = conduction band).

5.3 Computational Modeling Section

Due to a variety of photophysical properties of $[Au_3(RN{=}COR')_3]$ complexes bearing numerous polymorphic structures (Figure 5.2), reported from present and earlier[5-8] experiments, we report here a comprehensive computational study of different structural forms of Au_3Cb_3 complexes under both molecular and periodic regimes. In this research, we analyze the relationships between solid state and molecular electronic structures and optoelectronic properties of these materials utilizing their different polymorphic forms (Figure 5.2) as guidance. Simulations of the ground (singlet) and lowest excited (triplet) states are analyzed for molecular models to augment the search for important structure (molecular or solid)-property (electronic or optical) relationships that may guide the rational synthesis of novel materials for molecular electronic devices with both desired intramolecular and intermolecular arrangements.

5.3.1 Solid State Modeling Methodology

Solid state, calculations are also carried out using the VASP (Vienna Ab initio Simulation Program) code[10,11]. Density functional theory within the PAW (Projector-Augmented Wave) method[12]; the generalized gradient approximation (GGA) functional of Perdew, Burke and Ernzerhof (PBE)[13] was employed. The electronic wave functions are sampled on a 1×1×3 k-mesh; in the irreducible Brillouin zone (BZ) using the Monkhorst and Pack method[14]. The cut-off energy of the wave functions was 400 eV. Convergence of the total energy with the k-mesh in the Brillouin zones and the plane wave cut-off energy was checked. Gaussian smearing was used to set the partial occupancies for each wave function with a smearing width of 0.05 eV.

5.3.2 Molecular Modeling Methodology

The Gaussian 09 package is used to perform density functional calculations on molecular entities[15]. Los Alamos valence basis sets, LANL2DZ(2f,p)* [16-17] (with augmented d-polarization functions taken from 6-31G* basis set on main group elements) are employed in conjunction with the M06 functional[18] for all optimization and single point calculations. The LANL2DZ(2f,p)* basis set[16-17] was chosen as per an earlier study by Barakat et al. involving Au complexes, where an extended basis set was used, particularly on the gold atoms augmented by two f functions[19] and one Couty-Hall outer p function[20]. Calculations with the M06 functionals gave results more consistent with available experimental data, and even outperformed B3LYP functional[21] and higher-order, wavefunction-based MP2[22] calculations. Indeed, the latter, if anything, yields an overly bound Au_3Cb_3 dimer-of-trimer (inter-trimer separations ~ 2.8 Å). Hence, we focused our attention on the newer, hybrid meta-GGA functional of Truhlar and coworkers[18]. All geometries are optimized with restricted Kohn–Sham methods for singlet spin states and unrestricted Kohn-Sham methods for triplet multiplicities.

5.3.3 Periodic Modeling of Gold Carbeniate Complexes

Preliminary EHTB calculations (not presented in this dissertation) revealed interesting variations in the total and partial density of states for the trimeric gold carbeniates from the Balch and Omary labs, both in the conduction and valence bands. Given these electronic structure differences in the R and R' substituents studied by Balch[5] and those in our lab, the differences in crystal symmetry/morphology, and the presence of disorder in the experimentally characterized complexes, we sought to use first-principles computations to dissect the different experimentally observed solid-state structural variations in order to quantify their impact upon the condensed phase electronic structure of Au_3Cb_3 complexes.

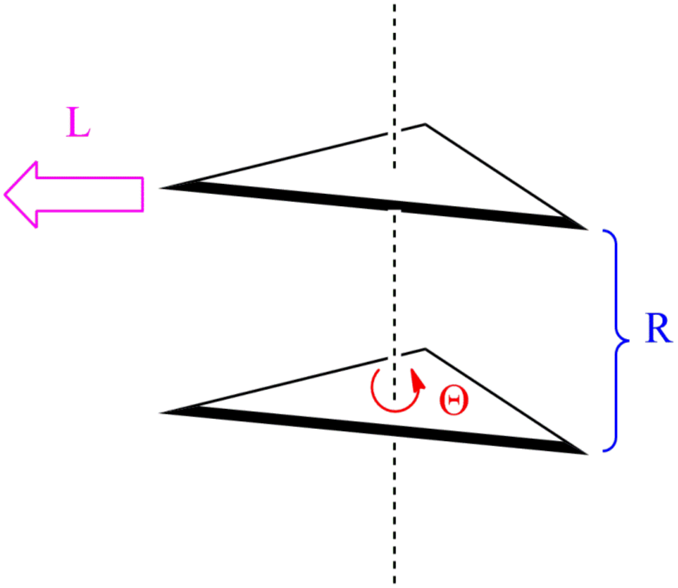

Figure 5.13. Different structural variations that impact trimer-trimer interactions in the solid state. The two triangles represent 2 stacked Au_3Cb_3 trimers. R, Θ, L indicate the inter-trimer separation, rotation and lateral movement, respectively.

The structural variations that impact trimer-trimer interactions in the solid state can be divided into three categories: (i) trimer-trimer stacking distance (R), (ii) rotational motion of one trimer relative to the other about the three-fold axis, (Θ); and (iii) lateral motion of one trimer relative to the other (L), Figure 5.13. Similar structural modifications were investigated in an earlier contribution from our groups utilizing molecular cyclo-trimer models and molecular (i.e., Gaussian-based) DFT calculations. One pertinent conclusion from that previous contribution was that such molecular motions were “soft”[23]. Hence, one may propose from such precedents, and from the structural diversity discussed above, that there is substantial potential to crystal engineer gold carbeniate complexes utilizing aurophilic interactions, hydrogen bonding, and electrostatic interactions. As such, one might expect that it is possible to rationally engineer materials with not only desirable chemical properties, but more importantly with desirable condensed phase and device-level properties. Given these goals, it was deemed prudent to use the same substituents to minimize differences due to the donor/acceptor properties of R and R’. Furthermore, to minimize computational expense, we chose R = R’ = H. Finally, the structural transformations in Figure 5.13 are evaluated with plane-wave DFT methods.

Table 5.3. Unit cell parameters of computationally generated crystal structures to study structural variations R, Θ, L. In this table; a, b, c and α, β, γ represent unit cell axes and angles respectively.

S. No.	Structural Variation	a (Å)	b (Å)	c (Å)	α (°)	β (°)	γ (°)	Θ (°)
1	Inter-trimer Distance (R)							
	Case-A	19.41	19.41	c-axis varied to maintain $R_1=R_2$ 4.69 to 10.69	90	90	120	0
	Case-B	19.41	19.41	C-axis varied to maintain $R_1 \neq R_2$ 5.35 to 9.35	90	90	120	0
2	Rotational Motion (Θ)	19.41	19.41	6.70	90	90	120	0 to 60
3	Lateral Motion (L)	25.41	25.41	6.70	90	90	120	0

In order to study the effect of the three structural changes (R, Θ, L) depicted in Figure 5.13 with PW-DFT calculations, crystal structures (Table 5.3) were built to model each structural change. In the following sections we will discuss the details of how the crystal structures are built for each structural change and how they impact the band gap.

Inter-trimer separation (R): Balch's perfectly stacked structure (**I**)[5a] was taken as a template[5b, 24] to probe the effect of 'R' (Figure 5.13) modification along the c-axis of the unit cell. This assumption holds valid considering the crystal packing, Van der Waals radii and interactions of cyclo-trimers. A crystal structure (Table 5.3) with four gold carbeniate trimers in the unit cell (Figure 5.14) with two pairs each stacking as an eclipsed structure (**I**) inside the unit cell was built as the reference. With this reference structure, the effect of 'R' (inter-trimer separation) was studied in two cases:

case-A) constant increasing or decreasing 'R' of the eclipsed stack (**I**) within the unit cell and its image (i.e. $R_1 = R_2$ in Figure 5.14),

case-B) fixing R_1 of the eclipsed stack (**I**) to the experimental Au—Au bond length, 3.346 Å[5a] within the unit cell, but changing R_2, and hence the distance of a cyclo-trimer with its image cell (i.e., $R_1 \neq R_2$ in Figure 5.14) along the c-axis of the crystal. This change can be made by modifying the unit cell c-axis length while keeping R_1 constant. Case A represents an infinite stack with constant inter-trimer distances and Case B models asymmetric stacking with irregular inter-trimer distances. PW-DFT calculations are performed on both case A and B to study the effect of R on their band structure.

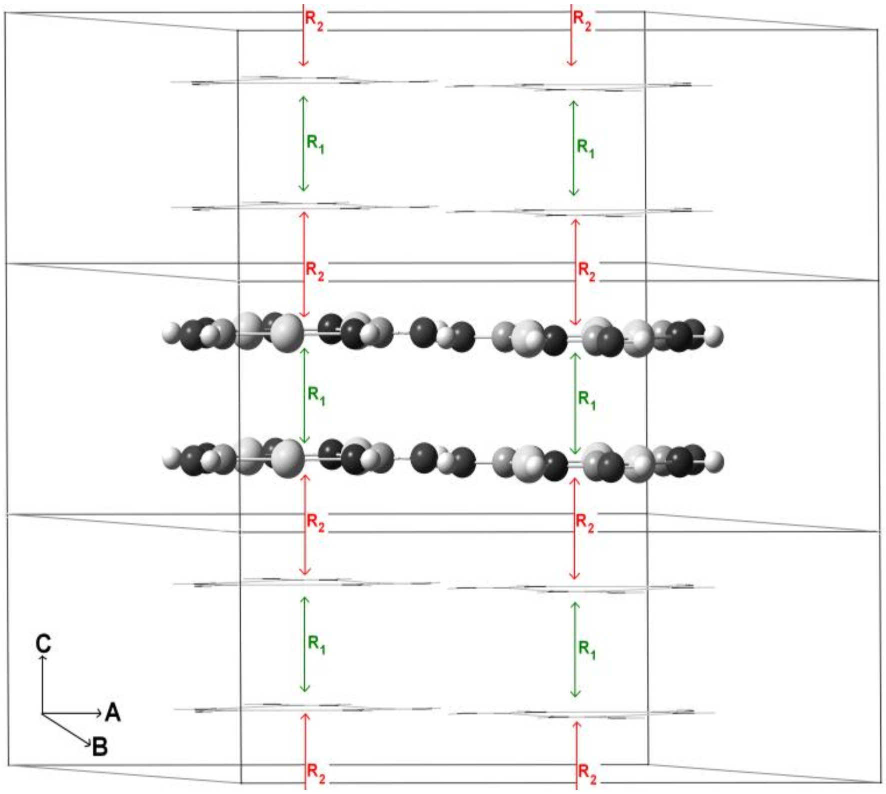

Figure 5.14. Unit cell with 2 images (above and below) along the c-axis from computationally generated crystal structure of cyclo-[$Au_3(HN{=}COH)_3$] complex. R_1, R_2 represent inter trimer distances within the unit cell and with the image cell respectively.

In case A ($R_1 = R_2$), the band gap (BG) is calculated for structures with 'R' in the range of 2.346 – 5.346 Å. From Figure 5.15, it can be seen that the band gap increases with increase in the inter trimer distances. At the experimental inter trimer distance[5a] of 3.346 Å, the calculated BG = 2.65 eV. The drastic drop in BG at $R_1 = R_2 = 2.346$ Å and 3.000 Å is caused by band broadening due to very short inter-trimer distances. This can also be seen from the relative energies (Figure 5.15) of all complexes considered in case A. Note that the rapid increase in energy (> 2 eV) at R_1, $R_2 < 3$ Å (data points of relative energies for $R_1 = R_2 < 3$ Å are not shown in Figure 5.15) is consistent with experimentally observed inter-trimer separations in aurophilic cyclo-[Au(μ-L)]$_3$ complexes[9] (L = monoanionic bidentate ligands of C-C, C-N, N-N ligation) in the solid state.

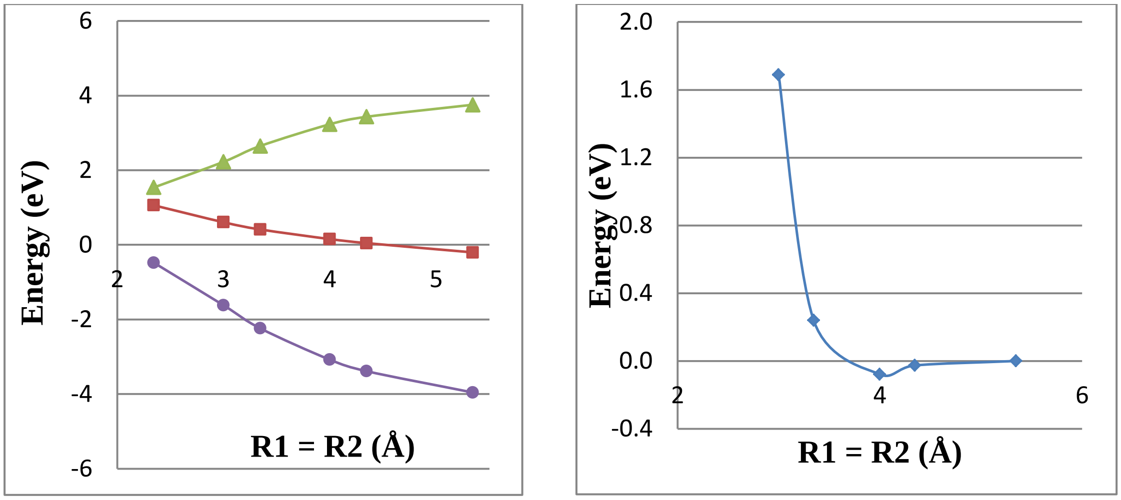

Figure 5.15. Band structures (left) and relative energies (right) of computationally generated cyclo-[$Au_3(HN=COH)_3$] complexes with different variations of 'R' mentioned for case A. Colors: Band gap (green), conduction band (red), valence band (purple) and relative energy (blue).

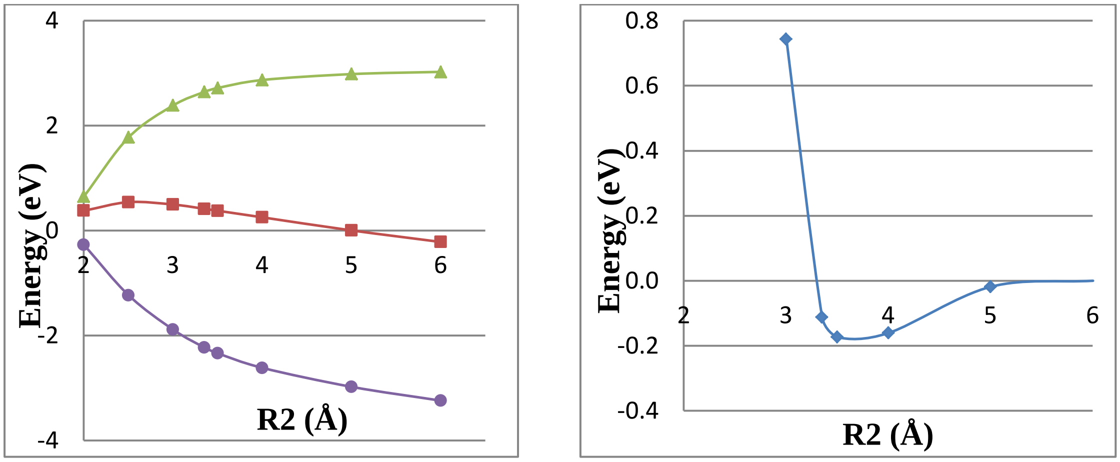

Figure 5.16. Band structures (left) and relative energies (right) of computationally generated cyclo-[$Au_3(HN=COH)_3$] complexes with different variartions of "R" mentioned for case B. Colors: Band gap (green), conduction band (red), valence band (purple) and relative energy (blue).

In case B ($R_1 \neq R_2$), the band gap (BG) is calculated for structures with R_2 in the range of 2.004 – 6.004 Å. From Figure 5.16, it can be seen that band gap increases with increase in R_2. Again, the drastic drop in BG at R_2 = 2.004, 2.504, and 3.004 Å is caused by band broadening due to very short inter-trimer distances between the unit cell with neighboring image cells

(Figure 5.14), which is also reflected in the relative energies (Figure 5.16, data points of relative energies (> 2 eV) for $R_2 < 3$ Å are not shown) of all models considered in case B.

Overall, the simulations (both cases A and B) clearly indicate that shorter inter-trimer distances (R_1) with symmetric stacking ($R_1 = R_2$) yield smaller band gaps, suggesting the importance of this structural parameter in making good condensed phase conductors.

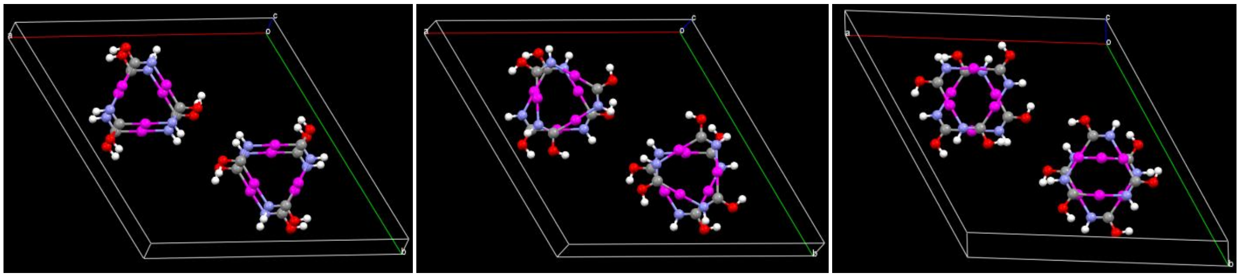

Figure 5.17. Computationally generated crystal structure with 4 [$Au_3(HN{=}COH)_3$] molecules inside the unit cell representing the variation of rotational motion (Θ). From left to right, Θ = 0°, 30°, 60°.

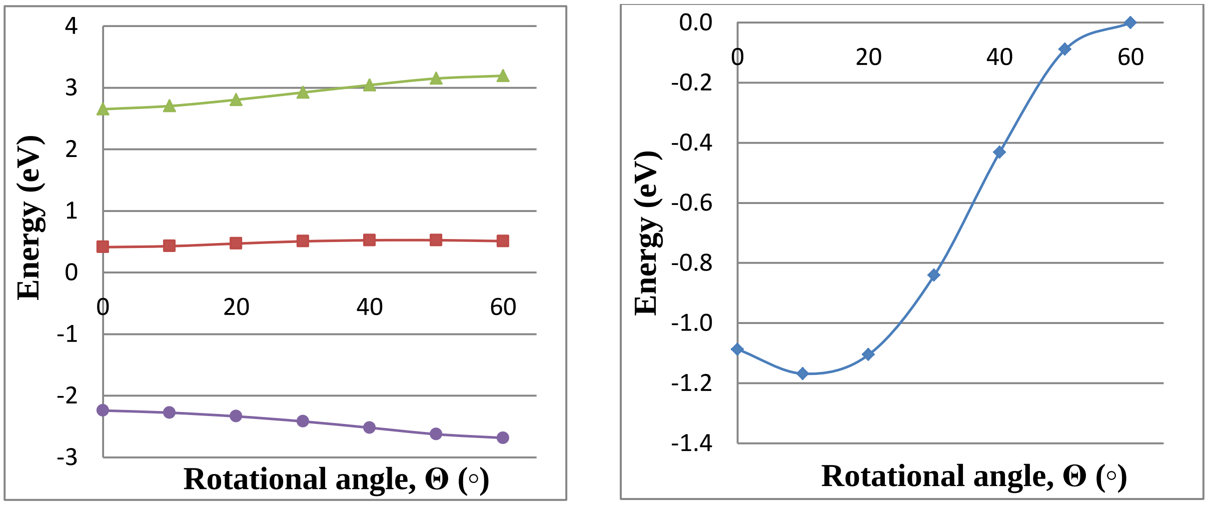

Figure 5.18. Band structures (left) and relative energies (right) of computationally generated cyclo-[$Au_3(HN{=}COH)_3$] complexes with different variations of Θ. Colors: Band gap (green), conduction band (red), valence band (purple) and relative energy (blue).

Rotational motion (Θ): Balch's disordered stack (**II**)[5a] is taken as a template[5b,25] to study the effect of 'Θ' (Figure 5.13) along the c-axis of the unit cell. A reference crystal structure (Table 5.3, Figure 5.17) was built with four gold carbeniate trimers in the unit cell (Figure 5.14) with two each stacking as a staggered structure (**II**) with rotational angle of 60^o inside the unit cell. With this reference structure, the effect of 'Θ' is studied by rotating the trimers from Θ = 60^o to 0^o in 10° increments. For all calculations with different Θ values, the unit cell parameters and inter-trimer centroid distance (3.346 Å)[5a] are kept fixed.

Band gaps (BGs) from the PW-DFT calculations with Θ = 0^o to 60^o are plotted in Figure 5.18. The smallest (2.65 eV) and largest (3.19 eV) BG is observed for Θ = 0^o and 60^o, respectively. Comparing the BG energies, it is obvious that the BG change with Θ is much less than calculated for R changes. However, the relative energy (Figure 5.18) for the complex with Θ = 0^o is 1.1 eV less than for the complex with Θ = 60^o. This indicates that the eclipsed stacks (**I**) are energetically more favorable than staggered stacks (**II**) by approximately 1 eV, and that this structural transformation serves to reduce the band gap.

Lateral motion (L): Balch's chair structures (**III**)[5b] are used as templates to study the effect of 'L' (Figure 5.13). Like in the previous two changes (R, Θ), a crystal structure (Table 5.3, Figures 5.19 - 5.20) with four gold carbeniate trimers in the unit cell (Figure 5.19) with two each stacking as the chair structure (**III**) with two short Au--Au distances (3.35 Å)[5b] per stack inside the unit cell is built.

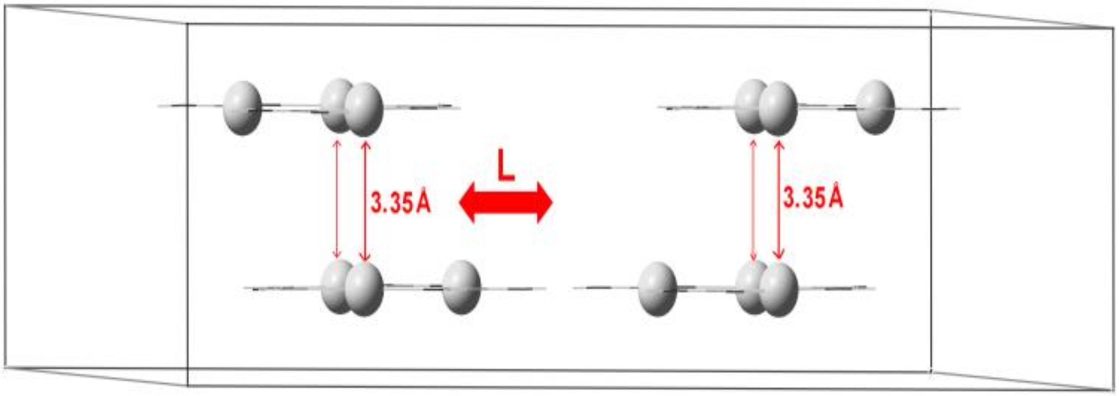

Figure 5.19. Unit cell from computationally generated crystal structure of Au_3Cb_3 complex to study the variation of lateral movement (L).

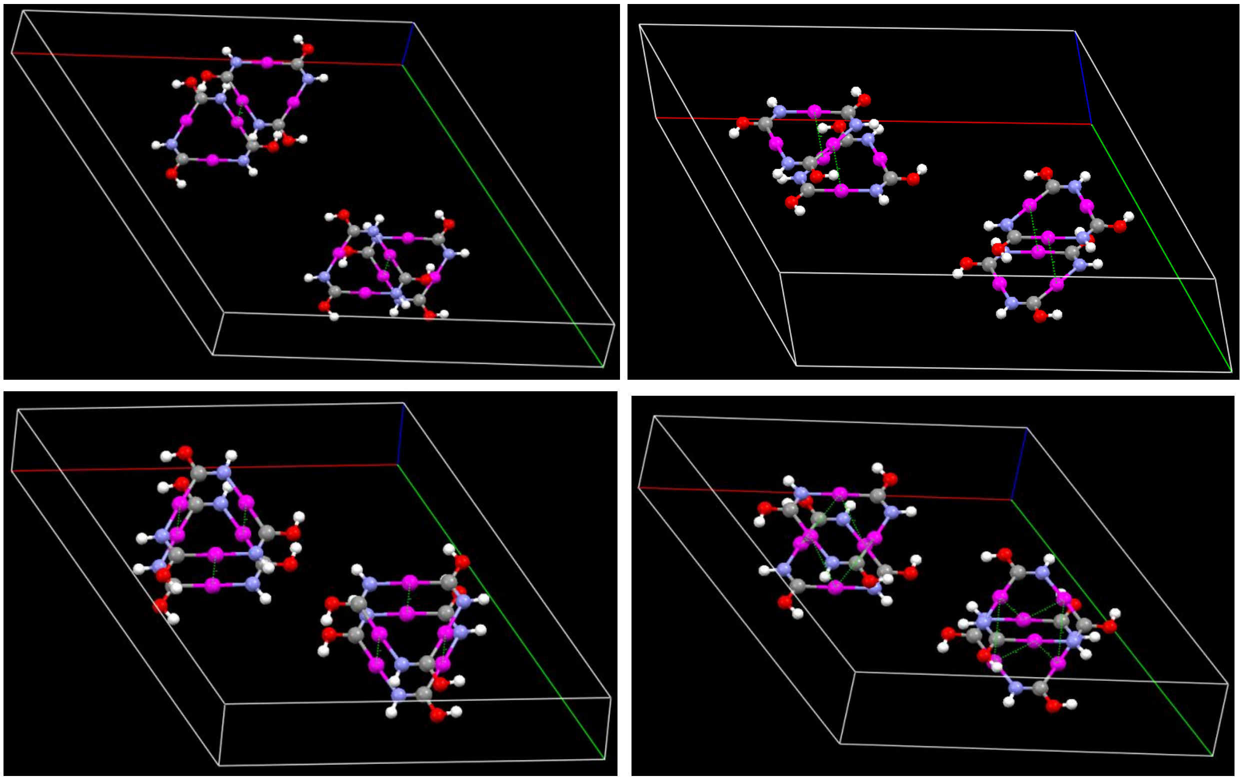

Figure 5.20. Computationally generated crystal structure with 4 [$Au_3(HN{=}COH)_3$] molecules inside the unit cell representing the variation of lateral motion (L). From left to right, number of inter-trimer Au--Au interaction are 1,2,3,6 respectively.

The band gap for the chair structure (**III**) with two short Au--Au bonds is found to be 3.01 eV vs. 2.65 eV (Figure 5.21) for the eclipsed stack (**I**) with three short Au--Au distances. With the chair structure (**III**) as reference, the effect of 'L' (Figure 5.13) along the stack is studied by moving the trimers laterally from 2 short Au--Au bonds in the stack to 6 and 1 Au--Au bonds respectively (Table 5.3, Figure 5.20). As the trimers move laterally, it is important to note that the distance between the planes of the trimers remains fixed at 3.35 Å.[5b] In the case of the complex with 6 Au--Au bonds, the trimers stack in a staggered conformation with Au--Au bond lengths of 3.85(±0.03) Å. In the complex with 1 short Au--Au bond in the stack, the Au--Au bond length of 3.35 Å. Band gaps from PW-DFT calculations of the former and latter geometries are calculated to be 3.284 and 3.280 eV respectively, i.e., a very small BG difference.

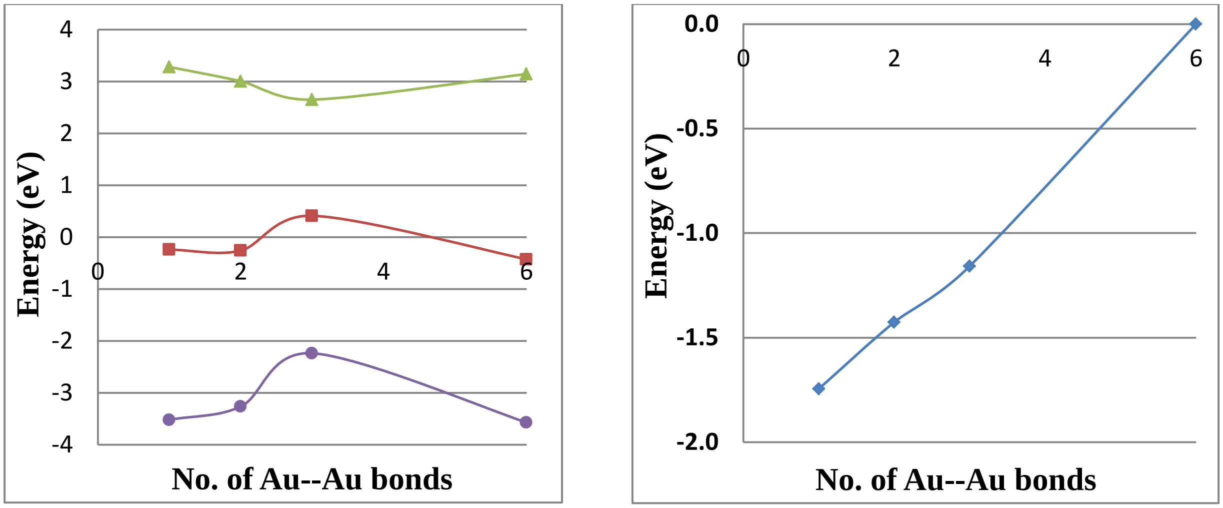

Figure 5.21. Band structures (left) and relative energies (right) of computationally generated cyclo-[$Au_3(HN=COH)_3$] complexes with different variations of L. Colors: Band gap (green), conduction band (red), valence band (purple) and relative energy (blue).

Comparing the band gaps of complexes with 1/2/3/6 short Au--Au bonds (Figure 5.21) with fixed inter planar distances indicate that the complex with 3 Au--Au bonds have smaller band gaps than 1/2/6 Au--Au bonds (Figure 5.21). However, the relative energies are found to increase with the increase in the number of Au--Au bonds (Figure 5.21) as the two trimers move laterally. Again, the PW-DFT simulations indicates that eclipsed stacking of trimers is necessary to obtain smaller band gaps in cyclo-[$Au_3(RN=COR')_3$] complexes, and that such changes are intimately related to the solid state morphology.

5.3.4 Molecular Modeling of Gold Carbeniate Complexes

We studied several molecular models of gold carbeniate complexes to evaluate their electronic and excited state properties. As mentioned earlier, due to the polymorphic nature of cyclo-[$Au_3(RN=COR')_3$] complexes (Figures 5.1, 5.2) which likely arise from varying crystal growth conditions and substituents (R, R'), we confined most of molecular modeling to complexes with R = R' = H. However, some calculations on complexes with R = Me (methyl)

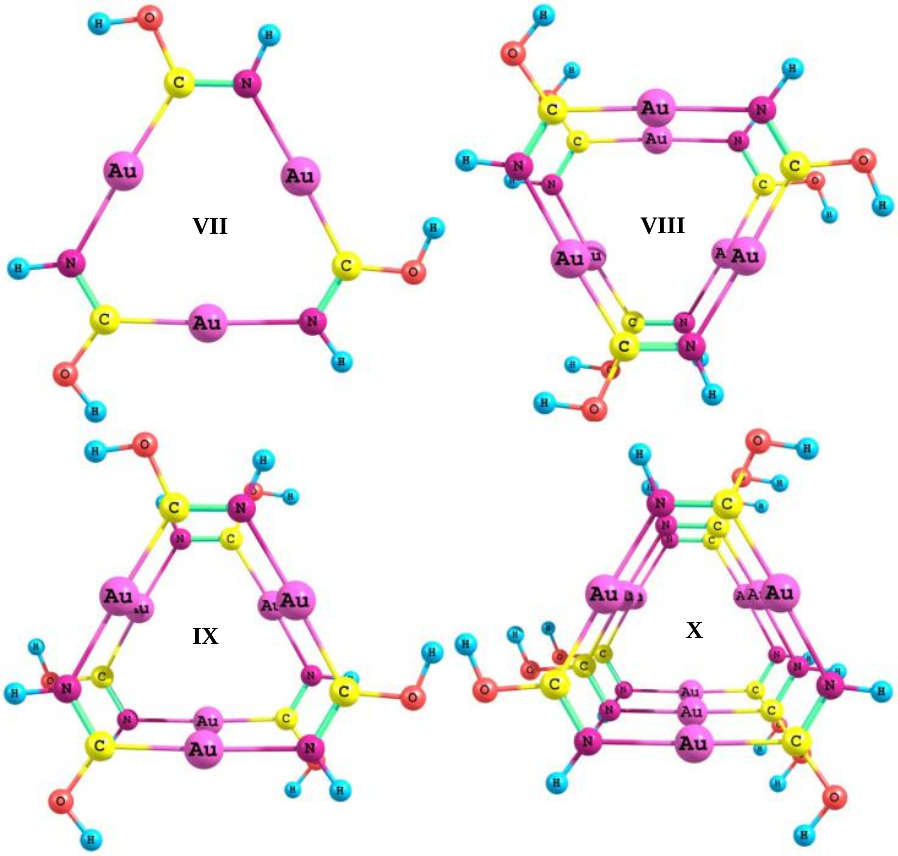

Figure 5.22. Cyclo-[$Au_3(HN{=}COH)_3$] complexes with different stacking patterns used for molecular modeling. MOT (**VII**), DOT:H-H (**VIII**), DOT:H-T (**IX**), TOT:H-H (**X**)

and R' = Me/^{n}Bu (n-butyl) are also performed for comparison, but not detailed in this report, as the conclusions obtained echo those given below for the minimalist molecular models. Molecular calculations with DFT are performed on cyclo-[$Au_3(HN{=}COH)_3$] trimer (T) complexes for a monomer of trimer (MOT)/(**VII)**, dimer of trimer (DOT)/(**VIII**/**IX)** and a trimer of trimer (TOT)/(**X)**, Figure 5.22, model. The DOT calculations are performed on both H-H (**V**/**VIII**) and H-T (**VI**/**IX**) conformations (Figure 5.12) but the TOT calculation is done only on the H-H conformation to conserve resources for this large model. It is important to note that DOT and TOT calculations are performed on eclipsed stacks only, given the favorability of this arrangement shown in the PW-DFT calculations. Molecular computations on a DOT model for staggered and chair conformations are reported elsewhere[23], and indicated a soft potential surface with minimal changes in electronic properties. Comparison of MOT, DOT and TOT complexes will enlighten how dimerization, trimerization and eventually polymerization of trimers would impact their structural and electronic properties.

Calculations are performed on singlet (S_0) and triplet (T_1) - forms of all 4 models (Figure 5.22) described above. All structures are completely relaxed without symmetry constraint. Nu/T_1 structures are calculated to determine the spectroscopic and electronic parameters, relative to Nu/S_0 ground states.

Geometric Properties: After optimization, all S_0 structures remain more planar than the respective triplets in the molecular plane when they stack in DOT and TOT conformations (Figures 5.23 – 5.25). Geometries for S_0 MOT and DOT agree well with the experimental geometries[5a,b]. In S_0 TOT complexes, we observe a rotational motion (Θ) of one trimer relative to the other about the three-fold axis. Irrespective of the changes in Θ, interestingly, the centroid to centroid distances of adjacent trimers in the stack agree with experimental bond distances[5a,b]. The shortest inter trimer Au--Au distances for all DOT and TOT complexes are listed in Table 5.4. Comparing the inter-trimer Au--Au bonds of S_0/ T_1 complexes, it is apparent that Au--Au bonds in the T_1 states are shorter than in singlets. Also, it is clear that one Au--Au bond is much shorter than the other two in the stack. This phenomenon is due to the formation of excimeric complexes consistent with cyclo-[$M_3(Pz)_3$] (M = Cu/Ag/Au and Pz = pyrazolate) DOT complexes, as reported earlier and discussed above in the experimental section[3b,23]. One other important distinction in comparing S_0 **VIII** and **IX** complexes is that Au--Au bonds are ~ 0.15 Å shorter for the latter versus the former complex. This agrees with the previous discussion of the crystallographic database analysis about H-T and H-H imine interactions. We propose that this is

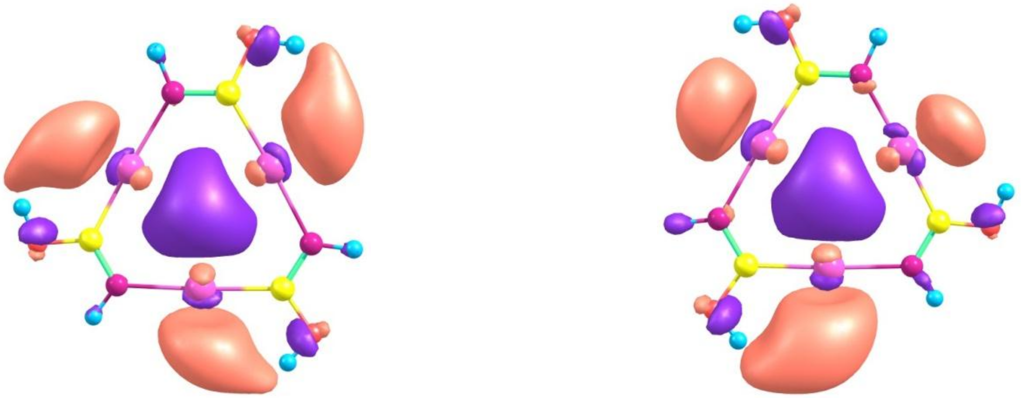

LUMO+1 (-0.932 eV) SUMO+1 (-1.207 eV)

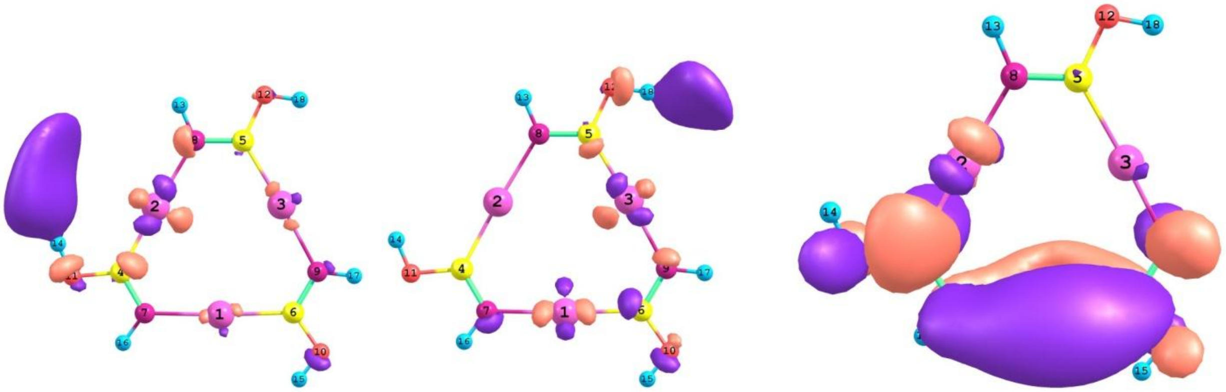

Degenerate LUMO (-0.955 eV) Upper SOMO (-2.077 eV)

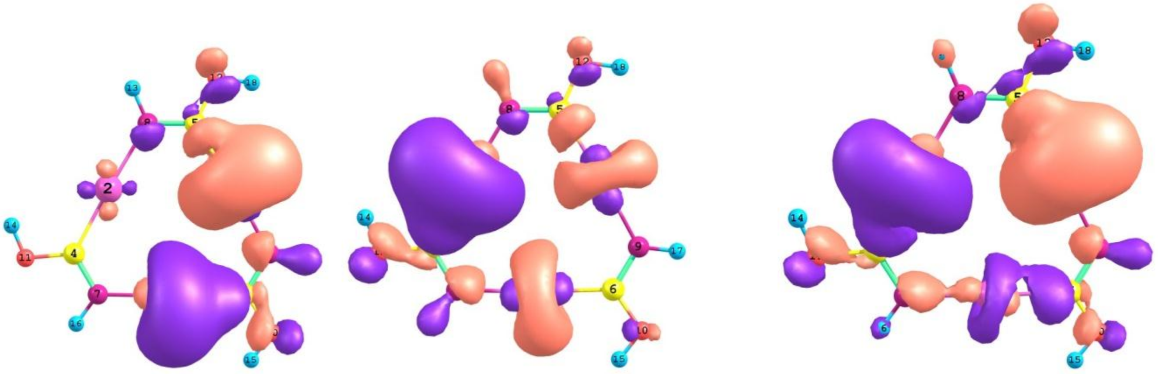

Degenerate HOMO (-6.759 eV) Lower SOMO (-6.835 eV)

Figure 5.23. Contours of frontier orbitals of MOTs with S_0 complexes on left and T_1 on the right. Note that some S_0 orbitals are degenerate. The corresponding orbital energies are given in eVs. HOMO, LUMO, SOMO, SUMO represents the highest occupied, lowest unoccupied, singly occupied, singly unoccupied molecular orbitals respectively.

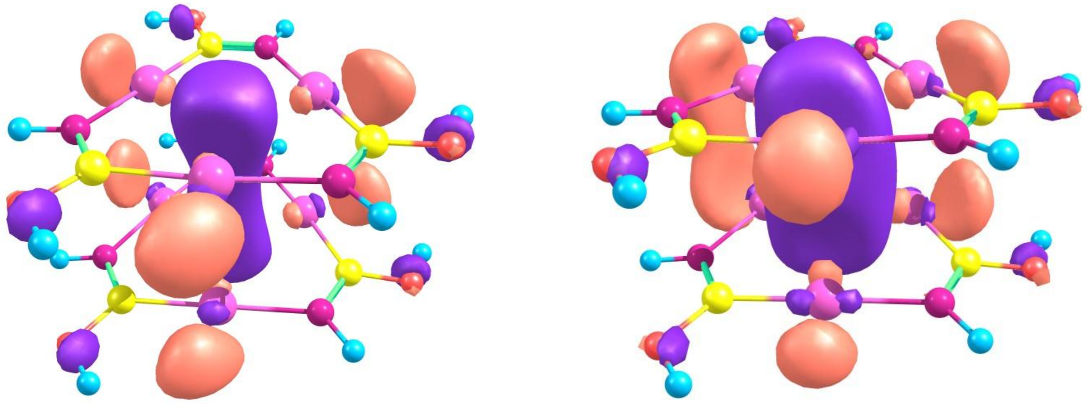

LUMO Upper SOMO

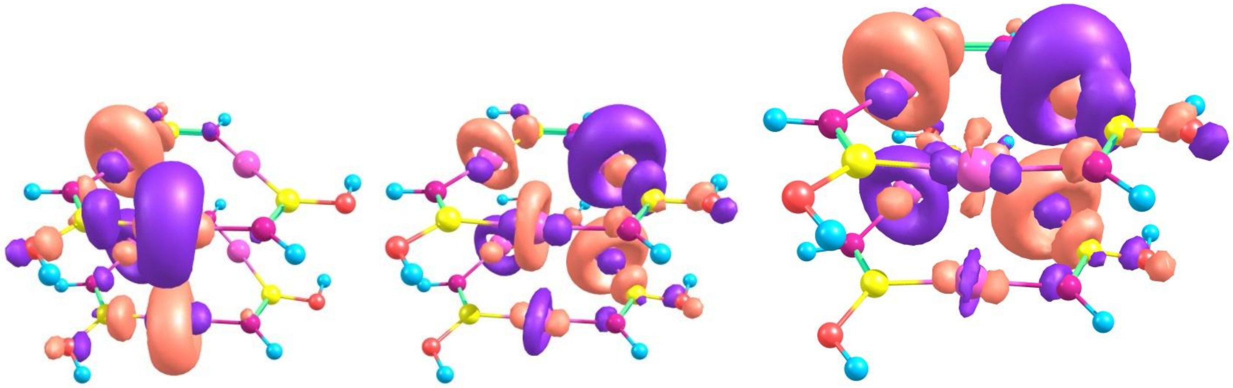

Degenerate HOMO Lower SOMO

Figure 5.24. Contours of frontier orbitals of DOTs with S_0 complexes on left and T_1 on the right. Note that some S_0 orbitals are degenerate. HOMO, LUMO, SOMO, SUMO represents the highest occupied, lowest unoccupied, singly occupied, singly unoccupied molecular orbitals respectively.

due to an enhanced electrostatic interaction (supported by both Mulliken and Natural Population analysis) in the H-T (**IX**) complex vs. the H-H (**VIII**) complex as the inter-trimer aurophilic distance, and presumably strength of interaction, in each complex remains the same for both **VIII** and **IX**. Also, it is important to recall that PW-DFT bang gap studies reported earlier in this chapter predicted that, shorter the inter-trimer distances (R), better the conduction in the trimers. Hence, we propose that H-T complexes which bear shorter inter trimer Au--Au distances may act as better conductors as compared to H-H materials.

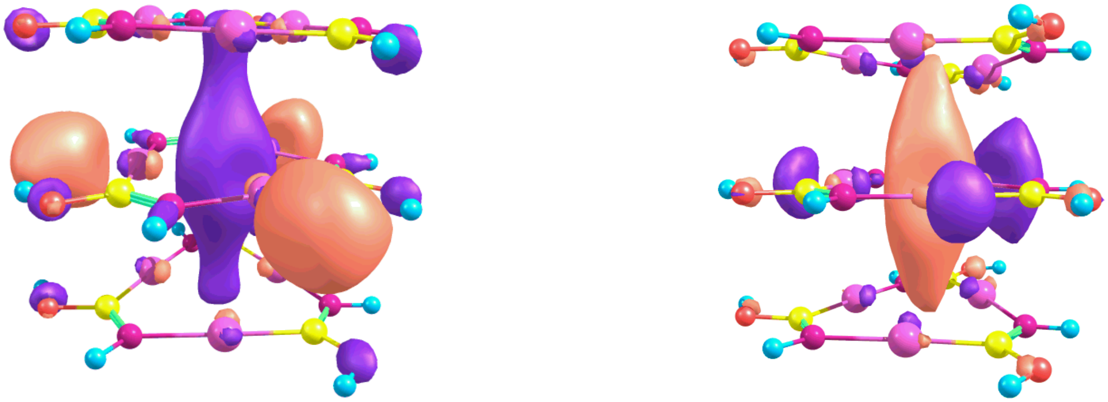

LUMO Upper SOMO

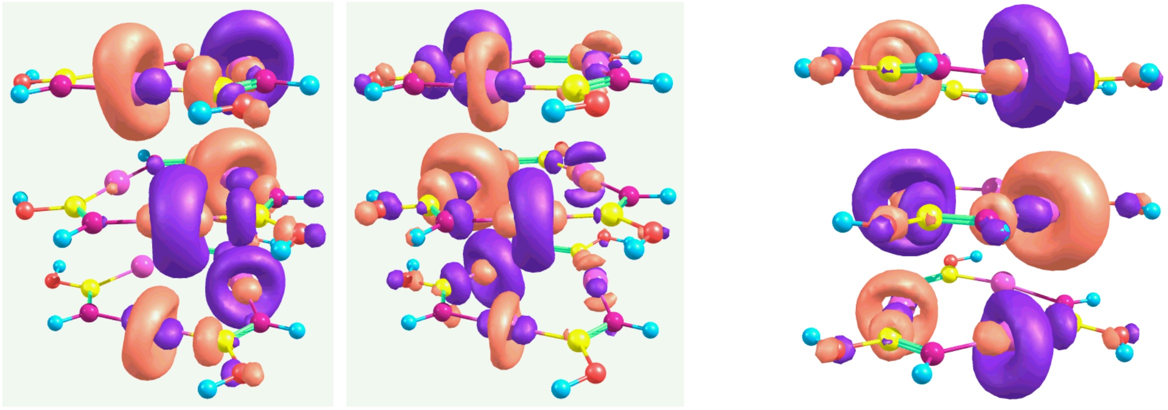

Degenerate HOMO Lower SOMO

Figure 5.25. Contours of frontier orbitals of TOTs with S_0 complexes on left and T_1 on the right. Note that some S_0 orbitals are degenerate. HOMO, LUMO, SOMO, SUMO represents the highest occupied, lowest unoccupied, singly occupied, singly unoccupied molecular orbitals respectively.

Electronic Properties: Frontier orbitals of S_0/T_1 states of d^{10} complexes were studied/reported earlier by many research groups including our own[3b,23]. Contours of frontier orbitals (Figure 5.23 - 5.25) for S_0/T_1 states of cyclo-[$Au_3(HN{=}COH)_3$] DOT/TOT (XII, XIII, XIV) complexes are consistent with previous studies on coinage metal-pyrazolate cyclo-trimers[23]. For all optimized DOT/TOT models, there is a doubly degenerate HOMO and a non-degenerate LUMO for the S_0 ground state (Figure 5.24, 5.26). Contours of singly occupied/unoccupied molecular orbitals (SOMO/SUMO) of optimized T_1 states of DOT/TOT complexes indicate the higher energy SOMO of the T_1 states correspond to the LUMO of the S_0

states, which again is consistent with earlier studies[3b,23]. The upper SOMO of T_1 and the LUMO of S_0 states show pronounced delocalized, inter-trimer excimeric bonding across multiple gold centers. They also show increased inter-trimer bonding in DOT/TOT complexes. Note that the frontier orbitals of the MOT models are slightly different with both a doubly degenerate HOMO and LUMO for the S_0 ground state (Figure 5.23). However, the LUMO+1 of the MOT is only 0.023 eV above the LUMO, and has delocalized orbitals inside the trimer ring, which yields inter-trimer excimer bonding (Figure 5.23) [23].

Note also that the frontier orbitals of S_0 and T_1 states of MOT/DOT/TOT complexes of cyclo-[$Au_3(MeN{=}COMe)_3$], cyclo-[$Au_3(MeN{=}CO^nBu)_3$] obtained by similar molecular DFT calculations from X-ray (as opposed to DFT-optimized) geometries (not presented in this report), yields similar results in terms of frontier orbital composition, which is predominantly within the metallocycle ring as in cyclo-[$Au_3(HN{=}COH)_3$]. This indicates that the substituents on the carbeniate ligand would have minimal influence on the HOMO/SOMO and LUMO/SUMO composition of S_0/T_1 states of gold carbeniate complexes. In addition, note that the morphology of the trimer complexes would be expected to have less effect on the HOMO than the LUMO composition given its disposition. This contention is supported by comparing the HOMO/SOMO and LUMO/SUMO of S_0/T_1 states of eclipsed vs. staggered vs. chair conformations of MOT/DOT/TOT of cyclo-[$Au_3(HN{=}COH)_3$] complexes (Figure 5.23 – 5.27).

Spectroscopic Properties: Excitation ($S_0 \rightarrow T_1$) and emission ($T_1 \rightarrow S_0$) energies and Stokes' shifts (SS) are calculated on the MOT, DOT and TOT models (Table 5.4). It is important to notice that that the overall excitation energies and Stokes' shift typically decreases as the extent of trimer stacking increases and this agrees with the experimental results (Table 5.2). The only exception being the SS of TOT, which may be attributed to the increase in the inter-trimer

Au--Au distances caused by the rotational motion (Θ) of one trimer relative to the other along the three-fold axis (Figure 5.25). Also, it was found that these spectroscopic energies decrease for the H-T conformation (**IX**) vs. the H-H conformation (**VIII**), which is plausibly due to the augmented electrostatic interaction enhancing inter-trimer bonding and this agrees with the experimental trend as well (Table 5.2). The experimental and calculated trend of decreasing Stokes' shift energies with an increase in the extent of trimer stacking and decreased inter-trimer distances supports the proposal that these Au_3Cb_3 complexes may act as good conducting materials when stacked in solid state, especially in H-T conformation.

Table 5.4. Inter-trimer aurophilic bonds and spectroscopic properties of cyclo-[$Au_3(HN{=}COH)_3$] complexes.

Structure number	Inter Trimer Au--Au bonds (Å)		Excitation $S_0 \rightarrow T_1$ (eV)	Emission $T_1 \rightarrow S_0$ (eV)	Stokes' Shift (eV)
	Neutral/Singlet	Neutral/Triplet			
VII (MOT)	-	-	4.93	1.44	3.49
VIII (DOT H-H)	3.302, 3.303, 3.306	2.941, 3.068, 3.217	3.80	3.34	0.46
IX (DOT H-T)	3.250, 3.250, 3.262	2.977, 2.977, 3.226	3.72	3.28	0.44
X (TOT H-H)	3.340, 3.340, 3.340	2.978, 3.292, 3.300	3.40	2.87	0.54

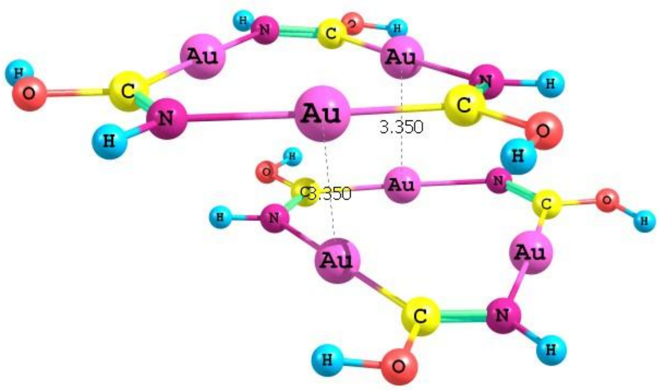

Figure 5.26. Pictorial representation of a chair structure for DOT of cyclo-[$Au_3(HN{=}COH)_3$].

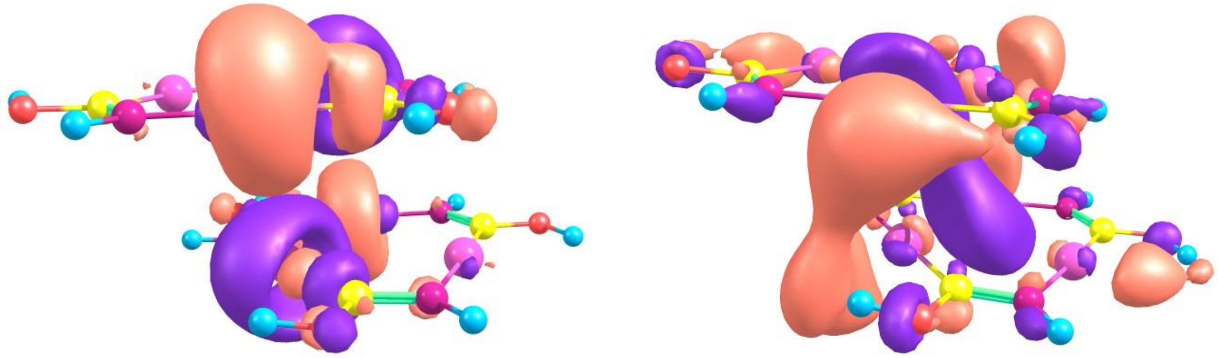
HOMO LUMO

Figure 5.27. Contours of frontier orbitals of singlet chair structure for DOT of cyclo-[$Au_3(HN=COH)_3$] complex. HOMO, LUMO represents the highest occupied, lowest unoccupied molecular orbitals respectively.

In order to distinguish the effect of trimer morphology on their spectroscopic properties, excitation and emission energies of eclipsed (**VII**) and chair (Figure 5.26) DOT complexes are compared. The emission/excitation/Stokes'-shift energies of the chair conformer (Figure 5.26) are found to be 4.04/3.49/0.54 eV respectively, which are higher than the corresponding excitation/emission/Stokes'-shift energies for the eclipsed conformer by 0.24/0.16/0.08 eV respectively. From this molecular-based comparison, we conclude that eclipsed DOT might be a better conductor than the chair given their respective spectroscopic energies, which corroborates the PW-DFT calculations as the BG for the eclipsed unit cell is 0.35 eV less than the chair unit cell.

Charge Transport Properties: In organic semiconductors, electronic charge transport parameters are dependent on strong coupling between geometric and electronic structures[26]. Degree of chain order (in polymers) and solid state packing (in crystals) of organic semiconductors are very critical for efficient charge transport[27]. At the microscopic level, charge transport parameters can be described using Marcus theory of electron transfer[26-28]. At high temperatures (room temperature), the electron transfer/hopping rate (k_{et}) can be approximated as[27, 29]

$$k_{et} = \frac{4\pi^2}{h} \frac{1}{\sqrt{4\pi\lambda k_b}} t^2 \, exp\left(-\frac{\lambda}{4k_b T}\right) \tag{5.1}$$

Equation 5.1 is governed by two parameters: the intermolecular transfer integral (t), and the intramolecular reorganization energy (λ). T, k_b, h represent temperature, Boltzmann's constant and Planck's constant, respectively. For a more in-depth discussion of the theoretical basis and description of λ and t see references 26-29.

Marcus theory can also be applied to metal-organic semiconducting materials such as cyclo-[Au_3(RN=COR')$_3$] complexes. In this research, we have calculated the intramolecular reorganization energies (λ) of cyclo-[Au_3(RN=COR')$_3$] (R=H/Me and R'=H/Me/^{n}Bu) complexes at both cationic and anionic charged states. Reorganization energies (λ) can be calculated using two methods: the adiabatic potential method and the normal mode analysis.[29a] Here we use the adiabatic potential method to determine the reorganization energies. Calculated reorganization energy (λ) values of cyclo-[Au_3(RN=COR')$_3$] complexes, for both hole (λ-Cation / λ^+) and electron (λ-Anion / λ^-) states are reported in Table 5.5. We also report molecular adiabatic/vertical ionizations (IP) and electron affinities (EA) for the above mentioned gold carbeniate (Au_3Cb_3) complexes. Vertical ionization (VIP) and electron affinity (VEA) represent IP and EA of Au_3Cb_3 complexes at their neutral geometry; whereas the adiabatic ionization (AIP) and electron affinity (AEA) represent IP and EA of Au_3Cb_3 complexes at their respective optimized charge (cation/anion) geometry, Table 5.5.

Table 5.5. Charge transport properties of cyclo-[$Au_3(RN{=}COR')_3$] complexes. VIP, AIP, VEA, AEA and λ represents vertical ionization, adiabatic ionization, vertical electron affinity, adiabatic electron affinity and reorganization energy, respectively.

Complex Name	VIP / VEA (eV)	AIP / AEA (eV)	λ-Cation (λ^+) (eV)	λ-Anion (λ^-) (eV)
cyclo-[$Au_3(HN{=}COH)_3$]	8.377 / 0.446	8.091 / 0.285	0.287	0.161
cyclo-[$Au_3(MeN{=}COMe)_3$]	7.724 / 0.778	7.431 / 0.407	0.293	0.371
cyclo-[$Au_3(MeN{=}CO^nBu)_3$]	7.486 / 0.819	7.169 / 0.441	0.317	0.379

Comparison of calculated reorganization energies of cyclo-[$Au_3(RN{=}COR')_3$] (R = H/Me and R' = H/Me/^{n}Bu) complexes indicate that the λ values for both a hole and an electron increase with the addition of bulky substituents (For R' = H/Me/^{n}Bu; λ^+ = 0.287/0.293/0.317 and λ^- = 0.161/0.371/0.379 eV) on the ligands of the gold carbeniate metallocycle. A similar trend is also observed with the respective VEA and AEA values, Table 5.5. However, one interesting difference among the 3 complexes (Table 5.5) studied here are the VIP and AIP values of cyclo-[$Au_3(HN{=}COH)_3$] (VIP/AIP = 8.38/8.09 eV), which are higher than the other 2 complexes cyclo-[$Au_3(MeN{=}COMe)_3$] (VIP/AIP = 7.724/7.431 eV) and cyclo-[$Au_3(MeN{=}CO^nBu)_3$] (VIP/AIP = 7.486/7.169 eV). Furthermore, we can observe that for the complex with R' = H, λ^- (0.161 eV) is lower than its λ^+ (0.287 eV) indicating that reorganization is less for electron transport than hole transport for the cyclo-[$Au_3(HN{=}COH)_3$] complex, whereas the opposite trend is observed for complexes with R' = Me/^{n}Bu (compare λ^+ and λ^- values, Table 5.5). The reason for higher λ^+ values for cyclo-[$Au_3(HN{=}COH)_3$] complex can be attributed to the increase in the respective VIP (8.377 eV) and AIP (8.091 eV) values.

As mentioned earlier[26,27b,29], at the microscopic level, along with reorganization energy (λ), the intermolecular transfer integral (t) is an important contributor to determine the electron transfer rate in organic/metal-organic semiconductors. Due to the formation of extended chains (Figures 5.2 (**I**, **II**), 5.3) along the c-axis of the unit cell[5] and also due to shorter intermolecular distances of cyclo-[Au_3(RN=COR')$_3$] complexes, we anticipate that these complexes have strong electronic couplings (significant transfer integral (t) values) especially along the c-axis and lower effective masses for charge carriers. Future studies are planned in this direction to obtain a comprehensive picture of charge transport properties of these gold(I) cyclo-trimers to guide the ongoing synthesis and device work.

5.4 Summary and Conclusions

A combined experimental (by Roy N. McDougald in the Omary group at UNT) and computational study on different cyclo-[Au_3(RN=COR')$_3$] complexes (where R and R' are a selection of substituents) is performed. Experimental studies include synthesis, x-ray structure (both not presented in this chapter) and photophysical characterization of selected novel gold(I) carbeniate complexes (Figures 5.2(**I**), 5.3–5.6).

Examination of the x-ray crystal structures of cyclo-[Au_3(RN=COR')$_3$] complexes synthesized in the Omary lab and those in the literature[5-8] indicated that gold (I) carbeniate complexes form polymorphic structures with variations of ligand substituents (R, R') and crystal growth conditions. Photoluminescence studies showed that the polymorphs exhibit distinct spectroscopic properties pertaining to the number of aurophilic bonds and Au--Au bond distances in their crystal geometries. Among a variety of [Au_3(RN=COR')$_3$] polymorphic structures synthesized by Balch's group and at UNT, we found that only two infinitely extended chain structures, [Au_3(MeN=COMe)$_3$] and [Au_3(MeN=CO^{n}Bu)$_3$] have smaller Stokes' shifts, and shorter Au--Au bond distances, indicating that these materials may have suitable photophysical and conduction properties for molecular electronic devices. An interesting structural disparity between these two extended stacking complexes, [$Au_3(MeN{=}COMe)_3$] and [$Au_3(MeN{=}CO^nBu)_3$] is that they stack in the head to head (H-H) and head to tail (H-T) conformations respectively (Figure 5.12). This orientation is due to the asymmetric, μ-N,C nature of the bidentate carbeniate ligand.

Due to the differences in the spectroscopic properties of [$Au_3(RN{=}COR')_3$] complexes bearing numerous polymorphic structures reported from present and earlier[5-8] experiments, we performed a comprehensive computational study of different structural forms of Au_3Cb_3 complexes under both molecular and periodic regimes. The goal of the computational modeling is to seek the structure-property relationship between the geometric stacking of different polymorphic [$Au_3(RN{=}COR')_3$] complexes and their respective optoelectronic and conduction properties. Periodic and molecular simulations were performed on all possible stacking patterns (Figure 5.13) of Au_3Cb_3 complexes. Given our goal to study the effect of "geometric stacking" on electronic properties, it was considered prudent to use the same substituents to minimize differences due to the donor/acceptor properties of R and R', we chose R = R' = H.

Periodic simulations are performed on multiple solid state geometries constructed (vide supra) based on experimental crystal structures. The periodic band gap and relative energies were chosen as the determining parameters to examine the conductivity in constructed solid state structures. In addition, simulations of the ground, excited and ionized states are performed on molecular models of [$Au_3(HN{=}COH)_3$] complexes to augment the periodic simulation results and establish their relationship with optoelectronic and conduction properties. The spectroscopic Stokes' shifts and the intramolecular reorganization energy (λ) of charged species were chosen as the determining parameters to examine the conductivity at the molecular level.

Both periodic and molecular simulations on constructed models of [$Au_3(HN=COH)_3$] complexes indicated that the infinitely extended chain of eclipsed head to tail (H-T) structures with equidistant Au--Au aurophilic bonding can have lower band gaps, smaller Stokes' shifts and reorganization energies (λ). These simulations predict that if such an extended chain of [$Au_3(RN=COR')_3$] complexes with non-bulky substituents were to be synthesized, they may act as ideal semiconducting materials for molecular electronic devices. However, it is also important to note that the device performance is not only dependent on the properties of the semiconducting material alone but also on its interface characteristics with other device components.

5.5 Chapter References

(1) (a) Cotton, F. A.; Wilkinson, G.; Murrillo, C. A.; Bochmann, M. In *Chapter 18; Advanced Inorganic Chemistry*; Wiley-Interscience: New York, **1999**. (b) Shriver, D. F.; Kaesz, H. D.; Adams, R. D. *The Chemistry of Metal Clusters Complexes*, VCH Publishers, Inc.: New York. **1990**.

(2) (a) Yang, X.; Zheng, Z.; Knobler, C. B.; Hawthorne, M. F. *J. Am. Chem. Soc.* **1993***, 115*, 193-195. (b) Ehlert, M. K.; Rettig, S. J.; Storr, A.; Thompson, R. C.; Trotter, J. *Can. J. Chem.* **1990***, 68*, 1444-1449. (b) Raptis, R. G.; Fackler, J. P. *Inorg. Chem.* **1988***, 27*, 4179-4182. (c) Sartori, P.; Golloch, A. *Chem. Ber.* **1968***, 101*, 2004-2009.

(3) (a) Dias, H. V. R.; Diyabalanage, H. V. K.; Eldabaja, M. G.; Elbjeirami, O.; Rawashdeh-Omary, M. A.; Omary, M. A. *J. Am. Chem. Soc.* **2005***, 127,* 7489-7501. (b) Omary, M. A.; Rawashdeh-Omary, M.; Gonser, M. W. A.; Elbjeirami, O.; Grimes, T.; Cundari, T. R.; Diyabalanage, H. V. K.; Gamage, C. S. P.; Dias, H. V. R. *Inorg. Chem.* **2005***, 44*, 8200-8210. (c) Yang, C.; Messerschmidt, M.; Coppens, P.; Omary, M. A. *Inorg. Chem.* **2006***, 45*,

6592-6594. (d) Rawashdeh-Omary, M. A.; Rashdan, M. D.; Dharanipathi, S.; Elbjeirami, O.; Ramesh, P.; Dias, H. V. R. *Chem. Commun.* **2011**, *47*, 1160–1162. (e) Elbjeirami, O.; Rawashdeh-Omary, M. A.; Omary, M. A. *Research Chem. Intermed.* **2011***, 37,* 691-703. (f) Forward, J. M.; Fackler, J. P., Jr.; Assefa, Z. *Photophysical and Photochemical Properties of Gold(I) Complexes*. In *Optoelectronic Properties of Inorganic Compounds,* Roundhill, D. M.; Fackler, J. P., Jr. Eds.; Plenum: New York, 1999, Chapter 6. (g) Omary, M. A.; Mohamed, A. A.; Rawashdeh-Omary, M. A.; Fackler, J. P., Jr. *Coord. Chem. Rev.* **2005**, *249*, 1372-1381.

(4) (a) Pyykkö, P. *Chem. Rev.* **1997***,* 97, 597-636. (b) Pyykkö, P. *Angew. Chem. Int. Ed.* **2004**, *43*, 4412-4456. (c) Pyykkö, P. *Inorg. Chim. Acta* **2005**, *358*, 4113-4130.

(5) (a) Vickery, J. C.; Olmstead, M. M.; Fung, E. Y.; Balch, A. L. *Angew. Chem. Int. Ed. (English)* **1997***, 36*, 1179-1181. (b) White-Morris, R.; Olmstead, M. M.; Attar, S.; Balch, A. L. *Inorg. Chem.* **2005***, 44*, 5021-5029. (c) Winkler, K.; Wysocka-Zolopa, M.; Recko, K.; Dobrzynski, L.; Vickery, J. C.; Balch, A. L. *Inorg. Chem.* **2009***, 48*, 1551-1558.

(6) (a) Schmidbaur, H.; Graf, W.; Müller, G. *Angew. Chem. Int. Ed. (English)* **1988***, 27*, 417-419. (b) Harwell, D. E.; Mortimer, M. D.; Knobler, C. B.; Anet, F. A. L.; *J. Am. Chem. Soc.* **1996***, 118*, 2679-2685. (c) Vickery, J. C.; Balch, A. L. *Inorg. Chem.* **1997***, 36*, 5978-5983.

(7) Olmstead, M. M.; Jiang, F.; Attar, S.; Balch, A. L. *J. Am. Chem. Soc.* **2001***, 123*, 3260-3267.

(8) Fung, E. Y.; Olmstead, M. M.; Vickery, J. C.; Balch, A. L. *Coord. Chem. Rev.* **1998***, 171*, 151-159.

(9) Allen, F., *Acta Cryst.* **2002***, 58*, 380-388.

(10) Kresse, G.; Furthmüller, J. *Comp. Mat. Sci.* **1996**, *6*, 15-50.

(11) Kresse, G.; Furthmüller, J. *Phys. Rev. B* **1996**, *54*, 11169.

(12) Kresse, G.; Joubert, D. *Phys. Rev. B* **1999**, *59*, 1758.

(13) Perdew, J. P.; Burke, K.; Ernzerhof, M. *Phys. Rev. Lett.* **1996**, *77*, 3865.

(14) Monkhorst, H. J.; Pack, J. D. *Phys. Rev. B* **1976**, *13*, 5188.

(15) Frisch, M. J.; et al. Gaussian 09, Revision A.1, Gaussian, Inc., Wallingford CT **2009**.

(16) Hay, P.; Wadt, W. *J. Chem. Phys.* **1985**, *82*, 270.

(17) Barakat, K. A.; Cundari, T. R.; Rabaa, H.; Omary, M. A. *J. Phys. Chem. B* **2006**, *110*, 14645-14651.

(18) Zhao, Y.; Truhlar, D. *Theor. Chem. Acc.* **2008**, *120*, 215-241.

(19) Pyykkö, P.; Mendizabal, F. *Inorg. Chem.* **1998**, *37*, 3018-3025.

(20) Couty, M.; Hall, M. B. *J. Comp. Chem.* **1996**, *17*, 1359-1370.

(21) (a) Stephens, P. J.; Devlin, F. J.; Chabalowski, C. F.; Frisch, M. J. *J. Phys. Chem.* **1994**, 98, 11623-11627. (b) Becke, A. D. *Phys. Rev. A* **1988**, *38*, 3098. (c) Lee, C.; Yang, W.; Parr, R. G. *Phys. Rev. B* **1988**, *37*, 785.

(22) Møller, C.; Plesset, M. S. *Phys. Rev.* **1934**, *46*, 618.

(23) Grimes, T.; Omary, M. A.; Dias, H. V. R.; Cundari, T. R. *J. Phys. Chem. A* **2006**, *110*, 5823-5830.

(24) Bartolomé, C.; Carrasco-Rando, M.; Coco, S.; Cardovilla, C.; Espinet, P.; Martín-Alvarez, J. M. *Organometallics* **2006,** *25*, 2700 .

(25) Tiripicchio, A.; Camellini, M. T.; Minghetti, G. *J. Organomet. Chem.* **1979**, *171*, 399-406.

(26) (a) Bao, G.; Locklin, J. In *Section 1.1; Organic Field-Effect Transistors*; CRC Press: Boca Raton. **2007**. (b) Brédas, J.L.; Beljonne, D.; Coropceanu, V.; Cornil, J. *Chem. Rev.* **2004,** *104*, 4971-5003.

(27) (a) Cornil, J.; Calbert, J.P.; Brédas, J.L. *J. Am. Chem. Soc.* **2001**, *123,*1250-1251. (b) Brédas, J.L.; Cornil, J.; da, D.A.; Filho, S. *PNAS* **2002**, *99*, 5804-5809. (c) Cornil, J.; Beljonne, D.; Calbert, J.P.; Brédas, J.L. *Adv. Mater.* **2001**, *13*, 1053-1067. (d) Mas-Torrent, M.; Hadley, P.; Bromley, S.T.; Ribas, X.; Tarrés, J.; Mas, M.; Molins, E.; Veciana, J.; Rovira, C. *J. Am. Chem. Soc.* **2004**, *126*, 8546-8553. (e) Bromley, S.T.; Mas-Torrent, M.; Hadley, P.; Rovira, C. *J. Am. Chem. Soc.* **2004**, *126*, 6544-6545.

(28) (a) Marcus, R. A. *Rev. Mod. Phys.* **1993**, *65*, 599. (b) Marcus, R. A. *J. Chem. Phys.* **1956**, *24*, 966 and 979. (c) Marcus, R. A.; Sutin, N. *Biochim. Biophys. Acta* **1985**, *811*, 265.

(29) (a) Delgado, M. C.; Pigg, K. R.; da, S. F.; Gruhn, N. E.; Sakamoto, Y.; Suzuki, T.; Osuna, R. M.; Casado, J.; Hernández, V.; Navarrete, J. T. L.; Martinelli, N. G.; Cornil, J.; Sánchez-Carrera, R. S.; Coropceanu, V.; Brédas, J.L. *J. Am. Chem. Soc.* **2009**, *131*, 1502-1512. (b) Chen, H.; Chao, I. *Chem. Phys. Lett.* **2005**, *401*, 539-545.

CHAPTER 6

MODELING DEPOSITION OF METAL ATOMS ON A P-TYPE ORGANOMETALLIC CONDUCTOR: IMPLICATIONS FOR STABILITY AND ELECTRON TRANSFER

6.1 Introduction

A variety of trinuclear nine-membered rings with Au(I) ions and monoanionic bidentate ligands (L) of C-C, C-N, N-N ligation have been synthesized by several different groups over the past three decades[1-7]. These trigold(I) complexes (cyclo-[Au(μ-L)]$_3$) (see Figure 6.1 for a characteristic example) exhibit approximate D_{3h} symmetry[8]. Aurophilic interactions result from a combination of correlation and relativistic effects[9,10] and are generally marked by Au-Au distances of less than 3.6 Å. Aurophilic interactions are partly responsible for the formation of a variety of Au_3L_3 solid-state structures, for example, individual complexes, dimers of trimers, supramolecular stacks, etc. Many cyclo-[Au(μ-L)]$_3$ complexes exhibit remarkable properties such as π-acidity and basicity, luminescence, thermochromism, solvoluminescence[7,11,12], excimeric bonding, and thus find application in metal-organic electronics such as organic light emitting diodes (OLEDs)[13], solar cells, photovoltaics and metal organic field effect transistors (MOFETs)[14].

Many d^{10} transition metal (TM) pyrazolate (Pz) trimers (cyclo-[TM(μ-Pz)]$_3$) have been synthesized with various organic substituents on the pyrazolate ligands[12,15]. In collaboration with Omary's group, our own group has researched luminescence properties for cyclo-[TM(μ-Pz)]$_3$ trimers (where TM = Ag, Au, Cu) with –CF_3 substituents on pyrazolate ligands[7]. It has been

---

* This entire chapter is reproduced from [Chilukuri, B.; Cundari, T. R. "Modeling the Deposition of Metal Atoms on a p-Type Organometallic Conductor: Implications for Stability and Electron Transfer" *The Journal of Physical Chemistry C* **2011,** vol. *115*, pp 5997-6003.], with permission for electronic and print publication in thesis and dissertation from the American Chemical Society (ACS) to Bhaskar Chilukuri # 3000501953.

demonstrated via a combination of experiment and modeling that cyclo-[Au(μ-Pz)]$_3$ (Figure 6.1) is among the most π-basic of this family of coinage metal trimers. The π-acidity and π-basicity was assessed using molecular electrostatic potentials (MEPs), HOMO (Highest Occupied Molecular Orbital) and LUMO (Lowest Unoccupied Molecular Orbital) energies, positive charge attraction energies, etc. The simulations revealed that cyclo-[Au(μ-Pz)]$_3$ trimers act as good π-bases, and so should be good models for p-type conductors in molecular electronics[16]. For example, we recently reported the synthesis, characterization and computational modeling of stacked trimers, [Ag(μ-Tz-(n-C_3F_7)$_2$)]$_3$•[Au(μ-Pz-(i-C_3H_7)$_2$)]$_3$ (Tz = triazolate), where the cyclo-[Au(μ-Pz)]$_3$ donor is a p-type conductor in a p-n blended material[17]. In addition cyclo-[Au(μ-Pz)]$_3$ complexes have also been used in applications that exploit their catalytic redox activity, metallomesogenic character, and photonic properties[18]. Reference 12 summarizes gold(I) pyrazolate complexes.

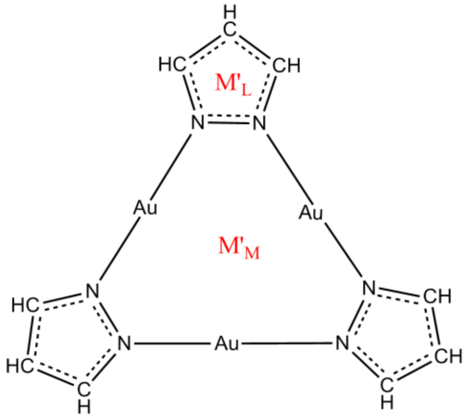

Figure 6.1. Structure of cyclo-[Au(μ-Pz)]$_3$ (Pz = Pyrazolate) trimer. M'$_L$ and M'$_M$ represent the ligand (L) and metal (M) deposition sites for different electrode metals (M') on the cyclo-[Au(μ-Pz)]$_3$ trimer.

In electronic devices, source and drain electrodes are usually metals, and are important components in determining the performance of a device[19]. Several metals have been tested or used as electrodes in electronic devices depending upon the type of conducting material, surrounding environment, surface chemistry with interacting materials and most importantly the right work function. Source and drain contacts are critical for effective charge transfer in electronic devices. In OLEDs, electrons and holes are injected from metal contacts into an organic or organometallic material where they subsequently recombine to emit light. Selection of metals with appropriate work functions is thus essential to avoid any barrier between the contacts that can impede the flow of charge in the device[20]. As the channel length decreases, the contact resistance between the source/drain electrodes and the semiconductor becomes increasingly important to device performance[21]. Hence, understanding the geometric and electronic properties of the contacts and their dependence on electrode materials has become increasingly important for processing organic semiconductors as researchers seek to go from molecular level control of properties to real-world device fabrication perspective.

In this paper, the interaction of different electrode metal atoms (M') with cyclo-[Au(μ-Pz)]$_3$ trimer(T) (Figure 6.1) is modeled. These electrode metals were chosen to assess metal-trimer interactions for M'= Al, Au, Cu, La, Ni, Pd, Pt, Ru, Ni. All these metals are currently used as electrodes in electronic devices[19]. Modeling the interactions of atoms with semiconductors is an important first step in modeling full electrode metal surfaces because in a device there is the possibility of diffusion of metal atoms from the slab into the semiconductor layer causing instability and inferior device performance. Stability of the device is very important and can be modeled partly by studying the metal atom interactions with the semiconductor, as we have done in this paper. Also molecular calculations can help better understand the type of bonding interactions that lead to charge transfer between interfaces.

6.2 Computational Methodology

Geometry optimizations and single point calculations of cyclo-[Au(μ-Pz)]$_3$ trimer and metal (M')-trimer complexes are performed using the Gaussian09 program[22]. Molecular DFT calculations are carried out with the B3LYP hybrid functional[23-25] in conjunction with the CEP-31G(d) pseudopotential basis set[26-28], where (d) signifies addition of a d-polarization function to main group elements. No imaginary frequencies are observed for the optimized structures, as confirmed by calculation of the energy Hessian. Also the spin contamination (<S**2> value) for the calculations is negligible (< 1% deviation) for all the structures.

The B3LYP functional and basis set have been proven to be valuable for studying metallocyclic trimer compounds in many earlier studies and the geometries and energies correlate well with the experimental results[7,16,29]. In addition we also compared the geometries obtained from B3LYP with the B3PW91[30,31] hybrid functional (results not presented in the paper) using the same basis set, which gave similar geometries for coinage metal-trimer complexes. In light of the study of Buhl et al. on the geometries of transition metal complexes with different DFT functionals[32-34], we selected the B3LYP functional for the current study.

Molecular orbital occupancies and atomic charges are obtained by performing a natural population analysis (NPA)[35,36] within the Gaussian suite of programs. The results from Gaussian-DFT calculations are utilized to plot the density of states (DOS) by expanding the atomic orbital occupancies using a gaussian expansion scheme within the AOMix program[37,38]. The full width at half maximum (FWHM) value used in the gaussian expansion scheme is 0.5 eV.

6.3 Results and Discussion

Deposition of an electrode metal (M') on to cyclo-[Au(μ-Pz)]$_3$ trimer leads to two possible bonding sites (Figures 6.1 and 6.2): (a) a gold (M'$_M$) metallocycle binding site, or (b) an organic ligand (M'$_L$) site. Our goal is to assess the preference of protypical electrode metals of high and low work function for a metal or organic binding site with this p-type material. Additionally, the geometric relaxation of cyclo-[Au(μ-Pz)]$_3$ upon coordination of M' is relevant to the efficiency of charge transfer across the electrode/conductor interface as well as the stability of the interface. A single metal atom, ligated in a π-type manner, i.e., coordinated the face of the Au_3 triangle and a single Pz of the substrate, is utilized as a model. These choices are supported by experimental crystal structures of several metal/cyclo-[M(μ-L)]$_3$) structures that highlight the π-acid/base nature of these trimers[17]. The former choice allows us to delineate metal/Au from organic/Pz binding preferences, and is a necessary precursor to research on cyclo-[M(μ-L)]$_3$) bound to various electrode metal surfaces.

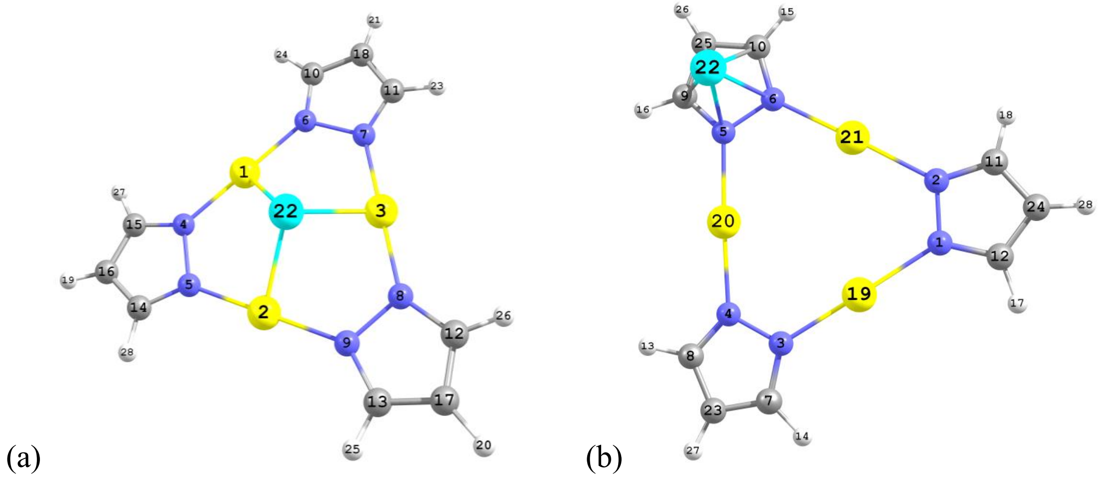

Figure 6.2. Possible deposition sites for metal atoms (M') on a cyclo-[Au(μ-Pz)]3 trimer. The figure on the left and right represent the metal site (M'M) and the ligand site (M'L), respectively. The metal atoms are colored blue, gold - yellow, nitrogen - violet, carbon – grey, hydrogen - white. Each element is numbered in both the molecules (these numbers are later used to explain geometric properties).

One may expect that the metal atoms (M') used in the study may replace Au from the trimer (T) skeleton and this could affect the stability of the T species for device applications. However, the experimental literature[39] and expansion thereof to generalize the phenomenon[40], show that mixing of other metals like Ag, Tl, Na, Li, etc. with cyclo-[Au(μ-L)]$_3$ complexes attains π-complexes (as calculated here) rather than displacing one of the ring atoms. Furthermore, preliminary data by our device collaborators[41] show that thermal deposition or solution casting of thin films of gold trimers on various metal cathodes retains the molecular structure of such cyclo-[Au(μ-L)]$_3$ trimer complexes, as evidenced by IR and photoluminescence data.

6.3.1 Metal Binding Characteristics

Geometry optimization of M'/cyclo-[Au(μ-Pz)]$_3$ complexes at the two studied deposition sites for M' on the Au trimer (Figure 6.2) is performed at the DFT level. The isolated cyclo-trimer has a singlet ground state. Hence, the spin multiplicity (2S+1) for all metal-trimer complexes (M'-T) considered here reflects the ground state multiplicity of M'.

The stability of electrode metals (M') at the gold trimer (T) binding sites is determined from the total energy difference between the two isomeric binding sites of M'-T, Figure 6.2.

$$\mathbf{E_{stability} = E_L - E_M} \qquad \mathbf{(6.1)}$$

The quantities E_L and E_M denote the total energies of metal-trimer complexes (M'-T) where M' is ligated to the ligand (M'_L) and metal (M'_M) sites, respectively. $E_{stability}$ thus reflects the relative preference of M' for the M'_M site over M'_L site binding. In other words, if $E_{stability} < 0$, M' prefers to bind at the ligand site and vice versa for $E_{stability} > 0$. All calculated $E_{stability}$ values are collected in Table 6.1. The most stable site for Al, Au, Cu, Ni, Pt, Ru is the metal site, Table 6.1. For La, Ti, the preferred binding site is the ligand site of the gold(I)-pyrazolate trimer; $E_{stability}$ = -0.39 and -0.70 eV, respectively. Interestingly, Pd has equal stability at both M'_L and M'_M sites, which is evidenced by $E_{stability}$ = 0 eV.

6.3.1.1 Reorganization Energies Upon M' Coordination

Geometric distortion of the trimer (T) upon M' adsorption with respect to the original ground state geometry of the M'-free trimer is determined to give relaxation/reorganization (RO) energies $[E(T)_{RO}]$[42].

$$\mathbf{E(T)_{RO} = E(T)_{unrelaxed} - E(T)_{relaxed}} \tag{6.2}$$

The quantity $E(T)_{unrelaxed}$ is the energy of the unrelaxed Au trimer at the M'-adsorbed geometry, $E(T)_{relaxed}$ is the energy of the fully geometry optimized Au trimer in isolation. It is important to have low RO energies for better performance of a device, as large reorganization energies will retard efficient electron transfer in a device.[42]

All RO values are obtained from equation 6.2 and are very low, <0.1 eV (2 kcal/mol). Moreover, one expects an isolated metal atom to be more chemically reactive than a metal surface and thus the reorganization energies are likely to be even less for deposition of a cyclo-trimer on to an electrode metal surface. Hence, the simulations suggest that electron transfer will be not be impeded by large structural reorganization of the conductor, and should be efficient from the drain/source metals studied here to these p-type gold cyclo-trimer materials. One exception is calcium, which is a very low work function metal. Attempts to geometry optimize Ca-T adducts lead to degradation of the organic ligand (data not shown), which suggests that electron transfer and interface stability would be compromised between calcium and this p-type organometallic.

Table 6.1. Stability (eq. 6.1) and binding energies (eq. 6.3) for metal-trimer complexes. M and L indicate metal and ligand binding sites, respectively. Only energies of the most stable sites of metal binding are summarized here. Pd is equally stable at either sites and denoted with M/L.

M'	Spin State	$E_{stability}$ (eV)	Stable binding Site	Binding Energy (eV)
Al	2	0.41	M	-0.52
Au	2	0.32	M	-0.57
Cu	2	0.43	M	-0.63
La	2	-0.39	L	-0.73
Ni	3	0.46	M	-0.60
Pd (M/L)	1	0.00	M/L	-0.85/-0.85
Pt	3	0.28	M	-0.60
Ru	5	0.33	M	-0.65
Ti	3	-0.70	L	-0.46

6.3.1.2 M’ Binding Energies

The binding energy of the metal atom on the gold trimer is calculated as the difference in total energy between the optimized metal-trimer (M’-T) complex and the sum of energies of the isolated optimized trimer (T) and metal atom (M’). This energy is also called the metal adsorption energy.

$$\mathbf{E_{bind} = (E_{M'\text{-}T}) - (E_{M'} + E_{T})} \qquad \mathbf{(6.3)}$$

E_{bind} is the binding energy of metal atom on the Au trimer and $E_{M'\text{-}T}$, $E_{M'}$, E_T are the total energies of M’-trimer complexes, M’ atoms and Au trimer respectively. Examination of binding energy values (Table 6.1) reveals that Ti with -0.46 eV is the weakest binding and Pd with -0.85 eV is the strongest binding metal atom on the Au trimer. Also, it is interesting that Pd binds at both M'_L and M'_M sites with the same binding energy of -0.85 eV.

Interaction of electrode metals with an organometallic semiconductor during device fabrication may result in diffusion of metal atoms into the semiconductor network. In this context, properties that characterize the stability of the metal/semiconductor interaction such as binding energies (E_{bind}) are important to minimize impurity scattering within the device. The present simulations indicate strong binding, Table 6.2, of the electrode metal atoms to these p-type gold trimers and thus that they will form a stable interface with minimal diffusion.

6.3.2 Geometric Properties

For efficient performance of an electronic device, it is important for the different materials in the device to remain stable and be chemically compatible. Additionally, diffusion of one material to another, due to differences in chemical potential, is a common mechanism of failure in an electronic device[43-46]. One way to judge the stability of a chemical system is by comparing the geometric changes in the system upon a chemical interaction. Trinuclear gold pyrazolate trimer is a nearly planar molecule, with average intramolecular Au-Au distances ranging from 3.2 - 3.4 Å[45], which indicate the Au-Au interactions being in the aurophilic regime. Calculated Au-Au distances in the geometry optimized gold pyrazolate trimer studied here is 3.44 Å, in good agreement with the experimental estimates.

We have analyzed the bond distances and bond angles for the gold trimer and each metal (M')-trimer complex. Important bond distances are listed in Tables 6.2 and 6.3. The geometry of the Au trimer remains roughly unchanged for metals that are bound to the gold atoms(M'$_M$ site). For example, the intramolecular Au-Au distances in all M'-T complexes with M'$_M$ coordination did not change significantly (maximum difference = 0.03 Å or less than 1%) with respect to the parent structure cyclo-[Au(μ-Pz)]$_3$. The shortest M'-Au distance is seen for Ni (2.78 Å) while the longest is for Ru (3.07 Å), and roughly paralleling the size of the electrode metal atoms. Also, note from Table 6.2 that all three M'-Au distances are equivalent or nearly so, supporting the contention that metal binding occurs in a π-acid/base fashion as opposed to a π/Lewis fashion.

Table 6.2. Notable bond length changes for metal-trimer complexes at M'$_M$ site. The bond numbering is given according to Figure 6.2(a). 'σ' is the standard deviation

Bond(R) Type		Al	Au	Cu	Ni	Pd	Pt	Ru	σ
Au-M'$_M$	R(1-22)	2.87	3.00	2.78	2.78	2.89	2.97	3.07	0.11
Au-M'$_M$	R(2-22)	2.87	3.00	2.78	2.81	2.89	2.87	3.06	0.10
Au-M'$_M$	R(3-22)	2.87	3.00	2.78	2.81	2.89	2.87	3.06	0.10

Comparing our theoretical results for optimized M'-Au bond lengths with their respective covalent (Cov.) radii and experimental (Expt.) bond distance estimates (from the Cambridge Crystallographic Data Centre, (CCDC) database) [47], is revealing with respect to the nature of the M'-Au interaction, Table 6.3. The two coinage metals modeled – Au, Cu – bind to the M'$_M$ site at distances close to covalent bond estimates. On the other hand, earlier (Group 8 and 10) transition metals Ni, Pd, Pt, Ru bind at Au-M’ distances that are longer than covalent bond estimates, and hence lie toward the weaker van der Waals regime.

Table 6.3. Comparison of calculated bond distances with experimental bond distances and covalent radii. ‘r’ is the avg. bond length, ‘σ’ is the standard deviation and ‘n’ is the sample size from CCDC.[47]

Metal	R(Au-M’) (Å)	Sum of Cov. Radii (Å)	r(Au-M') (Å)	σ(Au-M') (Å)	n
	Calc.	Expt.	CCDC	CCDC	CCDC
Al	2.87	2.62	-	-	-
Au	3.00	2.88	2.94	0.19	3323
Cu	2.78	2.82	2.79	0.13	102
Ni	2.80	2.65	2.68	0.03	36
Pd	2.89	2.75	2.82	0.14	201
Pt	2.90	2.72	2.74	0.12	373
Ru	3.06	2.70	2.81	0.08	412

On the other hand, when metals are bound to the ligand (M’$_L$) site, the Au trimer structure changes more noticeably (Table 6.4), in comparison to the M’$_M$ binding site. Major differences in bond distances and angles can be seen on the ligand to which the metal (M’) is bound (Table 6.4).

Table 6.4. Notable bond length and bond angle changes for metal-trimer complexes at M’$_L$ site. The bond numbering is given according to Figure 6.2(b). ‘σ’ is the standard deviation.

Bond(R)/Angle(A) Type		Trimer	La	Pd	Ti	σ
M’-C3	R(22-9)		2.71	2.68	2.31	0.22
M’-C4	R(22-10)		2.71	2.68	2.31	0.22
M’-C9	R(22-25)		2.91	2.14	2.52	0.39
M’-N6	R(22-6)		2.45	3.34	2.07	0.65
M’-N5	R(22-5)		2.45	3.34	2.07	0.65
Au-Au	R(20-21)	3.42	3.50	3.47	3.51	0.03
N-C	R(5-9)	1.36	1.45	1.35	1.44	0.05
N-C	R(6-10)	1.35	1.45	1.35	1.44	0.05
N-N	R(5-6)	1.38	1.51	1.39	1.49	0.07
N-Au-N	A(2-21-6)	175.38	178.21	178.79	179.10	1.70
Au-N-C	A(9-5-20)	131.47	125.09	130.85	127.62	2.97
Au-N-C	A(10-6-21)	132.01	125.09	130.85	127.62	3.14

La and Ti metals cause an elongation of N-N, N-C bonds, N-Au-N bond angle and shrinkage of Au-N-C bond angles on the ligand to which La and Ti are bonded. The average N-N, N-C bonds and N-Au-N bond angle are elongated from 1.38 Å, 1.35 Å, and 175.4° to 1.50 Å, 1.44 Å, and 178.6°, respectively. The Au-N-C bond angle reduces from 131.7° to 126.4°. Also, the intramolecular Au-Au distance increases by 0.08 Å for the gold atoms that are bonded to the ligand to which M' is π-coordinated. Both of these electropositive (low work function) metals are closer to the N atoms of the pyrazolate ligand than C atoms, which is consistent with the greater electronegativity of N versus C.

Palladium binding to an L site behaves differently from La and Ti. No major change in the trimer geometry is seen when Pd binds to the ligand except for slight elongation of intramolecular Au-Au distance from 3.42 Å to 3.47 Å for the gold atoms that are bonded to the pyrazolate to which Pd is bound. Also, Pd lies close to the tip carbon (C9 in Figure 6.2(b)) of the 5 membered pyrazolate ligand (η^1-C coordination) in contrast to Ti and La, which are η^2-N,N.

Overall, examination of all geometric parameters of Au trimer and metal (M')-trimer complex indicates that when M' binds to the metal (M'_M) site no inordinate change in trimer structure is seen. On the contrary, M' binding to the ligand (M'_L) site causes bending of the pyrazolate thus leading to considerable geometric distortion of Au trimer in contrast to its prototype. This is however not seen for the ligand bound Pd-trimer complex. In light of the overall low geometric reorganization, and strong interactions between the metal atoms and the trimer, the possibility of diffusion of metal atoms through the interfaces upon differences in chemical potential would be less and this phenomenon is important for a stable device performance[43-45].

6.3.3 Electronic Properties

For investigation of the electronic structures of metal-trimer complexes we plotted the HOMO-LUMO energies and the atomic density of states (DOS) of all the complexes have been analyzed. The HOMO-LUMO gap for the gold trimer is about 5.6 eV. Although this gap is large (and likely overestimated by these hybrid DFT calculations), electron donating substituents on the pyrazolate ligand reduce the HOMO-LUMO gap and make the trimer a conductor[16]. Here, our primary concern is the change in electronic properties of the prototype structure of cyclo-[Au(μ-Pz)]$_3$ upon the coordination of typical electrode metals, M'.

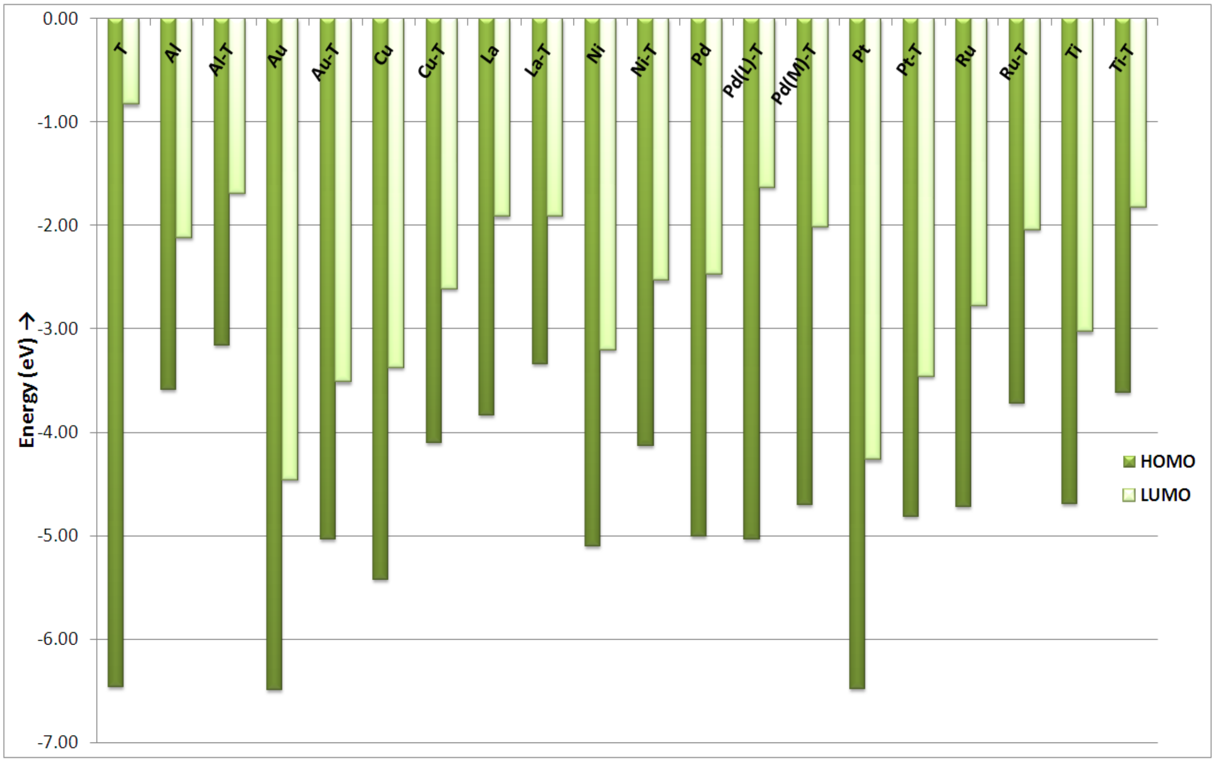

Figure 6.3. HOMO-LUMO values for Au trimer (T), individual metals (M') and stable metal-trimer complexes (M'-T) in eV.

Figure 6.3 presents the HOMO and LUMO values of all the stable metal-trimer complexes, metals and trimer. From the figure it is clear that that the HOMO-LUMO gap decreases for all the M'-T complexes in contrast to the T alone. The largest and smallest HOMO-

LUMO gaps of 3.4 eV and 1.5 eV are calculated for Pd(M'$_L$)-T and Pt-T complexes, respectively. The reduction in HOMO-LUMO gap is a result of both lowering the LUMO energy and raising the HOMO energy. As such, this suggests extensive Au-M' hybridization (see also corroborating DOS data below). Hence, the calculations predict that deposition of the trimer, T, onto an electrode metal M' will maintain if not improve conductivity properties across the electrode/conductor interface.

We also examined other electronic properties, viz charge transfer (CT) and dipole moment data for the Au trimer versus the M'-T complexes. CT was assessed using both Mulliken and Natural Population Analysis. Examination of all CT and dipole moment data did not reveal any obvious trend in terms of the binding preference of the electrode metal, M', to either the metal or ligand sites of the gold trimer.

The orbital contributions or partial density of states (pDOS) of the trimer by itself and metal (M') projections to the total DOS (tDOS) of metal-trimer complexes are shown in Figure 6.4 and Figure 6.5 respectively. The DOS results are obtained from the Gaussian expansion scheme of discrete energy levels ε_i by the AOMix code[37,38].

$$\mathbf{tDOS\ (E) = \Sigma_i\ \delta(E\text{-}\varepsilon_i)} \qquad \mathbf{(6.4)}$$

E is the energy at each state, ε_i is the one electron energy level and δ is the gaussian expansion function. Partial densities of states (pDOS) for fragments (group of atoms or orbitals) are determined using the Mulliken population analysis (MPA) scheme.

$$\mathbf{pDOS\ (E) = \Sigma_i\ C_{A,i}\ \delta(E\text{-}\varepsilon_i)} \qquad \mathbf{(6.5)}$$

$C_{A,i}$ is the one-electron character of any fragment A at energy ε_i. The DOS plots gives an indication of which electrons hybridize in the metal trimer interaction and also helps in understanding the conduction or flow of charge near the metal-trimer interface.

Figure 6.4 shows the DOS plot of cyclo-[Au(μ-Pz)]$_3$ along with projections for the gold 6s, 6p, 5d and ligand orbitals. The HOMO and LUMO are at -6.47 eV and -0.83 eV, respectively, yielding a 5.64 eV HOMO-LUMO gap. The pDOS projections clearly indicate that pyrazolate ligands (blue line in Figure 6.4) are major contributors in both the HOMO (valence) and LUMO (conduction) orbitals. Also, the valence band has considerable gold 5d orbital character (red line in Figure 6.4) with some s and p character. The above interpretation is consistent with previous studies of similar coinage metal materials[17].

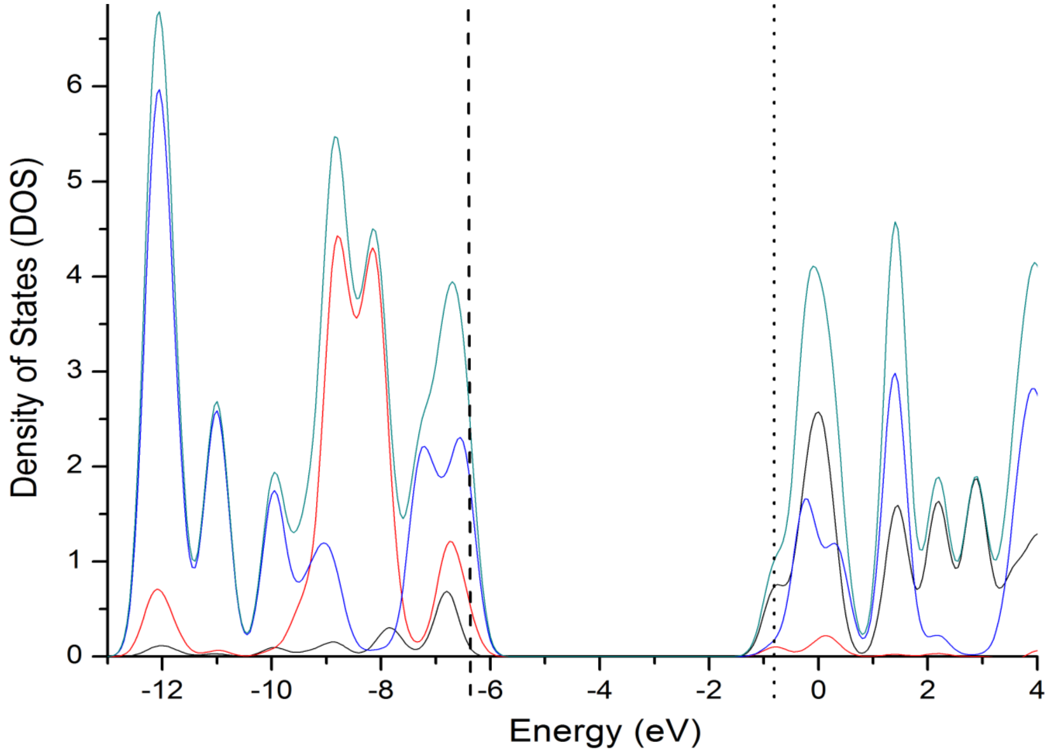

Figure 6.4. Projected DOS plot with contributions from gold s+p, d orbitals and ligand orbitals colored in black, red and blue, respectively. The total DOS is colored in green.

Figure 6.5 shows the DOS plots of all M'-T complexes studied here. For all M'-T complexes the HOMO and LUMO energies rise (become more weakly bound) and fall, respectively, with respect to those of isolated cyclo-[Au(μ-Pz)]$_3$. This phenomenon highlights the hybridization of the metal orbitals with those of gold. The degree of hybridization however varies for different metal atoms. Among all the DOS plots for the Pd-T complexes are distinct. The orbital mixing or hybridization of metal atoms with trimer based orbitals is less for Pd at both the gold and pyrazolate binding sites, which can be seen from the wide HOMO-LUMO gap and pDOS plots of Pd(M'_L)-T and Pd (M'_M)-T. In either case, very little or no contribution from the Pd atom (black line in the graph, Figure 6.5) is seen in DOS plots. On the other hand, all the remaining metal atoms show considerable mixing of M' orbitals with gold trimer, where the atomic contribution of the electrode metals is clearly seen in the respective DOS plots (Figure 6.5).

Examining individual DOS plots of M'-T complexes gives an overview of how different metals contribute to tDOS. We focus our discussion mostly to the frontier/Fermi level orbitals in the vicinity of the HOMO and LUMO (ca. -8 to 1 eV energy), which would be responsible for most chemical reactions and charge transport. The pDOS plot of Al-T complex shows equal contributions from Al and trimer to the HOMO, while the trimer orbitals dominate the LUMO. In the Au-T complex, the contribution of the bound gold atom is roughly the same in the valence and conduction bands, but remains less than the contribution of orbitals from the trimer. The Cu character in Cu-T complex is similar to that of gold in Au-T. The pDOS plots show considerable orbital mixing at the top of the valence band, but the Cu character is less in the conduction band, Figure 6.5.

For the La-T complex (recall La binds to the L site), the La contribution to the HOMO is prominent but orbitals below the HOMO have very low or no contribution from La. Unlike the coinage metals just discussed, the La character is high in the LUMO and the orbitals beyond. The DOS plot of the Ti-T complex (recall that Ti binds to the L site), Figure 6.5, is similar to that of La-T complex, where the Ti character is less in orbitals below the HOMO and more in orbitals above the LUMO. The trimer contribution to HOMO and LUMO orbitals is negligible indicating that HOMO and LUMO orbitals in the Ti-T complex are solely from the Ti metal atom.

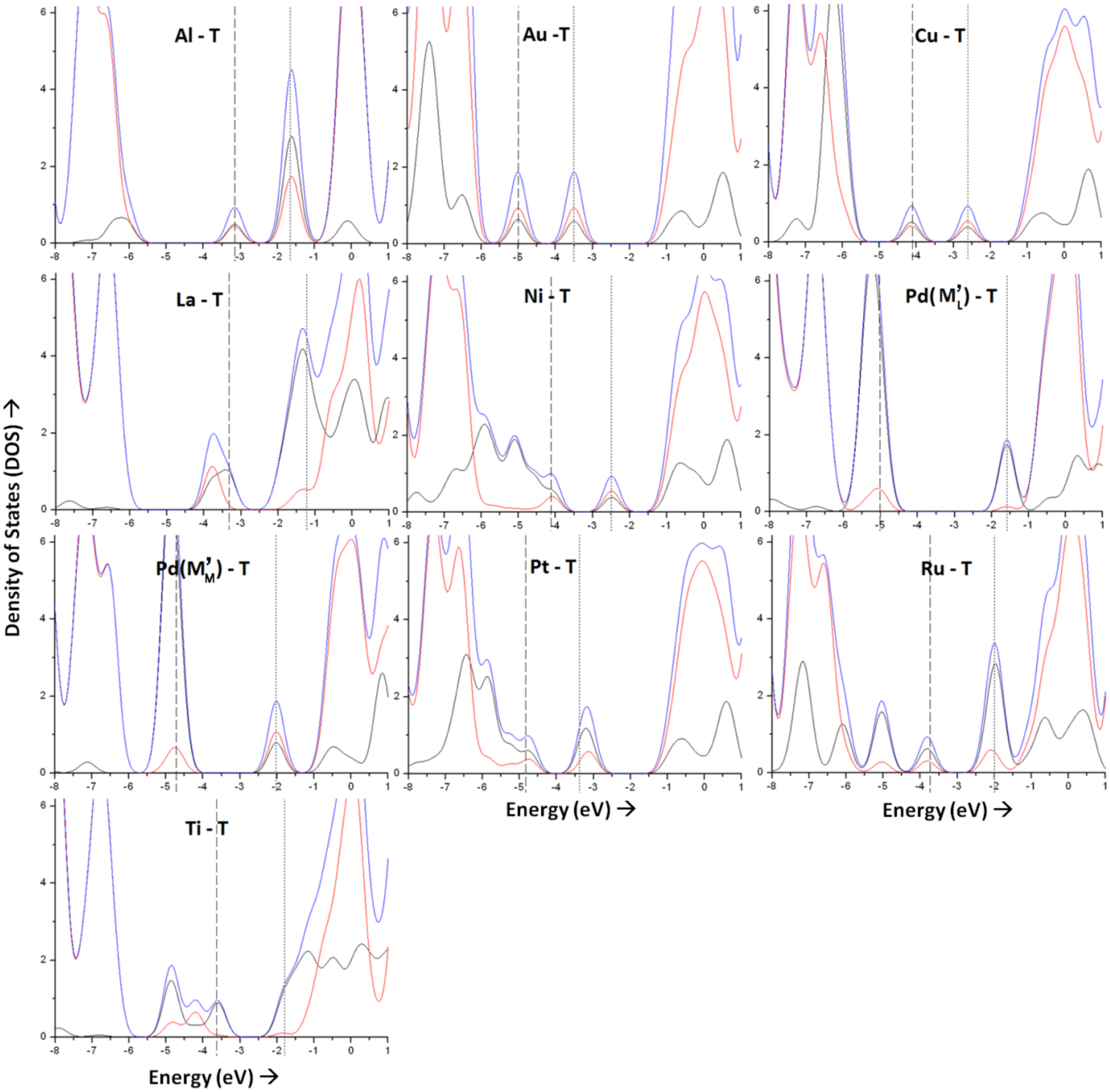

Figure 6.5. B3LYP DOS plots of metal-trimer complexes with metal atoms M' = Al, Au, Cu, La, Ni, Pd, Pt, Ru, Ti. DOS plots for all the metals are limited to their stable sites, either the ligand (M’L) or metal (M’M) site. Two DOS plots are plotted for Pd which is equally stable at both the sites and respective plots are named with M’L/M’M in parenthesis. The tDOS is colored blue, pDOS of metal atom (M') and trimer (T) are colored black and red respectively. The dashed lines mark the HOMOs and the dotted lines LUMOs for each complex.

The pDOS plots of the Ni-T complex show ample mixing of metal atom and trimer orbitals, Figure 6.5, within the range considered which is apparent from the Ni character in the DOS. Pt-T and Ru-T complexes are similar to Ni-T complexes where notable mixing of orbitals is seen and there is metal (M’) atom contribution in both the HOMO and LUMO.

Analyzing the binding preferences of metal atoms on the trimer, electropositive transition metals La, Ti prefer the anionic M'_L site in contrast to electronegative Au, Cu, Ni, Pt, and Ru which prefer the cationic M'_M site. The reason for equal gold/ligand binding preferences of the Pd atom is not understood, but may be related to its different frontier orbital composition, which shows minimal hybridization with trimer orbitals. Al which is the only main group element in our list binds to the M'_M site.

6.4 Summary and Conclusions

Molecular DFT calculations are performed on cyclo-[Au(μ-Pz)]$_3$ trimer (T), a model p-type organometallic, with prototypical electrode metal atoms (M’). Metal (M'_M) and ligand (M'_L) sites of the gold trimer are investigated as the possible sites of deposition for the metal atoms. Metal atom-trimer (M’-T) interactions for M’= Al, Au, Cu, La, Ni, Pd, Pt, Ru and Ni are presented in this report. Metal binding characteristics, geometric and electronic properties were analyzed for M’-T complexes. It was found that Al, Au, Cu, Ni, Pt and Ru favor coordination to the metal (i.e., gold) site of the trimer; low work function metals like La and Ti favor the ligand site while Pd has equal stability at both the M'_L and M'_M sites of the trimer. Among all the metal atoms, Ti is the weakest binding and Pd is the strongest binding to the Au trimer at their respective stable coordination sites. Changes in geometry of the trimer upon deposition of metal atom are negligible for M'_M-T complexes, but more change is seen for M'_L-T complexes. Examination of the electronic structure of all M’-T complexes reveal a considerable hybridization for all M’ and trimer orbitals around the HOMO and LUMO. However, there is an exception for the Pd-T complex, where negligible Pd contribution is observed around the HOMO-LUMO.

In conclusion, modeling the effect of electrode metal atom deposition onto a p-type gold trimer is important to understand the impact of metal-trimer chemistry upon the electronic properties of cyclo-Au(μ-L)]$_3$[7,11,12]. Deposition of metal source and drain electrodes on the organometallic semiconductor during device fabrication is critical for stable device performance. Metal binding characteristics, as well as geometric and electronic properties, play an important role in minimizing impurity scattering within the device. Efficient charge transport across the metal-trimer interface is also critical as researchers seek to go from molecular level control of properties to real-world device fabrication perspectives. The present simulations indicate minimal reorganization, both in terms of the energies and geometries, upon metal/trimer interaction. The substantial binding energies of the electrode metal atoms to the p-type trimer, significant hybridization of the metal and trimer orbitals near the Fermi level, and large changes in the HOMO-LUMO gaps upon metal deposition all suggest a stable interface for these metal-based MOFETs, with efficient charge transport, for both high and low work function metals.

6.5 Chapter References

(1) Vaughan, L. G. *J. Am. Chem. Soc.* **1970***, 92*, 730-731.

(2) Parks, J. E.; Balch, A. L. *J. Organomet. Chem.* **1974***, 71*, 453-463.

(3) Minghetti, G.; Bonati, F. *Inorg. Chem.* **1974***, 13*, 1600-1602.

(4) Bovio, B.; Bonati, F.; Banditelli, G. *Inorg. Chim. Acta* **1984***, 87*, 25-33.

(5) Bovio, B.; Calogero, S.; Wagner, F. E.; Burini, A.; Pietroni, B. R. *J. Organomet. Chem.* **1994***, 470*, 275-283.

(6) Balch, A. L.; Olmstead, M. M.; Vickery, J. C. *Inorg. Chem.* **1999***, 38*, 3494-3499.

(7) Omary, M. A.; Rawashdeh-Omary, M.; Gonser, M. W. A.; Elbjeirami, O.; Grimes, T.; Cundari, T. R.; Diyabalanage, H. V. K.; Gamage, C. S. P.; Dias, H. V. R. *Inorg. Chem.* **2005***, 44*, 8200-8210.

(8) Burini, A.; Mohamed, A. A.; Fackler, J. P. *Comments Inorg. Chem.* **2003***, 24*, 253.

(9) Pyykkö, P.; Zhao, Y. *Angew. Chem. Int. Edn.* **1991***, 30*, 604-605.

(10) Pyykkö, P.; Li, J.; Runeberg, N. *Chem. Phys. Lett.* **1994***, 218*, 133-138.

(11) Dias, H. V. R.; Diyabalanage, H. V. K.; Rawashdeh-Omary, M.; Franzman, M. A.; Omary, M. A. *J. Am. Chem. Soc.* **2003***, 125*, 12072-12073.

(12) Dias, H. V. R.; Diyabalanage, H. V. K.; Eldabaja, M. G.; Elbjeirami, O.; Rawashdeh-Omary, M.; Omary, M. A. *J. Am. Chem. Soc.* **2005***, 127*, 7489-7501.

(13) D'AndradeB. W.; Forrest, S. R. *Adv Mater* **2004***, 16*, 1585-1595.

(14) Caseri, W.R.; Chanzy, H.D.; Feldman, K.; Fontana, M.; Smith, P.; Tervoort, T.A.; Goossens, J.G.P.; Meijer, E.W.; Schenning, A.P.H.J.; Dolbnya, I.P.; Debije, M.G.; de Haas, M.P.; Warman, J.M.; van de Craats, A.M.; Friend, R.H.; Sirringhaus, H.; Stutzmann, N. *Adv Mater* **2003***, 15*, 125-129.

(15) Torralba, M. C.; Ovejero, P.; Mayoral, M. J.; Cano, M.; Campo, J.; Heras, J.; Pinilla, E.; Torres, M. R. *Helv. Chim. Acta* **2004***, 87*, 250-263.

(16) Tekarli, S. M.; Cundari, T. R.; Omary, M. A. *J. Am. Chem. Soc.* **2008***, 130*, 1669-1675.

(17) Chilukuri, B.; Cundari, T. R.; Omary, M. A.; Gnade, B. In *In Modeling silver and gold complexes for next generation electronic materials;* Abstracts of Papers, INOR 363; poster presentation to the ACS Division of Inorganic Chemistry,239th ACS National Meeting,

San Francisco, CA, Mar 21–25, **2010**; American Chemical Society: Washington, DC., **2010**.

(18) Kim, S. J.; Kang, S. H.; Park, K.; Kim, H.; Zin, W.; Choi, M.; Kim, K. *Chem. Mater.* **1998**, *10*, 1889-1893.

(19) Zaumseil, J.; Sirringhaus, H. *Chem. Rev.* **2007**, *107*, 1296-1323.

(20) Campbell, I. H.; Rubin, S.; Zawodzinski, T. A.; Kress, J. D.; Martin, R. L.; Smith, D. L.; Barashkov, N. N.; Ferraris, J. P. *Phys. Rev. B* **1996**, *54*, R14321.

(21) Zaumseil, J.; Baldwin, K. W.; Rogers, J. A. *J. Appl. Phys.* **2003**, *93*, 6117-6124.

(22) Frisch, M. J.; et al. Gaussian 09, Revision A.1, Gaussian, Inc., Wallingford CT **2009**.

(23) Stephens, P. J.; Devlin, F. J.; Chabalowski, C. F.; Frisch, M. J. *J. Phys. Chem.* **1994**, *98*, 11623-11627.

(24) Becke, A. D. *Phys. Rev. A* **1988**, *38*, 3098.

(25) Lee, C.; Yang, W.; Parr, R. G. *Phys. Rev. B* **1988**, *37*, 785.

(26) Stevens, W. J.; Krauss, M.; Basch, H.; Jasien, P. G. *Can. J. Chem.* **1992**, *70*, 612.

(27) Stevens, W. J.; Basch, H.; Krauss, M. *J. Chem. Phys.* **1984**, *81*, 6026-6033.

(28) Cundari, T. R.; Stevens, W. J. *J. Chem. Phys.* **1993**, *98*, 5555-5565.

(29) Grimes, T.; Omary, M. A.; Dias, H. V. R.; Cundari, T. R. *The J. Phys. Chem. A* **2006**, *110*, 5823-5830.

(30) Becke, A. D. *J. Chem. Phys.* **1996**, *98*, 5648–5642.

(31) Perdew, J. P.; Wang, Y. *Phys. Rev. B* **1992**, *45*, 13244–13249.

(32) Buhl, M.; Kabrede, H. *J. Chem. Theory Comput.* **2006**, *2*, 1282–1290.

(33) Waller, M. P.; Braun, H.; Hojdis, N.; Buhl, M. *J. Chem. Theory Comput.* **2007**, *3*, 2234-2242.

(34) Buhl, M.; Reimann, C.; Pantazis, D. A.; Bredow, T.; Neese, F. *J. Chem. Theory Comput.* **2008**, *4*, 1449-1459.

(35) Foster, J. P.; Weinhold, F. *J. Am. Chem. Soc.* **1980**, *102*, 7211-7218.

(36) Reed, A. E.; Weinstock, R. B.; Weinhold, F. *J. Chem. Phys.* **1985**, *83*, 735-746.

(37) Gorelsky, S. I. AOMix program, http://www.sg-chem.net/ .

(38) Gorelsky, S. I.; Lever, A. B. P. *J. Organomet. Chem.* **2001**, *635*, 187-196.

(39) Burini, A.; Bravi, R.; Fackler, , John P.; Galassi, R.; Grant, T. A.; Omary, M. A.; Pietroni, B. R.; Staples, R. J. *Inorg. Chem.* **2000**, *39*, 3158-3165.

(40) Omary, M. A. *et al.*, Abstracts of Papers, INOR-119; presentation to the ACS Division of Inorganic Chemistry, 236th ACS National Meeting, Philadelphia, PA, Aug 17-21, **2008**; American Chemical Society: Washington, DC., **2010**.

(41) Gnade, B. (University of Texas, Dallas); Omary, M. A (University of North Texas) - private communication.

(42) Marcus, R. A. *Rev. Mod. Phys.* **1993**, *65*, 599.

(43) Aziz, H.; Popovic, Z. D.; Hu, N.; Hor, A.; Xu, G. *Science* **1999**, *283*, 1900-1902.

(44) Chua, S.; Ke, L.; Kumar, R. S.; Zhang, K. *Appl. Phys. Lett.* **2002**, *81*, 1119-1121.

(45) Cumpston, B. H.; Jensen, K. F. *Appl. Phys. Lett.* **1996**, *69*, 3941-3943.

(46) Diao, L.; Frisbie, C. D.; Schroepfer, D. D.; Ruden, P. P. *J. Appl. Phys.* **2007**, *101*, 014510-8.

(47) Allen, F., *Acta Cryst.* **2002**, *58*, 380-388.

CHAPTER 7

SURFACE INTERACTIONS OF AU(I) CYCLO-TRIMER WITH AU(111) AND AL(111) SURFACES: A COMPUTATIONAL STUDY

7.1 Introduction

Semiconductor and metal electrode interfaces are common entities in many organic devices[1] such as organic light emitting diodes (OLEDs)[2], organic field effect transistors (OFETs)[3], and organic photovoltaics (OPVs)[4]. These organic devices are attracting enormous attention due to their promising properties, low-cost processing and flexibility[2-4]. However, due to some limitations regarding the mobility, performance and stability of organic electronic devices, metal-organic materials are being considered because of the presence of additional electronic and chemical properties obtained such as metal-metal, metal-π, and π-π interactions. A variety of metal-organic materials have led to devices such as "hot-water proof" field effect transistors[5], superconductors[6], and white electrophosphorescence in OLEDs[7].

Metal-organic cyclic trinuclear complexes, cyclo-$[M(\mu\text{-}L)]_3$ with coinage metals (M = Cu, Ag, Au) have interesting chemical and material properties[8-9]. The d^{10} metal ions (M^I) of the cyclo-trimers are bridged by monoanionic bidentate ligands (L) with C-C, C-N and N-N ligation. These coinage metal complexes often display metallophilicity[10] and metalloaromaticity, as well as other interesting properties[8-11]. Cyclo-$[M(\mu\text{-}L)]_3$ complexes exhibit excellent, highly tunable π-acid/base molecular properties, easily surpassing pentacene and perfluoropentacene, making them good p-/n-type semiconductor candidates[12]. Among the various cyclo-trimers studied, gold pyrazolate (Pz) trimers, cyclo-$[Au(\mu\text{-}Pz)]_3$ (Figure 7.1), exhibit good electron-donating

---

* This entire chapter is reproduced from [Chilukuri, B.; Cundari, T. R. "Surface interactions of Au(I) cyclo-trimer with Au(111) and Al(111) surfaces: A computational study" *Surface Science* **2012**, vol. *606*, pp 1100–1107.], with permission from Elsevier.

behavior[12-14] making them a good choice as semiconducting material for metal-organic electronic devices.

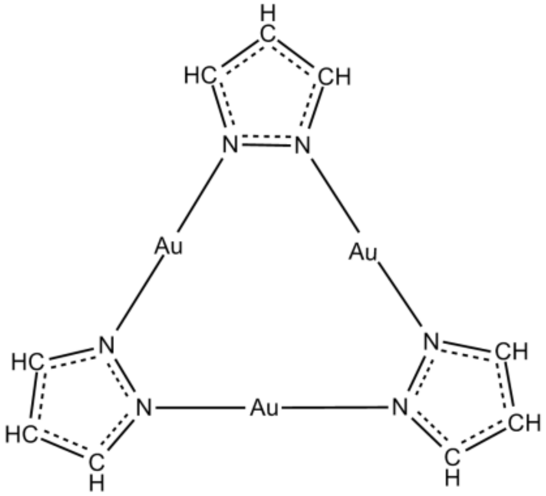

Figure 7.1. Molecular structure of cyclo-[Au(μ-Pz)]3 (Pz = Pyrazolate) trimer (T).

In organic electronic devices, the interface between semiconductors and metal electrodes (Figure 7.2) has been studied extensively mainly because energy level alignment at the organic/metal interfaces govern the efficiency of the carrier injection, which ultimately determines the performance of the devices[15]. Moreover, these interfaces are common components in devices such as OFETs, OLEDs and OPVs. Numerous studies, both experimental[16] and theoretical[17] have been performed to understand the interfacial properties of organic molecules/semiconductors and metal electrodes. Studies revealed that organic semiconductor interfaces ignore the vacuum level alignment rule otherwise known as the Schottky-Mott limit for inorganic semiconductor interfaces[18]. The change in work functions and energy level alignments at the electrode-semiconductor interfaces are attributed to a variety of parameters: the molecule-metal distance, vacuum level shift[19] and dipole formation at the interface[16-20]. It was also reported that these work function changes are not consistent for a given metal, but are typical to the type of molecule interacting with the metal electrode[18]. Earlier studies on interfaces ignored the dipole barriers, leading to errors in determining the electronic properties at interfaces[21].

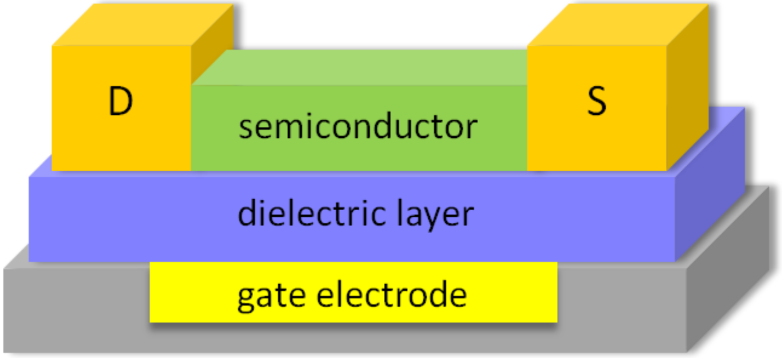

Figure 7.2. Typical layout of an OFET. D and S represent source and drain electrodes, respectively.

Similar studies on interfacial electronic properties are not as prevalent in metal-organic electronic devices as in organic devices[16-17]. Our earlier study[14] of the interaction of electrode metal atoms with cyclo-[Au(μ-Pz)]$_3$ has demonstrated that at the molecular level there is minimal reorganization both in terms of the energies and geometries, substantial binding energies and significant hybridization of the metal and trimer orbitals near the Fermi level upon metal/trimer interaction. In this report, we present a DFT study of interface interactions and electronic properties of cyclo-[Au(μ-Pz)]$_3$ trimer (denoted as T) with Au(111) and Al(111) metal surfaces. We also compare the interfacial interactions of the trimer molecule with high work function Au(111) and low work function Al(111) metals.

7.2 Methodology

7.2.1 Starting Geometries

In order to model the interactions at electrode-trimer interfaces, unit cells are built for Au(111), Al(111) and the trimer (T) separately and these are used to build an interface between the trimer and metal slabs (M’). The unit cells of the trimer and metal slabs are fully relaxed before building interfaces between them. In this section we describe the starting geometries of metal slabs, the trimer and interfaces between them. Limitations for building their respective interfaces are also discussed.

7.2.1.1 Primary lattices for Au and Al structures

Face centered cubic (fcc) lattice structures of gold and aluminum obtained from experiment[22] are used as starting structures. The fcc lattices are used as they represent ground state structures for gold and aluminum. These lattices are fully relaxed (details in Computational Methods) and the optimized lattice constants agree closely with the experiment, Table 7.1. Calculated fcc-Au and fcc-Al structures are now used to build Au(111) and Al(111) slabs.

Table 7.1. Lattice constants of calculated and experimental structures for fcc-Au and fcc-Al solids.

Lattice	Calculated	Experimental
fcc-Au	4.079	4.078
fcc-Al	4.048	4.049

Table 7.2. Lattice parameters of Au/Al(111) metal slabs, Au/Al(111)-T interface systems and isolated gold pyrazolate trimer (T).

System	a (Å)	b (Å)	c (Å)	α (^{o})	β (^{o})	γ (^{o})
Au(111) and Au(111)/T	14.26	14.26	45.02	90	90	120
Al(111) and Al(111)/T	14.74	14.74	45.02	90	90	120
Isolated trimer	24.70	24.70	15.00	90	90	120

7.2.1.2 Au(111) and Al(111) slabs (M')

We used the repeated slab approach to build Au(111) and Al(111) surfaces. Six layers of gold and aluminum are used to represent the Au(111) and Al(111) surfaces respectively. The

(111) surfaces are built by cleaving the fully optimized fcc lattices of gold and aluminum along the (111) Miller plane using the software MedeA[23]. The primary unit cells (both hexagonal) of these (111) surfaces are now repeated 5×5×3 for Au(111) and 5×5×2 for Al(111) along the a, b, c directions respectively to obtain super cells with lattice parameters listed in Table 7.2. The c-axis of both Au(111) and Al(111) unit cells was made to be 45.02 Å leaving a vacuum gap of 33 Å, since the thickness of both the metal slabs is ~ 12 Å. The surface reconstruction[24] of Au(111) and Al(111) surfaces is not considered in the present study.

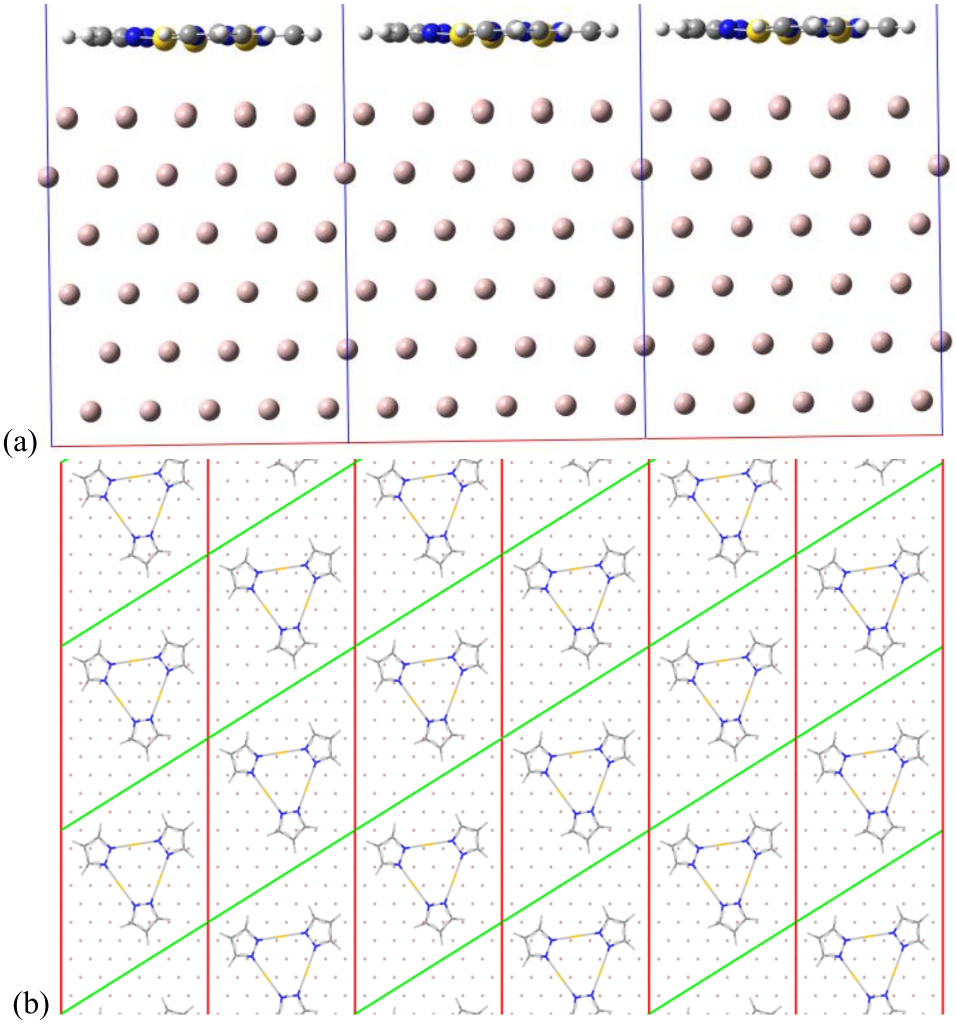

Figure 7.3. Starting geometries of metal(111)-trimer interface systems. The red, green and blue lines represent the *a*, *b*, *c* axes of the unit cell respectively. (a) Side view of the interface unit cell along the *b*-direction. (b) Top view of the interface unit cell along the *c*-direction.

7.2.1.3 Cyclo-[Au(μ-Pz)]$_3$ trimer (T)

A unit cell of isolated cyclo-[Au(μ-Pz)]$_3$ trimer was built with one molecule of the trimer inside the lattice, Table 7.2. The trimer is positioned at the center of the periodically repeated super cell. The choice of unit cell parameters for T in Table 7.2 was made to avoid any interactions of the trimer with another trimer in the neighboring unit cell, thus making the gold pyrazolate trimer act as a single molecule.

7.2.1.4 Au(111)-T and Al(111)-T interfaces

Fully relaxed geometries of metal slabs (M') and the trimer (T) are used to build Au(111)-T and Al(111)-T interfaces. To model the trimer monolayer coverage, each unit cell of the metal(111) slab is made (using Material Studio[25]) to accommodate one cyclo-[Au(μ-Pz)]$_3$ trimer molecule (Figure 7.3) with consistent thickness of the layers. Due to lack of experimental data on lattice parameters of the trimer monolayer on metal surfaces, we chose to adopt the corresponding metal (111) slab parameters for Au(111)-T and Al(111)-T interfaces respectively, Table 7.2. This assumption was made because it would be very difficult and impractical to model two sets of non-commensurate lattice parameters in a DFT calculation under periodic boundary conditions. Also, the trimer monolayer was made to deposit flat on the metal(111) slabs rather than in a vertical or angular fashion. This choice was made by considering the crystal structures of cyclo-[M(μ-Pz)]$_3$ complexes[13-26], our previous investigation[14] of the interaction of electrode metal atoms with cyclo-[Au(μ-Pz)]$_3$ trimer, experimental literature[27], and preliminary device data[28] for thermal deposition or solution casting of thin films of d^{10} trimers on various metal cathodes. However, we caution that the alignment height, direction and (non)planarity of the trimer adsorption on the metal surface may not correspond to the absolute global minimum structure, but should give important information on the adsorption interaction. Furthermore, since the unit cell parameters of the metal(111) slabs are adopted for the metal-trimer interface simulation, the vacuum gap between the trimer molecule and the next metal slab along the c-axis is then larger than 30 Å.

7.2.2 Computational Methods

All calculations are performed using plane-wave density functional theory (PW-DFT) within the projector augmented wave (PAW)[29] method to describe the core electrons and valence-core interactions. All simulations are performed using the VASP[30] code. The generalized gradient approximation (GGA) exchange-correlation functional of Perdew, Burke and Ernzerhof (PBE)[31] was employed. A spin polarized approach has been utilized for all calculations to check the presence of any polarization effects.

For all slab calculations, which include Au(111)-T, Al(111)-T, Au(111), Al(111), T_{Au} and T_{Al}, (T_{Au} and T_{Al} represent isolated trimer monolayers where the trimer molecules are maintained in their corresponding optimized adsorption geometries for Au(111)-T and Al(111)-T slabs, respectively), the electronic wave functions are sampled on a 3×3×1 k-point mesh in the irreducible Brillouin zone (BZ) using the Monkhorst and Pack (MP) method[32]. The cut-off energies of the wave functions used for Au(111)-T/Au(111)/T_{Au} and Al(111)-T/Al(111)/T_{Al} systems are 299.33 and 240.30 eV, respectively. Methfessel-Paxton smearing was used to set the partial occupancies for each wave function with a smearing width of 0.2 eV.

Calculations on isolated gold pyrazolate trimer (T) and primary fcc-Au/Al lattices are also carried out at the same level of theory but with different energy cut-offs and k-point meshes. For the isolated trimer, two optimizations with energy cut-offs of 299.33 and 240.30 eV with only one gamma point (1×1×1 k-point using MP method) are performed separately. Two different energy cut-offs are used to maintain consistency with metal slab calculations on

Au(111) and Al(111) surfaces performed earlier. For primary fcc lattice calculations on Au and Al, energy cut-offs of 299.33 and 240.30 eV, respectively, with a k-point mesh of 4×4×4 (MP method) for both metals, are used for the optimization.

7.3 Results and Discussion

7.3.1 Optimized Geometries

7.3.1.1 Au(111) and Al(111) slabs (M')

Six-layered gold and aluminum (111) slabs built from their respective fcc lattices are fully relaxed at the aforementioned level of theory. Upon relaxation, the surface structures of both Au(111) and Al(111) slabs are absolutely flat with intra-layer (along the a and b axes of the unit cell) Au-Au and Al-Al bond lengths of 2.949 and 2.852 Å, respectively. The inter-layer (along the c-axis of the unit cell) separation was found to be 2.413 Å and 2.442 Å for Au(111) and Al(111) surfaces, respectively. Work functions (Φ) of clean metal surfaces are calculated as the energy difference between the Fermi energy (E_f) of the surface and the electrostatic potential energy of an electron in the vacuum region at the distance where the potential energy has reached its asymptotic value. The calculated work function values for Au(111) and Al(111) are Φ_{Au} = 5.16 eV and Φ_{Al} = 4.01 eV respectively. These values are only lower than the experimental[33] work functions of Au and Al (111) surfaces by approximately 0.2 eV.

7.3.1.2 Cyclo-$[Au(\mu\text{-}Pz)]_3$ trimer (T)

Upon complete relaxation of the isolated gold pyrazolate trimer inside the unit cell, the trimer is planar and lies in the middle of the lattice. The intra-trimer aurophilic Au--Au bonds are found to be 3.40 Å, which closely agrees with our previous molecular study[14] and experimental data[13]. The sum of bond angles for each atom in the optimized trimer (Figure 7.4) is nearly 360°, indicating that the trimer is almost perfectly flat.

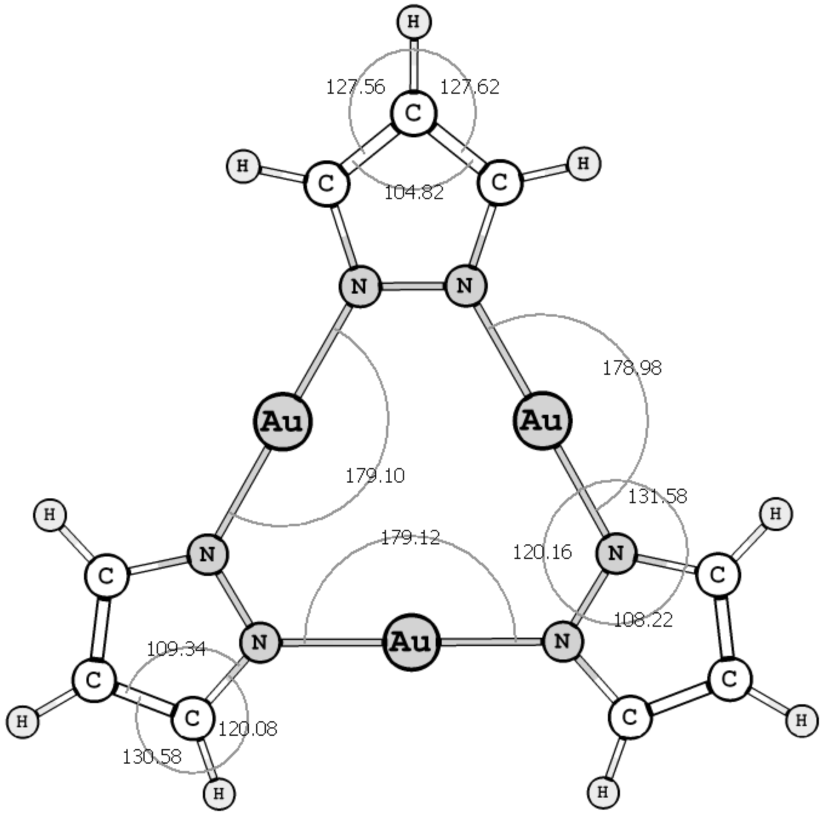

Figure 7.4. Optimized structure of isolated cyclo-[Au(μ-Pz)]3 trimer with different bond angles. The unit cell is omitted for clarity.

7.3.1.3 Au(111)-T and Al(111)-T interfaces

Relaxation of Au(111)-T and Al(111)-T interface systems are carried out in two steps. Firstly, the trimer monolayer is relaxed with a frozen metal surface. Secondly, the relaxed geometry from the previous step was used to initiate a complete structural relaxation of the M'-T system. Upon geometry optimization, the cyclo-[Au(μ-Pz)]$_3$ trimer adsorbs on the Au(111) surface in a 'concave up' shape (see bottom left in Figure 7.5) where the three gold atoms of the trimer are bound to the Au(111) surface with weak Au-Au bond lengths of 3.01, 3.03 and 3.11 Å, respectively- all easily within the aurophilic bond regime[10]. In the Au(111)-T interface system, the three pyrazolate rings of the trimer are bent away from the Au(111) surface slightly above the plane of the three trimer gold atoms (see left bottom in Figure 7.5). This can be seen from the shrink in the Au-N-C bond angles from 131.35 ± 0.15° for the isolated gold pyrazolate trimer to 130.00 ± 0.15° in the Au(111)-T interface system. The bending of the trimer molecular plane is possibly due to a weaker interaction of the pyrazolate ring with the Au(111) surface than the trimer gold atoms. In the Al(111)-T system, the gold pyrazolate trimer adsorbs 'flat' on the Al(111) surface (see right bottom in Figure 7.5) where three gold atoms of the trimer are binding to the Al(111) surface within the van der Waals regime[34] with Au-Al bond lengths of 3.09, 3.14 and 3.27 Å, respectively. The three pyrazolate rings of the trimer lay flat in the same plane as the three trimer gold atoms, in contrast to Au(111)-T system where they were bent. This is likely due to a weaker Al-Au interaction causing the trimer as a whole to remain flat on the Al(111) surface.

7.3.2 Adsorption Energy

The adsorption energy (E_{ads}) of the trimer on the metal surfaces is calculated as the difference in total energy between the optimized metal slab-trimer (M'-T) interface and the sum of energies of the isolated optimized trimer molecule (T') and metal slabs (M'). This energy is also referred to as the trimer binding energy, equation 7.1. E_{ads} is the adsorption energy of the

$$\mathbf{E_{ads} = E_{M'\text{-}T} - [E_{M'} + E_{T'}]} \qquad \mathbf{(7.1)}$$

cyclo-[Au(μ-Pz)]$_3$ trimer on the Au(111)/Al(111) metal slabs. $E_{M'\text{-}T}$, $E_{M'}$, $E_{T'}$ are the total energies of individually optimized metal slab-trimer complex, isolated metal slabs and isolated Au trimer molecule respectively. From equation 7.1, the adsorption energies (E_{ads}) of the gold pyrazolate trimer on Au(111) and Al(111) surfaces are found to be -0.73 and -0.59 eV, respectively. The energy values indicate that the gold pyrazolate trimer binds more strongly to the Au(111) surface than on Al(111) by 0.14 eV. Also, the E_{ads} values correlate with the bond distances of gold atoms of the trimer molecule to the metal slabs (aurophilic for Au(111)-T and van der Waals for Al(111)-T). In addition, the adsorption energies are also consistent with the 'concave up' shape of the gold pyrazolate trimer on the Au(111) surface versus a flat alignment on the Al(111) surface. The GGA-PBE functionals used here tend to dramatically underestimate the adsorption interactions[35] so we used the dispersion corrected DFT-D3 approach[36] with PAW pseudopotentials and GGA-PBE functional to determine the adsorption energies of cyclo-$[Au(\mu\text{-}Pz)]_3$ trimer on the Au(111)/Al(111) metal slabs. Single point DFT-D3 calculations were performed on metal slab-trimer complexes, isolated metal slabs and isolated Au trimer molecule obtained from optimizations at the previously mentioned level of theory. Upon adding dispersion corrections, the adsorption energies (E_{ads}) of the gold pyrazolate trimer on Au(111) and Al(111) surfaces obtained from equation 7.1, are found to be -3.63 and -2.45 eV, respectively. This significant change in the adsorption energies indicate that dispersion interactions play a very important role in adsorption. It is also important to note that DFT-D calculations slightly overestimate the dispersion interactions due to a double counting of correlation effects[37]. However, our focus here is to predict a qualitative binding trend of T to Au/Al(111) surfaces which is consistent with and without adding the dispersion corrections and indicate that gold pyrazolate trimer binds more strongly to the Au(111) surface than on Al(111). The present adsorption energy trend of T on Au(111) and Al(111) also agrees with our earlier investigation[14] of metal atom-trimer interactions.

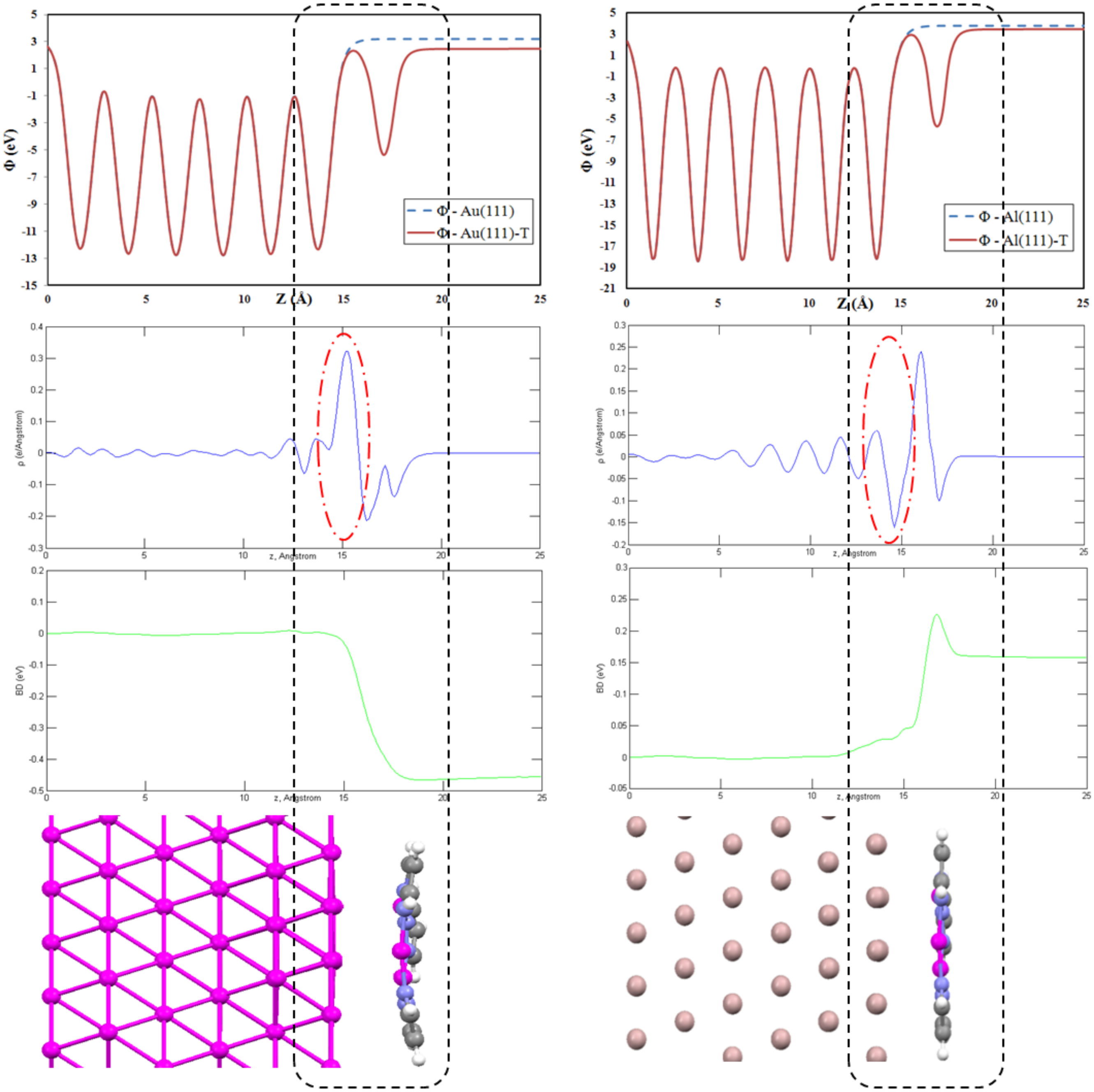

Figure 7.5. Plots/figures on the left represent the Au(111)-T interface system and those on the right represent the Al(111)-T interface system. Upper panel: Electrostatic potentials for the clean metal(111) surface (blue dashed line) and metal(111)-trimer interface (brown solid line). Middle panel: Valence charge density difference (blue solid line) observed at the interface upon trimer adsorption. The red (dot-dash) ovals indicate the charge density "push" away (in Au(111)-T) and towards (in Al(111)-T) the cyclo-[Au(μ-Pz)]3 trimer from their respective metal(111) surfaces. Lower Panel: Bond/interface dipoles (solid green line) obtained from solving the Poisson's equation. In the bottom, optimized geometries of Au(111)-T (left) and Al(111)-T interface systems. The dashed black line in the figure represents the interface area of both model systems.

7.3.3 Work Function Change and Charge Redistribution

Upon adsorption of the gold pyrazolate trimer with the metal surfaces, work-functions (Φ) of the metal surfaces are altered. Calculated work functions of Au(111), Al(111) surfaces have changed from 5.16 and 4.01 eV to 4.49 and 4.22 eV, respectively, from before and after trimer adsorption. Thus, the corresponding work function differences are $\Delta\Phi_{Au}$ = -0.67 eV and $\Delta\Phi_{Al}$ = +0.21 eV. Similar previous studies by Bredas and coworkers[38] on the interaction of organic self-assembled monolayers and semiconductors with metal surfaces have indicated that the change in the work function can be attributed to two major contributions originating from

(a) Change in vacuum potential (ΔU_{vac}) due to molecular dipole moment of the adsorbing monolayer

(b) Formation of bond/interface dipoles (BD) at the metal-trimer interface.

ΔU_{vac} comes from the electrostatic potential difference of vacuum across a single, 2D molecular layer obtained from DFT calculations (for benchmark description see reference[38d]) of cyclo-[Au(μ-Pz)]$_3$ monolayer at its respective metal surface adsorbed geometry without a metal slab. For cyclo-[Au(μ-Pz)]$_3$ monolayer geometry obtained from Au(111)-T interface system, $\Delta U_{vac\text{-}Au}$ = -0.22 eV, but for that obtained from Al(111)-T interface system, $\Delta U_{vac\text{-}Al}$ = -0.03 eV. A larger $\Delta U_{vac\text{-}Au}$ value than $\Delta U_{vac\text{-}Al}$ can be attributed to unsymmetrical ('concave up' shape) atomic positions of gold pyrazolate trimer when adsorbed on the Au(111) surface versus symmetrical ('flat' shape) alignment when adsorbed on the Al(111) surface (see bottom in Figure 7.5). Also differences in the lattice constants of Au and Al can lead to variation in packing of the monolayer on the metal surfaces and thus causing different potential steps across the 2D molecular layer.

The work function change caused by formation of bond dipoles can be determined by plotting the charge redistribution at the metal-trimer interface. The charge redistribution is obtained by solving the one dimensional Poisson's equation of charge density over the a,b-plane:

$$\nabla^2 V(z) = -\frac{\rho_{diff}(z)}{\varepsilon_o} \qquad \textbf{(7.2)}$$

$$\rho_{diff}(z) = \rho_{M'-T}(z) - \rho_{M'}(z) - \rho_T(z) \qquad \textbf{(7.3)}$$

where V(z) is the electrostatic potential energy (upper panels in Figure 7.5), ε_o the vacuum permittivity, $\rho_{diff}(z)$ the averaged surface charge density difference over the a,b-plane and $\rho_{M'-T}(z)$, $\rho_{M'}(z)$, $\rho_T(z)$ represent the plane averaged surface charge densities for the metal-trimer interface, metal(111) surface and isolated trimer (at the same geometry of the metal-trimer interface). The charge density difference ($\rho_{diff}(z)$) for Au(111)-T and Al(111)-T interface systems calculated from equation 7.3 is plotted with respect to the distance along the c-axis of the unit cell (middle panels in Figure 7.5).

7.3.3.1 Au(111)-T interface system

For the Au(111)-T system, the charge density difference (see plot in left middle panel in Figure 7.5) goes from nearly zero until layer 5 of the gold surface (z ~ 13 Å) to slightly negative between layers 5 and 6 (layer 6 is that in contact with the trimer) to then positive upon crossing the gold surface, reaching a maximum (0.30 e^-/Å) at z ~ 15 Å. The $\rho_{diff}(z)$ then falls back to negative, reaching a minimum (-0.20 e^-/Å) at z ~ 16 Å and eventually reaching zero at z ~ 19 Å. The evolution of $\rho_{diff}(z)$ in the interface region (ca. 14 - 17 Å) between the gold surface and the trimer indicate that electron density is being pushed back (red oval in left middle panel of Figure 7.5) towards the gold surface upon adsorption of trimer molecule. Such evolution has been referred to as the 'pillow effect'[39]. Accordingly, we also observe a potential energy, V(z), drop by -0.45 eV in the interface region (see plot in left lower panel in Figure 7.5). This drop in the potential energy is due to formation of bond dipoles (BD_{Au}) between the trimer and gold surface, which was defined as the interface dipoles in similar studies[16,17,38] with organic molecules. Since the work function modification for an Au(111) surface is attributed to the contributions from $\Delta U_{vac\text{-}Au}$ and BD_{Au}, the work function difference $\Delta\Phi_{Au}$ can be expressed as follows:

$$\Delta\Phi_{Au} = \Delta U_{vac\text{-}Au} + BD_{Au} = -0.22 - 0.45 = -0.67 \text{ eV} \qquad \textbf{(7.4)}$$

This value clearly agrees with the calculated $\Delta\Phi_{Au}$ value and is consistent with previous studies[16,17,38]. Also from equation 7.4, it can be concluded that the bond dipole potential drop is a bigger contributor to work function change than the vacuum potential difference. However, the potential step caused by the molecular dipole moment ($\Delta U_{vac\text{-}Au}$) is also significant in the Au(111)-T system due to an unsymmetrical alignment of the T on the Au(111) surface.

7.3.3.2 Al(111)-T interface system

In the Al(111)-T system, the charge density difference (see plot in right middle panel in Figure 7.5) is nearly zero until layer 3 (z ~ 7 Å) of the aluminum surface. From layer 3 to layer 6 (z ~ 7 – 13 Å) $\rho_{diff}(z)$ oscillates up (+ve) and down (-ve) four times reaching a minimum (-0.15 e^-/Å) just after crossing the metal surface z ~ 14.8 Å. Followed by the minimum, $\rho_{diff}(z)$ rises back up reaching a maximum (0.24 e^-/Å) as it gets closer to the trimer molecule at z ~ 15.8 Å and eventually falls to zero at z ~ 18 Å. The evolution of $\rho_{diff}(z)$ in the interface region (ca. 13.5 - 17 Å) between the aluminum surface and the trimer indicates that electron density is being pushed (red oval in right middle panel of Figure 7.5) towards the trimer monolayer upon adsorption. Correspondingly, we also observe a potential energy, V(z), rise by 0.24 eV in the interface region (see plot in right lower panel in Figure 7.5). This rise in the potential energy is due to formation of interface/bond dipoles (BD_{Al}) between the trimer and gold surface. So the work function modification, $\Delta\Phi_{Al}$ for Al(111) surface can be expressed as follows:

$$\Delta\Phi_{Al} = \Delta U_{vac,Al} + BD_{Al} = -0.03 + 0.24 = +0.21 \text{ eV} \qquad \textbf{(7.5)}$$

This value clearly agrees with the calculated $\Delta\Phi_{Al}$ value given above and is also consistent with previous studies on organic materials[16,17,38]. Similar to the Au(111)-T system, we can conclude from equation 7.5 that the rise in interface dipole potential is a much bigger contributor to work function change than the vacuum potential difference due to planar alignment of the T on the Al(111) surface.

Overall, comparing the $\rho_{diff}(z)$ for both the Au, Al interface systems, it is found that for the Au(111)-T interface the charge density is being pushed back towards the metal surface from the trimer monolayer, whereas the opposite happens in the Al(111)-T system where the charge is being pushed towards the trimer monolayer from the Al(111) surface. This trend for metal surfaces is the same seen in a previous study on the interaction of a cyclo-$[Au(\mu\text{-}Pz)]_3$ trimer with electrode metal atoms[14]. Also, the work function change ($\Delta\Phi$) for Au(111)-T is greater than in the Al(111)-T system, which once again is indicative of the strength of their respective interface interactions. It is important to note that bond dipoles caused due to charge redistribution at the metal-trimer interfaces are dominant contributors to the $\Delta\Phi$ change versus vacuum level shifts due to molecular dipoles especially in Al(111)-T system.

7.3.4 Density of States

To better understand the adsorption interaction of the cyclo-$[Au(\mu\text{-}Pz)]_3$ trimer with electrode metal slabs, we examined the spin polarized density of states (DOS) of an isolated trimer molecule, Au(111)-T and Al(111)-T interfaces. Figure 7.6 shows the DOS plot for an isolated trimer molecule with projections (pDOS) for gold (pink) and ligand (cyan) atoms of the trimer. The Fermi level (E_f) of the trimer molecule was aligned to zero for simplicity. No spin polarization is observed for cyclo-[Au(μ-Pz)]$_3$. The calculated band gap (BG) of the isolated gold pyrazolate trimer was found to be 4.53 eV, which is ~ 1 eV less than our previously calculated value for the molecule using hybrid DFT techniques[14]. The difference in BG value from molecular (Gaussian-based) to PW-DFT calculations may be due to the discrepancy in their theoretical description. The top of the valence band of the trimer has contributions from both gold atoms and the pyrazolate ligand, with Au being the dominant contributor. The bottom of the conduction band is dominated by the ligand more than the Au atoms. This layout clearly agrees with earlier molecular DFT studies[14] on the cyclo-[Au(μ-Pz)]$_3$ trimer.

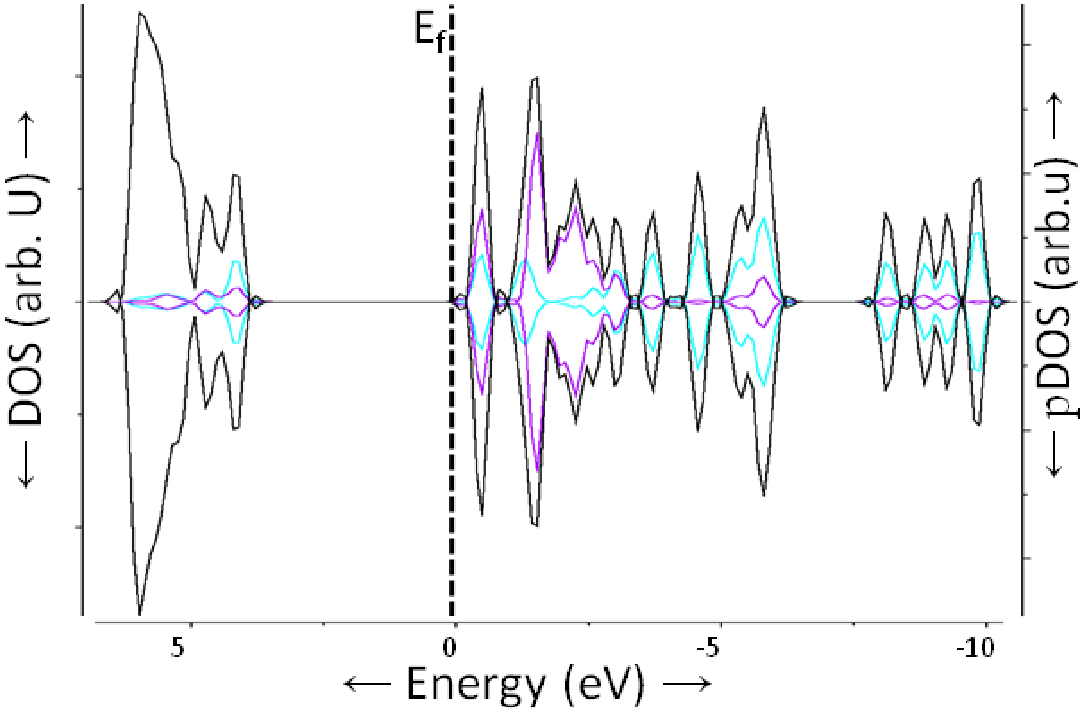

Figure 7.6. Spin polarized density of states (DOS) for isolated cyclo-[Au(μ-Pz)]3 trimer. In the plot, the solid black line represents the tDOS of the isolated trimer while solid purple and cyan lines represent the projected-DOS of Au atoms and ligands of the trimer respectively. The Fermi level (Ef) is represented by a dotted black line.

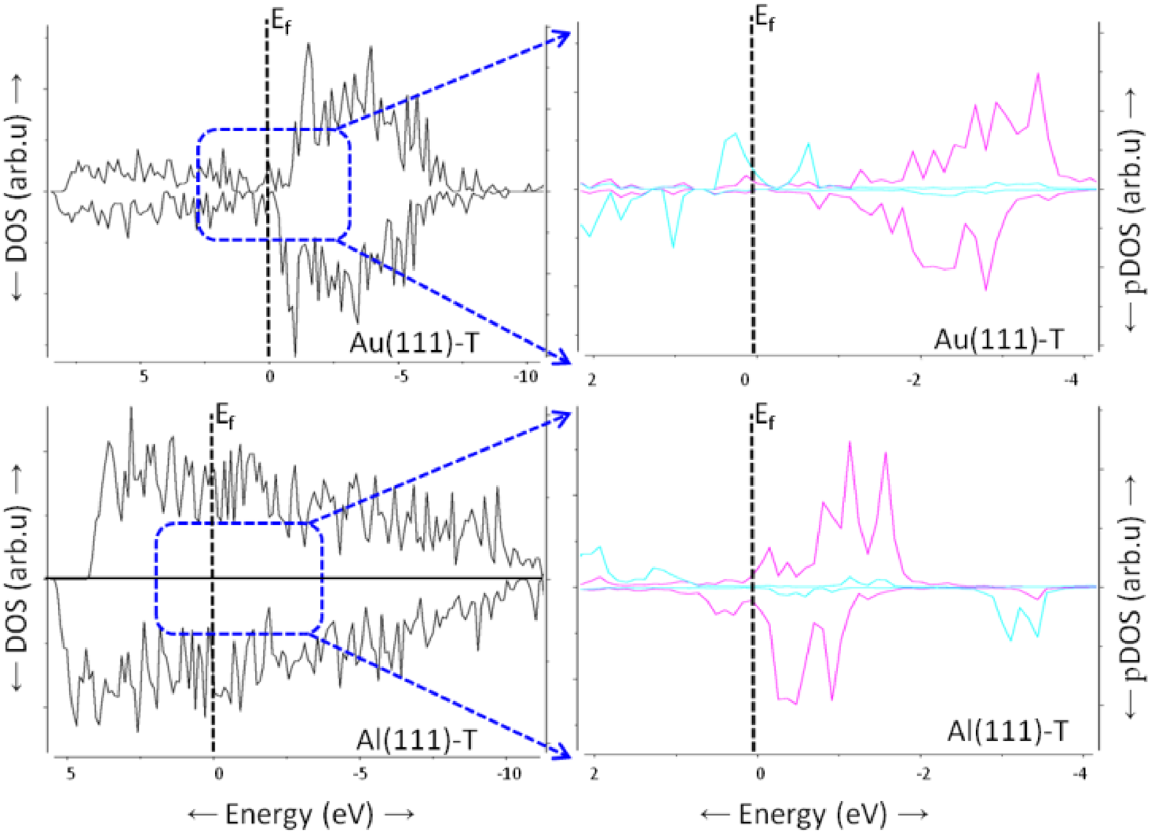

Figure 7.7. Spin polarized density of states (DOS) for Au(111)-T (top) and Al(111)-T (bottom) interface systems. The plots on the left with solid black lines represent the total-DOS. The plots on the right represent the projected-DOS of Au atoms (solid pink lines) and ligands (solid cyan lines) of the metal adsorbed cyclo-[Au(μ-Pz)]3 trimer. The Fermi levels (Ef) are represented by dotted black lines.

DOS plots of Au(111)-T and Al(111)-T interfaces are depicted in Figure 7.7. The Fermi level (E_f) of the trimer molecule was aligned to zero for simplicity. Observing the tDOS for M'-T complexes (left side in Figure 7.7) it can be seen that there is some degree of spin polarization present for both M'-T systems. The region around the Fermi level of the M'-T interfaces is enlarged and molecular projections (pDOS) for gold atoms (pink) and pyrazolate ligand (cyan) of the trimer are shown in the right side of Figure 7.7. Comparing the DOS of the gold pyrazolate trimer from its isolated form (Figure 7.6) with that in M'-T systems, it is observed that the DOS bands have broadened in the latter with essentially no band gap. The band broadening of the gold pyrazolate trimer in M’-T systems can be attributed to the interaction of the trimer with metal(111) slabs.

In Au(111)-T (right top in Figure 7.7) the top of the valence band of the trimer has contributions from both gold and the pyrazolate ligand, with the latter being the dominant contributor; the bottom of the conduction band has a greater contribution from the pyrazolate ligand than the Au atoms. However, in Al(111)-T (right bottom in Figure 7.7) both the top of valence band and the bottom of conduction band are dominated by gold atom contributions from the trimer than the pyrazolate ligand. So, the pDOS in M’-T systems are exhibiting different contributions around the Fermi level, possibly indicating the ligand dominated charge transfer in Au(111)-T and metal dominated charge transfer in Al(111)-T systems.

7.4 Summary and Conclusions

Surface interactions of the cyclo-[Au(μ-Pz)]$_3$ trimer (T) with Au(111) and Al(111) surfaces (M’) are studied using plane-wave density functional theory. The interfaces between the gold pyrazolate trimer and the metal(111) surfaces are built from fully relaxed structures of the isolated trimer (T) as well as Au(111) and Al(111) slabs. Upon geometric optimization the gold pyrazolate trimer aligns in a concave up shape on the Au(111) surface but remains planar on the Al(111) surface. Different geometric alignments of the trimer on metal surfaces are evident from strong (metallophilic) and weak (van der Waals) binding energies for cyclo-[Au(μ-Pz)]$_3$ on Au(111) and Al(111) surfaces, respectively.

Adsorption of the gold pyrazolate monolayer on Au(111) and Al(111) surfaces changes the work functions of their respective clean metal(111) surfaces. It was found that these work function changes in both Au(111)-T and Al(111)-T systems correspond to the sum of their respective monolayer vacuum level shifts and interface bond dipoles. Also redistribution of valence charge density is observed at both M'-T interfaces. The plane (a,b) averaged valence charge density difference (ρ_{diff}) plots obtained from Poisson's equation indicates that for the Au(111)-T system, the electron density is being pushed back towards the Au(111) surface and for the Al(111)-T system, the electron density is being pushed towards the cyclo-[Au(μ-Pz)]$_3$ trimer. Finally, we observe a DOS broadening of the cyclo-[Au(μ-Pz)]3 monolayer when bound to the metal surfaces with prominent near Fermi level contributions coming from the pyrazolate ligands in the Au(111)-T system and trimer gold atoms in the Al(111)-T system.

In conclusion, we present a comprehensive study of interface interactions between a monolayer of the p-type organometallic semiconductor, cyclo-[Au(μ-Pz)]$_3$ and high (Au) and low (Al) work function metal electrode surfaces. The present results indicate the role of molecular interactions, charge redistribution, interface dipoles, surface vacuum level shifts and band broadening at the metal(111)-trimer interfaces in influencing device performance. The present results for an extended system also closely correspond with our earlier study[14] on interaction of electrode metal atoms with cyclo-[Au(μ-Pz)]$_3$ showing that the gold pyrazolate trimer forms a stable interface with metal surfaces with low reorganization, substantial binding energies and considerable orbital mixing at the interface. As such, this work provides an important contribution in the search to rationally tie molecular structure to device properties for the design of organic and organometallic molecular electronics. This work also provides a clearer understanding of the structural and electronic properties of electrode-semiconductor interfaces that are needed to fabricate stable, better performing electronic devices.

7.5 Chapter References

(1) (a) Koch, N. *ChemPhysChem* **2007**, *8*, 1438-1455. (b) Kelley, T. W.; Baude, P. F.; Gerlach, C.; Ender, D. E.; Muyres, D.; Haase, M. A.; Vogel, D. E.; Theiss, S. D. *Chem. Mater.* **2004**, *16*, 4413-4422.

(2) (a) Zhou, G.; Wong, W.; Suo, S. *Journal of Photochemistry and Photobiology C: Photochemistry Reviews* **2010**, *11*, 133-156. (b) Chen, S.; Deng, L.; Xie, J.; Peng, L.; Xie, L.; Fan, Q.; Huang, W. *Adv Mater* **2010**, *22*, 5227-5239. (c) Farinola, G. M.; Ragni, R. *Chem. Soc. Rev.* **2011**, *40*, 3467-3482. (d) Duan, L.; Xie, K.; Qiu, Y. *J. Soc. Inf. Display* **2011**, *19*, 453-461.

(3) (a) Zaumseil, J.; Sirringhaus, H. *Chem. Rev.* **2007**, *107*, 1296-1323. (b) Klauk, H. *Chem. Soc. Rev.* **2010**, *39*, 2643-2666. (c) Newman, C. R.; Frisbie, C. D.; Da, S. F.; Bredas, J.; Ewbank, P. C.; Mann, K. R. *Chem. Mater.* **2004**, *16*, 4436-4451. (d) Di, C.; Yu, G.; Liu, Y.; Zhu, D. *J. Phys. Chem. B* **2007**, *111*, 14083-14096.

(4) (a) Harald Hoppe, N. S. *J. Mat. Res.* **2004**, *19*, 1924. (b) Yambem, S. D.; Haldar, A.; Liao, K.; Dillon, E. P.; Barron, A. R.; Curran, S. A. *Solar Energy Mater. Solar Cells* **2011**, *95*, 2424-2430. (c) Myung-Gyu Kang; Hui Joon Park; Se Hyun Ahn; Ting Xu; Guo, L. J. *Selected Topics in Quantum Electronics, IEEE Journal of* **2010**, *16*, 1807-1820. (d) Liao, K.; Yambem, S. D.; Haldar, A.; Alley, N. J.; Curran, S. A. *Energies* **2010**, *3*, 1212-1250.

(5) W.R. Caseri, ; H.D. Chanzy, ; K. Feldman, ; M. Fontana, ; P. Smith, ; T.A. Tervoort, ; J.G.P. Goossens, ; E.W. Meijer, ; A.P.H.J. Schenning, ; I.P. Dolbnya, ; M.G. Debije, ; M.P. de Haas, ; J.M. Warman, ; A.M. van de Craats, ; R.H. Friend, ; H. Sirringhaus, ; N. Stutzmann, *Adv Mater* **2003**, *15*, 125-129.

(6) Matsumoto, Y.; Murakami, M.; Shono, T.; Hasegawa, T.; Fukumura, T.; Kawasaki, M.; Ahmet, P.; Chikyow, T.; Koshihara, S.; Koinuma, H. *Science* **2001**, *291*, 854-856.

(7) (a) Kalyanasundaram, K.; Grätzel, M. *Coord. Chem. Rev.* **1998**, *177*, 347-414. (b) Ma, Y.; Zhang, H.; Shen, J.; Che, C. *Synth. Met.* **1998**, *94*, 245-248. (c) Wing-Wah Yam, V.; Kam-Wing Lo, K. *Chem. Soc. Rev.* **1999**, *28*, 323-334.

(8) (a) Yang, C.; Wang, X.; Omary, M. A. *J. Am. Chem. Soc.* **2007**, *129*, 15454-15455. (b) Barakat, K. A.; Cundari, T. R.; Rabaâ, H.; Omary, M. A. *J. Phys. Chem. B* **2006**, *110*, 14645-14651. (c) Yang, C.; Messerschmidt, M.; Coppens, P.; Omary, M. A. *Inorg. Chem.* **2006**, *45*, 6592-6594. (d) Dias, H. V. R.; Diyabalanage, H. V. K.; Eldabaja, M. G.; Elbjeirami, O.; Rawashdeh-Omary, M.; Omary, M. A. *J. Am. Chem. Soc.* **2005**, *127*, 7489-7501. (e) Dias, H. V. R.; Diyabalanage, H. V. K.; Rawashdeh-Omary, M.; Franzman, M. A.; Omary, M. A. *J. Am. Chem. Soc.* **2003**, *125*, 12072-12073.

(9) (a) Winkler, K.; Wysocka-Zolopa, M.; Recko, K.; Dobrzynski, L.; Vickery, J. C.; Balch, A. L. *Inorg. Chem.* **2009**, *48*, 1551-1558. (b) White-Morris, R.; Olmstead, M. M.; Attar, S.; Balch, A. L. *Inorg. Chem.* **2005**, *44*, 5021-5029. (c) Olmstead, M. M.; Jiang, F.; Attar, S.; Balch, A. L. *J. Am. Chem. Soc.* **2001**, *123*, 3260-3267. (d) Balch, A. L.; Olmstead, M. M.; Vickery, J. C. *Inorg. Chem.* **1999**, *38*, 3494-3499. (e) Fung, E. Y.; Olmstead, M. M.; Vickery, J. C.; Balch, A. L. *Coord. Chem. Rev.* **1998**, *171*, 151-159. (f) Vickery, J. C.; Olmstead, M. M.; Fung, E. Y.; Balch, A. L. *Angew. Chem. Int. Ed. (English)* **1997**, *36*, 1179-1181. (g) Vickery, J. C.; Balch, A. L. *Inorg. Chem.* **1997**, *36*, 5978-5983.

(10) (a) Pyykkö, P.; Mendizabal, F. *Inorg. Chem.* **1998**, *37*, 3018-3025. (b) Pyykkö, P. *Chem. Rev.* **1997**, *97*, 597-636. (c) Pyykkö, P.; Li, J.; Runeberg, N. *Chem. Phys. Lett.* **1994**, *218*, 133-138. (d) Pyykkö, P.; Zhao, Y. *Angew. Chem. Int. Ed. (English)* **1991**, *30*, 604-605.

(11) (a) Cundari, T. R.; Chilukuri, B.; Hudson, J. M.; Minot, C.; Omary, M. A.; RabaaÌ,, H. *Organometallics* **2010**, *29*, 795-800. (b) Rabaa, H.; Cundari, T. R.; Omary, M. A. *Can. J. Chem.* **2009**, *87(7)*, 775–783. (c) Smucker, B. W.; Hudson, J. M.; Omary, M. A.; Dunbar, K. R. *Inorg. Chem.* **2003**, *42*, 4714-4723. (d) Chen, W.; Reinheimer, E. W.; Dunbar, K. R.; Omary, M. A. *Inorg. Chem.* **2006**, *45*, 2770-2772. (e) Schmidbaur, H. *Chem. Soc. Rev.* **1995**, *24*, 391-400. (f) Schmidbaur, H.; Graf, W.; Müller, G. *Angew. Chem. Int. Ed. (English)* **1988**, *27*, 417-419. (g) Burini, A.; Mohamed, A. A.; Fackler, J. P. *Comments Inorg. Chem.* **2003**, *24*, 253.

(12) Tekarli, S. M.; Cundari, T. R.; Omary, M. A. *J. Am. Chem. Soc.* **2008**, *130*, 1669-1675.

(13) (a) Omary, M. A.; Rawashdeh-Omary, M.; Gonser, M. W. A.; Elbjeirami, O.; Grimes, T.; Cundari, T. R.; Diyabalanage, H. V. K.; Gamage, C. S. P.; Dias, H. V. R. *Inorg. Chem.* **2005**, *44*, 8200-8210. (b) Grimes, T.; Omary, M. A.; Dias, H. V. R.; Cundari, T. R. *J. Phys. Chem. A* **2006**, *110*, 5823-5830. (c) Raptis, R. G.; Fackler, J. P. *Inorg. Chem.* **1988**, *27*, 4179-4182. (d) Yang, G.; Raptis, R. G. *Inorg. Chem.* **2003**, *42*, 261-263. (e) Bovio, B.; Bonati, F.; Banditelli, G. *Inorg. Chim. Acta* **1984**, *87*, 25-33.

(14) Chilukuri, B.; Cundari, T. R. *J. Phys. Chem. C* **2011**, *115*, 5997-6003.

(15) (a) Scott, J. *J. Vac. Sci. Technol. A* **2003**, *21*, 521. (b) Mitrasinovic, P.M. *Curr. Org. Chem.*, **2010**, *14*, 198-211. (c) Flores, F.; Ortega, J.; Vazquez, H. *Phys. Chem. Chem. Phys.* **2009**, *11*, 8658-8675. (d) Knupfer, M.; Peisert, H. In *Electronic Properties of Interfaces between Model Organic Semiconductors and Metals;* Physics of Organic Semiconductors; Wiley-VCH Verlag GmbH & Co. KGaA: 2005; **2006**; pp 41-67.

(16) (a) Knupfer, M. *J. Vac. Sci. Technol. A* **2005**, *23*, 1072. (b) Ishii, H.; Sugiyama, K.; Yoshimura, D.; Ito, E.; Ouchi, Y.; Seki, K. *Selected Topics in Quantum Electronics, IEEE*

Journal of **1998**, *4*, 24-33. (c) Sehati, P.; Braun, S.; Lindell, L.; Xianjie Liu; Andersson, L. M.; Fahlman, M. *Selected Topics in Quantum Electronics, IEEE Journal of* **2010**, *16*, 1718-1724.

(17) (a) Yamane, H.; Yoshimura, D.; Kawabe, E.; Sumii, R.; Kanai, K.; Ouchi, Y.; Ueno, N.; Seki, K. *Phys. Rev. B* **2007**, *76*, 165436. (b) Watkins, N. *Appl. Phys. Lett.* **2002**, *80*, 4384. (c) Sun, X.; Suzuki, T.; Yamauchi, Y.; Kurahashi, M.; Wang, Z. P.; Entani, S. *Surf. Sci.* **2008**, *602*, 1191-1198. (d) Simeoni, M.; Picozzi, S.; Delley, B. *Surf. Sci.* **2004**, *562*, 43-52. (e) Chiodi, M.; Gavioli, L.; Beccari, M.; Di Castro, V.; Cossaro, A.; Floreano, L.; Morgante, A.; Kanjilal, A.; Mariani, C.; Betti, M. G. *Phys. Rev. B* **2008**, *77*, 115321. (f) Lee, K.; Yu, J. *Surf. Sci.* **2005**, *589*, 8-18. (g) Mura, M.; Gulans, A.; Thonhauser, T.; Kantorovich, L. *Phys. Chem. Chem. Phys.* **2010**, *12*, 4759-4767. (h) Terentjevs, A.; Steele, M. P.; Blumenfeld, M. L.; Ilyas, N.; Kelly, L. L.; Fabiano, E.; Monti, O. L. A.; Della Sala, F. *J. Phys. Chem. C* **2011**, *115*, 21128-21138.

(18) Hill, I.G.; Rajagopal, A.; Kahn, A. *Appl. Phys. Lett.* **1998**, *73*, 662.

(19) (a) Ishii, H.; Sugiyama, K.; Ito, E.; Seki, K. *Adv Mater* **1999**, *11*, 605-625. (b) Schroeder, P.; France, C. B.; Park, J. B.; Parkinson B. A. *J. Appl. Phys.* **2002**, *91*, 3010.

(20) Xavier, C. *Solar Energy Mater. Solar Cells* **2004**, *83*, 147-168.

(21) (a) Ishii, H.; Seki, K. *Electron Devices, IEEE Transactions on* **1997**, *44*, 1295-1301. (b) Rajagopal, A.; Kahn, A. *J. Appl. Phys.* **1998**, *84*, 355A. (c) Hirose, Y.; Kahn, A.; Aristov, V.; Soukiassian, P.; Bulovic, V.; Forrest, S. R. *Phys. Rev. B* **1996**, *54*, 13748-13758.

(22) Wyckoff, R.W.G. In: *Crystal Structures;* ed 2; Interscience Publishers, New York, New York, **1963**, 1, pp 7-83.

(23) Materials Design Inc. Angel Fire, NM, **2010**, http://www.materialsdesign.com/medea .

(24) (a) Harten, U.; Lahee, A.M.; Toennies, J.P.; Woll, C. *Phys. Rev. Lett.* **1985**, *54*, 2619-2622. (b) Woll, C.; Chiang, S.; Wilson, R.J.; Lippel, P.H. *Phys. Rev. B* **1989**, *39*, 7988-7991. (c) Barth, J.V.; Brune, H.; Ertl, G.; Behm, R.J. *Phys. Rev. B* **1990**, *42,* 9307-9318. (d) Huang, K.G.; Gibbs, D.; Zehner, D.M.; Sandy, A.R.; Mochrie, S.G.J. *Phys. Rev. Lett.* **1990**, *65*, 3313-3316. (e) Sandy, A.R.; Mochrie, S.G.J.; Zehner, D.M.; Huang, K.G.; Gibbs, D. *Phys. Rev. B* **1991**, *43***,** 4667-4687. (f) Takeuchi, N.; Chan, C.T.; Ho, K.M. *Phys. Rev. B* **1991**, *43*, 13899-13906.

(25) Materials Studio 4.4, Accelrys, Inc. San Diego, CA, **2008**, http://accelrys.com/products/materials-studio/.

(26) (a) Ehlert, M. K.; Rettig, S. J.; Storr, A.; Thompson, R. C.; Trotter, J. *Can. J. Chem.* **1990**, *68*, 1444-1449. (b) Kim, S. J.; Kang, S. H.; Park, K.; Kim, H.; Zin, W.; Choi, M.; Kim, K. *Chem. Mater.* **1998***, 10*, 1889-1893. (c) Torralba, M. C.; Ovejero, P.; Mayoral, M. J.; Cano, M.; Campo, J.; Heras, J.; Pinilla, E.; Torres, M. R. *Helv. Chim. Acta* **2004***, 87*, 250-263.

(27) (a) Burini, A.; Bravi, R.; Fackler, , John P.; Galassi, R.; Grant, T. A.; Omary, M. A.; Pietroni, B. R.; Staples, R. J. *Inorg. Chem.* **2000***, 39*, 3158-3165. (b) Omary, M. A. *et al.*, Abstracts of Papers, INOR-119; presentation to the ACS Division of Inorganic Chemistry, 236th ACS National Meeting, Philadelphia, PA, Aug 17-21, **2008**; American Chemical Society: Washington, DC., **2010**.

(28) Gnade, B. (University of Texas, Dallas); Omary, M. A (University of North Texas) - private communication.

(29) (a) Kresse, G.; Joubert, D. *Phys. Rev. B* **1999***, 59*, 1758. (b) Blochl, P.E. *Phys. Rev. B.* **1994**, *50*, 17953-17979.

(30) (a) Kresse, G.; Furthmüller, J. *Phys. Rev. B* **1996**, *54*, 11169. (b) Kresse, G.; Furthmüller, J. *Comp. Mater. Sci.* **1996**, *6*, 15-50.

(31) Perdew, J. P.; Burke, K.; Ernzerhof, M. *Phys. Rev. Lett.* **1996**, *77*, 3865.

(32) Monkhorst, H. J.; Pack, J. D. *Phys. Rev. B* **1976**, *13*, 5188.

(33) Michaelson, H. *J. Appl. Phys.* **1977**, *48*, 4729.

(34) (a) Bondi, A. *J. Phys. Chem.* **1964**, *68*, 441-451. (b) Huheey, J.E.; Keiter, E.A.; Keiter, R.L. In *Inorganic Chemistry : Principles of Structure and Reactivity*; ed 4; HarperCollins, New York, USA, **1993**.

(35) Kristyán, S.; Pulay, P. *Chem. Phys. Lett.*, **1994**, *229*, 175.

(36) Grimme, S.; Antony, J.; Ehrlich, S.; Krieg, H. *J. Chem. Phys.* **2010**, *132*, 154104.

(37) Barone, V.; Biczysko, M.; Pavone, M. *Chem. Phys.* **2008**, *346*, 247-256.

(38) (a) Heimel, G.; Romaner, L.; Zojer, E.; Brédas, J. *Nano Letters* **2007**, *7*, 932-940. (b) Li, H.; Duan, Y.; Coropceanu, V.; Brédas, J. *Org. Elect.* **2009**, *10*, 1571-1578. (c) Beljonne, D.; Cornil, J.; Muccioli, L.; Zannoni, C.; Brédas, J.; Castet, F. *Chem. Mater.* **2011**, *23*, 591-609. (d) Heimel, G.; Romaner, L.; Brédas, J.L.; Zojer, E. *Surf. Sci.* **2006**, *600*, 4548-4562. (e) Crispin, X.; Geskin, V.; Crispin, A.; Cornil, J.; Lazzaroni, R.; Salaneck, W. R.; Brédas, J. *J. Am. Chem. Soc.* **2002**, *124*, 8131-8141.

(39) Koch, N.; Vollmer, A,; Duhm, S.; Sakamoto, Y.; Suzuki, T. *Adv. Mater.* **2007**, *19*, 112-116.

CHAPTER 8

SUMMARY AND FUTURE DIRECTIONS

In the 21st century, the usage of novel electronic/technological devices has become an integral part of human life. For example, mobile phones, television sets, computers etc., are ubiquitous. For years, most electronic devices made have been based on silicon, which has high processing costs and results in low device flexibility. Due to increased production cost, lack of material resources, quest for renewable energy and desire to produce innovative and high performing products, industries and governments continue to fund projects for breakthrough research in development of novel electronic materials and devices beyond silicon. In an attempt to find alternative materials, a new field of organic electronics has emerged over the last 2 - 3 decades leading to innovations like organic light emitting diodes (OLEDs), organic field effect transistors (OFETs) or organic thin film transistors (OTFTs), radio frequency identification (RFID) tags, conductive polymer printed electronics and organic photovoltaics (OPVs) or organic solar cells. Furthermore, organic electronic materials are cost effective, highly flexible, need low temperature processing condition and there is a continuous emergence of new organic semiconducting materials with tailored electronic properties. However, devices such as OFETs and OPVs have not achieved the type of performance and stability similar to those with inorganic electronic devices, which is mainly due to the low electron and hole mobilities (μ) in organic semiconductors.

The research presented in this dissertation is a small effort in a broader context of the application of computational simulations to guide experimentalists in their pursuit of novel electronic materials and devices. The electronic materials studied here are organometallic complexes, which by virtue of their diverse chemical (covalent, ionic, electrostatic, metal-metal,

metal-π, and π-π) interactions can produce promising molecular electronic devices. The work presented in this dissertation basically addresses two approaches toward making better electronic devices using computational modeling.

Approach (1): Finding novel organometallic electronic materials.

Approach (2): Understanding interface chemistry in electronic devices

Approach (1) is aimed to guide experimental chemists to synthesize and characterize new organometallic complexes with tailored electronic properties such as p-/n-type materials by making a rational choice of ligands, metals and substituents. Approach (2) is designed to study the interface chemistry of semiconductors and other device components like electrodes, substrates, and dielectrics. Understanding interface chemistry in electronic devices helps engineers to make rational choices of materials to fabricate the device.

Chapters 3-5 deals with approach (1) where I modeled the geometric, electronic and conduction properties of platinum based charge transfer complexes and d^{10} cyclo-$[M(\mu\text{-}L)]_3$ trimers (M = Ag, Au and L = monoanionic bidentate bridging (C/N~C/N) ligand) using molecular and periodic simulation methodologies. It was concluded from the simulations that molecular and solid state packing, chemical composition (metals, ligands and substituents), synthetic/crystal growth processes effect the material properties in organometallic complexes. Furthermore, calculations provided a comprehensive picture of the electronic and conduction properties of the organometallic complexes based on which selective synthesis and growth of materials with tailored electronic properties is recommend to experimental chemists. For example in Chapter 3, it was predicted that DD/A stacking of Pt(II) donor (D) and organic acceptor (A) molecules exhibit better conduction properties than D/A stacking. In Chapter 4, calculations suggest that Ag_3•Au_3 trimer complexes exhibit charge transfer interactions where substituents play a very key role in the interaction. Additionally, the simulations support the experimental spectroscopic data suggesting the fact that the molecular designs of both p- (Au trimer) and n-type (Ag trimer) metal-organic complexes are wide-band-gap semiconductors and are particularly attractive for novel light-emitting device concepts, such as phosphorescent p-n junction or bulk heterojunction OLEDs and ambipolar/light-emitting OFETs. Finally, in Chapter 6, a combined periodic and molecular simulations predicted that an infinitely stacking cyclo-[Au_3(RN=COR')$_3$] complexes (where R and R' are a selection of substituents) have lower band gaps with better optoelectronic and charge transport properties for fabrication in electronic devices. The studies in Chapter 6 also agree with the available spectroscopic data.

The work done so far on approach (1) has yielded promising results in terms of the short term goals of finding novel metal-organic electronic materials. However, if you consider the cost benefit of the type of transition metals (Au, Ag, Pt) used in the present studies, it is not practically feasible to produce commercial devices out of such complexes. Hence, it is necessary to make organometallic complexes with cheaper 3d metals that have excellent electronic and mechanical properties for commercial molecular electronics applications. The valuable information regarding the material properties gained from the present research on expensive transition metal complexes can now be used to design cheaper and better organometallic electronic materials in the future.

Chapters 6 and 7 deals with approach (2) where multi-scale computational simulations were performed on the interfaces of a p-type metal-organic semiconductor viz cyclo-[Au(μ-Pz)]$_3$ trimer with metal electrodes at atomic and surface levels. Simulations at the molecular level with multiple electrode metal atoms and at the periodic level with Au(111) and Al(111) surfaces indicate huge orbital mixing in the interfaces with varying binding energies and charge transfer behaviors. Calculations provided insight into the type of chemical interactions/bonding, bond dipoles, work function and energy level alignments, direction of charge flow, etc., on the interface between cyclo-[Au(μ-Pz)]$_3$ trimer and electrode metal atoms and surfaces. The different interface characteristics obtained from multi-scale simulations presented in this dissertation can be helpful for engineers to narrow their choice of electrode metals that can be used in conjunction with the cyclo-[Au(μ-Pz)]$_3$ trimer if they were to fabricate the device. Thus, theory guided device fabrication is recommended if there is a thorough understanding of the interface chemistry.

My research on approach (2) has so far only studied the interfaces between electrode metals and cyclo-[Au(μ-Pz)]$_3$. Future work can be done on interfaces of other organic/metal-organic semiconductors, electrode metals and dielectric materials. Although enough research has been done on interfaces between organic semiconductors and electrode metals, very little modeling work has been done on low-k dielectric materials and their interfaces in the literature. The difficulty in modeling dielectric interfaces is the lack of available structures of amorphous/polymer dielectrics. Thus, there is plenty of room for future research toward modeling plausible structures of dielectric materials with molecular dynamic simulations using available experimental X-ray diffraction, NMR and spectroscopic data. Such structures can be used to model interfaces with semiconducting materials and obtain the necessary information to guide the device fabrication process.

Following the directions for the two approaches presented in this chapter, novel metal-organic semiconductors and devices can be developed smartly in addition to understanding the fundamental questions that will supply the chemical and engineering community with high-impact scientific and technological findings.